Alma Mater Studiorum · University of Bologna

School of Science
Department of Physics and Astronomy
Master Degree in Physics

Measurement of nuclear fragmentation cross section for a 400 MeV/u ^{16}O beam on a polyethylene target with the FOOT experiment

Supervisor:
Prof. Mauro Villa

Co-supervisor:
Dr. Riccardo Ridolfi

Submitted by:
Matilde Dondi

Academic Year 2023/2024

Abstract

Hadrontherapy is an external radiation therapy for cancer that uses beams of charged particles, protons or heavier ions, to target the tumor and prevent its proliferation. When entering a medium, due to electromagnetic interactions with electrons, a charged particle releases most of its energy just before stopping in the so-called Bragg peak, whose position depends on the initial energy of the particle. The energy release is thus concentrated in the tumor area, minimizing damage to surrounding healthy tissues. Nuclear interactions can also occur, causing fragmentation of human body nuclei and of the beam, possibly changing the dose release profile. A precise understanding of these interactions is therefore needed. Another field that benefits from nuclear interaction measurements is space radioprotection. The main concern of human missions in deep space is protecting astronauts from the harsh space radiation environment. To provide effective shielding, nuclear interaction data are fundamental to develop accurate models and evaluate health risks. However, nuclear fragmentation cross section data are very limited.

The FOOT (FragmentatiOn Of Target) experiment aims to fill this gap by measuring the nuclear fragmentation double differential cross section with respect to the kinetic energy of the fragments and their emission angle, with a precision within 5%. The experiment is composed of two different setups: an emulsion setup, optimized for light fragments, and an electronic setup.

In this thesis I analyze a data sample taken at GSI (Darmstadt, Germany) in July 2021, with the electronic setup, with a 400 MeV/u ^{16}O beam on a polyethylene (C_2H_4) target, obtaining a first evaluation of total and angular differential cross section for different fragment charges. Using a previous result with a graphite (C) target, the cross section for a proton target is also obtained. When a comparison is possible, the results are in agreement with the limited data currently available.

Contents

Introduction

Hadrontherapy, like conventional radiotherapy, is an external radiation therapy for cancer treatment that targets the tumor and prevents its proliferation. However, while radiotherapy uses photons, hadrontherapy utilizes charged particles such as protons or heavier ions. The main difference between these two therapies resides in the different dose profiles of the particles employed: photons release a higher amount of energy upon entering the medium, which gradually decreases as they penetrate deeper, while charged particles primarily release most of their energy just before stopping, at the so-called Bragg peak. The position of this peak depends on the initial energy of the particle beam. Thanks to these properties, in hadrontherapy the energy release is concentrated in the tumor area, thereby minimizing damage to the surrounding healthy tissues. At typical hadrontherapy energies, from 120 MeV/u up to 400 MeV/u for heavier ions, nuclear fragmentation can occur, involving both the projectile and the target, i.e. human body nuclei. Fragments produced by the projectile can reach regions beyond the Bragg peak, potentially releasing energy in healthy tissue; on the other end, fragments produced by the target travel no more than tenths of μm, releasing their energy where they are produced. For this reason, an accurate knowledge of nuclear fragmentation processes is necessary.
Nuclear fragmentation can play an important role also in the field of space radioprotection. Space agencies around the world, including NASA and ESA, are showing an increasing interest in human missions beyond the Low Earth Orbit to explore new frontiers. However, one of the biggest challenges in these missions is dealing with the particularly harsh space radiation environment, which is a significant risk for the health of astronauts. Since space radiation is isotropic, the most effective countermeasure that can be taken to provide protection against it is shielding. To provide an effective shielding, as well as to evaluate risks during space missions, a clear knowledge of physical processes involved is required, starting from nuclear fragmentation. Unfortunately, the availability of nuclear fragmentation data is very limited, particularly regarding target fragmentation.
The FOOT (FragmentatiOn Of Target) experiment aims to fill the gap in nuclear fragmentation measurements by measuring the double differential cross section with respect to the kinetic energy of the fragments and their emission angle, achieving a precision within 5%. The FOOT experiment is equipped with two different experimental setups to identify the various fragments produced: an electronic setup designed for detecting

charged fragments with $Z \geq 2$, and an emulsion setup optimized for lighter fragments. The electronic setup is composed of a tracking region to measure the momentum of the fragments and a section dedicated to charge identification and kinetic energy evaluation. To properly address relevant cross section measurements, the FOOT experiment employs an inverse kinematics strategy: instead of firing a proton beam against a target resembling a human tissue, nuclei which are abundant in the human body are fired as projectiles on a target containing Hydrogen (protons). In this way, the produced fragments have enough kinetic energy to exit the target and to be detected by the apparatus, in order to determine their production cross section. At the end, a Lorentz boost is applied to obtain the cross section in direct kinematics. The experiment has a table top setup so that it can be easily transported in different research centers to perform measurements. The targets used are the same both for particle therapy and space radioprotection applications: graphite (C), polyethylene (C_2H_4) and PMMA ($C_5O_2H_8$) with different beam elements and energies, ranging from 200 MeV/u up to 800 MeV/u in the case of radioprotection.
In this thesis work a first analysis conducted with data acquired at GSI in July 2021 with a 400 MeV/u ^{16}O beam impinging on a 10 mm C_2H_4 target is presented. At the time, the FOOT setup was not in its final configuration. It was composed of a scintillator foil that provides the trigger, a drift chamber to monitor the beam before the target and, at 1.93 m from the target, two layers of scintillator bars, called Tof Wall. The energy loss in the Tof Wall, together with the time-of-flight information, is used to reconstruct the particle charge. Without the tracking system, it was not possible to evaluate the mass of the fragments and to recognize fragmentations outside the target event by event. To remove the background, a run without the target has been subtracted to the data acquired with the target. The same analysis conducted on the data was also carried on a Monte Carlo (MC) sample to validate the technique and calculate the efficiencies. From the analysis, total and angular differential cross section for different charges has been extracted. Using a previous result obtained with a Carbon target with the same beam conditions, the cross section for a proton target has been calculated, subtracting the Carbon cross section from the polyethylene one.
In Chapter 1 an overview of processes involved when charged particles interact with matter is presented, with a focus on aspects relevant for hadrontherapy and space radioprotection. Chapter 2 contains an explanation of hadrontherapy principles and a description of the space radiation environment. The role of nuclear fragmentation is also highlighted, together with some relevant measurements that can be found in literature. In Chapter 3, the FOOT experiment is explained, focusing on the electronic setup. In Chapter 4 the analysis on GSI2021 data is described and its results are presented.
Moreover, during my master's program, I spent a period at the CNAO (Centro Nazionale di Adroterapia Oncologica) working on a project aimed at performing dose verification during patient treatment sessions. This work is presented in Appendix A.

Chapter 1

Charged particles interactions in matter

In this chapter I will give an overview of processes involved when charged particles, such as protons and heavier ions, interact with matter, focusing on aspects relevant for hadrontherapy and space radioprotection applications.
Charged particles mainly interact electromagnetically with atomic electrons through inelastic Coulomb scattering, a process that leads to energy loss. They can also undergo elastic Coulomb scattering with nuclei, which causes deviations from their initial trajectory. Although less frequent, nuclear interactions can also occur, playing an important role in both particle therapy and space radioprotection.

1.1 EM interactions with atomic electrons

When a heavy charged particle such as a proton or a heavier ion, enters an absorbing medium, it mainly interacts with atomic electrons. Considering the dimensions of a nucleus, approximately $\sim 10^{-15}$ m, compared to those of an atom, around $\sim 10^{-10}$ m, the probability of interaction is 10^{10-8} times higher for the atom. This significant difference makes interactions with atomic electrons far more probable than with nuclei.
Depending on the interaction's intensity, the collision can either lead to the excitation of an atomic electron to a higher energy level (*excitation*) or be sufficiently energetic to eject the electron entirely from the atom (*ionization*). During excitation, the electron is promoted to an external atomic energy level and subsequently de-excites by emitting a photon.
Since the mass of the electron is much smaller than that of the incoming proton or charged ion, the trajectory of the primary particle remains nearly straight. This is because the primary particle is not significantly deflected by these inelastic interactions, which occur randomly in all directions. The energy transferred to the electron comes

from the particle's kinetic energy, leading to a reduction in the particle's speed.
As the charged particle traverses the medium, it interacts with numerous electrons. Consequently, it is better to discuss the overall energy loss of the particle rather than focusing on individual collisions. Each collision results in a very small fraction of the total energy being transferred, so the energy loss process can be considered continuous.

1.1.1 The Bethe-Bloch formula

The continuous loss of energy process of charged particles can be described by the concept of stopping power [1]. This quantity, which represents a force, indicates the average energy loss per unit length:

$$S = \frac{dE}{dx} \tag{1.1}$$

where E is the deposited energy in the infinitesimal path dx. The first attempt to find an expression for the stopping power was made by Bohr using a classical approach. Later, Bethe and Bloch, through a quantum mechanical treatment, derived the following formula:

$$-\frac{dE}{dx} = 2\pi N_A r_e^2 m_e c^2 \rho \frac{Z}{A}\frac{z^2}{\beta^2}\left[\ln\left(\frac{2m_e\gamma^2 v^2 W_{max}}{I^2}\right) - 2\beta^2 - \delta - 2\frac{C}{Z}\right] \tag{1.2}$$

where $2\pi N_A r_e^2 m_e c^2 = 0.153\,55\,\mathrm{MeVcm^2/g}$, with N_A the Avogadro number and:

- r_e is the classical electron radius and m_e is the electron mass,
- c is the speed of light in vacuum,
- ρ, Z and A are the density, the atomic number and the mass number of the irradiated material,
- z is the atomic number of the atoms of the incident radiation,
- $\beta = v/c$ and $\gamma = 1/\sqrt{1-\beta^2}$ with v incident particle's velocity,
- $\mathrm{W_{max}}$ is the maximum energy transferred in a single collision,
- I is the mean excitation potential of the atoms in the material,
- δ is the delta correction,
- C is the shell correction.

This formula assumes that the electron is effectively at rest relative to the incoming charged particle. Additionally, as previously mentioned, due to the electron's much smaller mass compared to the incoming particle, the particle's trajectory remains almost unchanged, only experiencing energy loss in the process.
The dependence on the medium in this formula is associated with the term ρZ/A and the mean excitation potential I. The mean excitation potential I depends on the atomic number Z of the material, with values ranging from 19 eV for Hydrogen to 820 eV for Lead. Since I appears inside a logarithm, its impact on the overall energy loss is relatively

minor. The ratio Z/A typically remains around 0.5 and is approximately 0.42 for heavier nuclei, typically not present in the human body. In contrast, the density ρ can vary significantly between different materials, making it the primary factor that expresses the medium dependence in this formula.

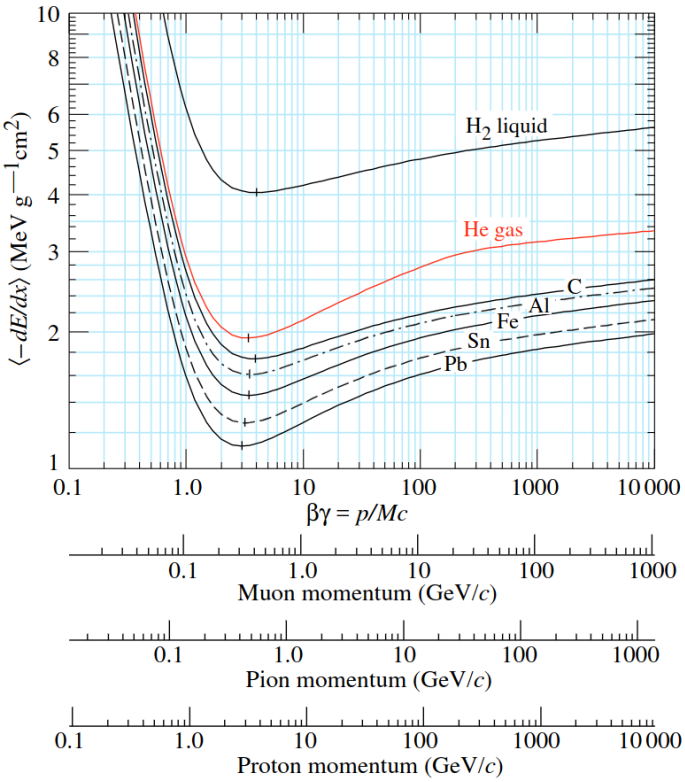

Figure 1.1: Variation of the Mass Stopping Power as a function of $\beta\gamma$ for different particles (muon, pion and proton) and materials [2].

In order to have a more material independent formula, the *mass stopping power* is defined, as:

$$-\frac{dE}{d\chi} = -\frac{1}{\rho}\frac{dE}{dx}\,. \tag{1.3}$$

The *stopping power* of a charged particle depends on its velocity (β). At low energies, it is inversely proportional to β^2. Its value decreases until it reaches a minimum around $\beta\gamma = 3 - 4$, after which it increases logarithmically with β^2. Figure 1.1 illustrates the variation of the Mass Stopping Power as a function of $\beta\gamma$.
In the energy range relevant for hadrontherapy, the energy loss primarily depends on the z^2/β^2 of the incident particle. This means that, in this region, the particle releases more energy as it slows down, leading to a peak in energy release just before it stops. This is

known as the *Bragg peak* and, as illustrated in Section 2.1.1, its position depends on the initial kinetic energy of the beam.
The density correction δ presented in Eq. 1.2 becomes important at high energy and its related to the polarization of the atoms along the incident particle's path. Electrons far from the particle are shielded from its electric field and, as a result, they contribute less to the total energy loss. This correction mitigates the logarithmic increase in energy loss at high energies and depends on the density of the material.
The shell correction, instead, becomes significant at lower energy, when the velocity of the incident particle is comparable or less than the orbital velocity of the bound electrons. At these energies, the assumption that the electron is stationary relative to the incident particle is no longer valid, but generally this correction is small. This correction prevents the Bethe-Bloch from being infinite (non-physical result) when the velocity β tends to zero. The plot in Figure 1.2 shows the effect of this correction.

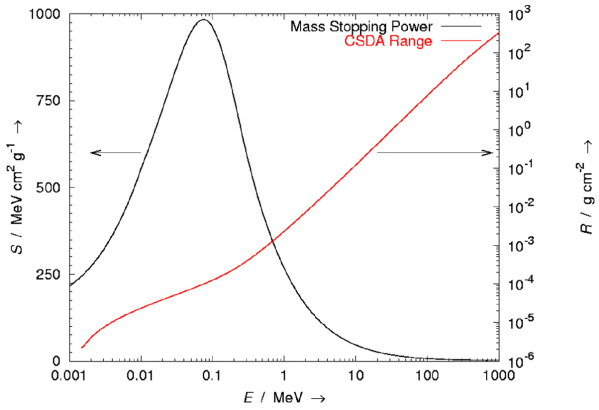

Figure 1.2: Mass stopping power in function of ion energy for protons in liquid water, in the hadrontherapy energy range [3]. The $1/\beta^2$ increase is stopped at low energy by the shell correction. In red, the corresponding range is shown (see Section 1.1.2).

For an electron entering a medium, the process of energy loss can be still described by the Bethe-Bloch; however, some corrections are needed to account for the small mass of the electron and the fact that it interacts with other electrons, i.e. identical particles. In addition, for electrons, energy loss by radiation (*Bremsstrahlung*) is also relevant [1].

1.1.2 Energy loss fluctuations and range

The energy loss process, as previously stated, results from a stochastic process involving hundreds of interactions. This means that particles with the same initial energy will not have the same exact energy release (*energy loss straggling*). The energy loss is described by a Landau-Vavilov distribution, as shown in Figure 1.3.

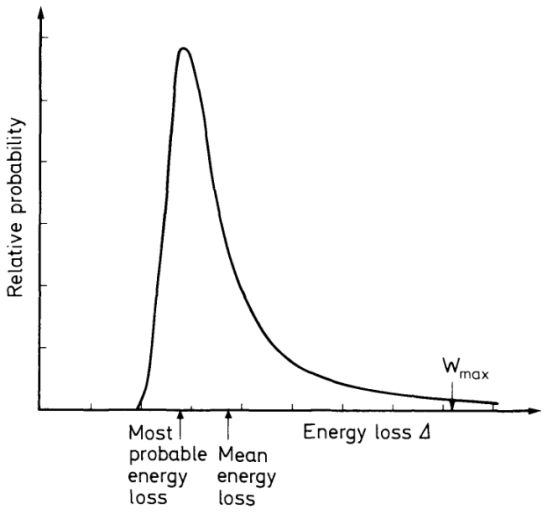

Figure 1.3: Typical distribution of energy loss in a thin absorber: the distribution is asymmetric with a tail at high energy [1].

In the case of a thick absorber material, where many collisions take place, considering the central limit theorem, the distribution can be considered Gaussian [4]:

$$f(\Delta E) = \frac{1}{\sqrt{2\pi\sigma^2}} \exp \frac{(\Delta E - \overline{\Delta E})^2}{-2\sigma^2} \tag{1.4}$$

where σ is the energy loss fluctuation, ΔE the energy loss and $\overline{\Delta E}$ the mean energy loss value. Even though the process is statistical, it is possible to define the path travelled by a charged particle before it stops in a given material. This quantity is called range, and its most common definition is obtained considering the particle as continuously slowing down (*Continuous-Slowing-Down Approximation*) in the medium. It is defined integrating the Bethe-Bloch equation as:

$$R(E_0) = \int_0^R dx = \int_0^{E_0} - \left(\frac{dE}{dx}\right)^{-1} dE \tag{1.5}$$

where E_0 is the initial kinetic energy of the particle. Due to energy loss straggling, the range of particles with same initial energy will have a range distributed around a mean value (see Figure 1.4). Statistical fluctuations of range are called *range straggling*.

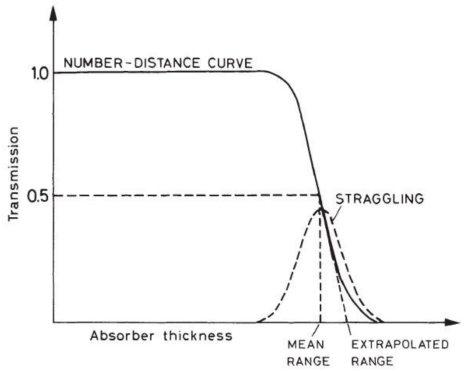

Figure 1.4: Fraction of transmitted particles as a function of depth in the medium. The mean value of the range and its distribution, which is approximately Gaussian, are also shown [1].

It can be shown that the integration of Eq. 1.5 leads to:

$$R(v) = \frac{m}{z^2} F(v) \tag{1.6}$$

where F(v) is a function of the initial velocity of the particle. From this formula, a useful scaling law can be derived for two particles, a and b, with the same velocity, but different mass and charge, traversing the same medium [5]:

$$R_a(v) = \frac{m_a z_b^2}{m_b z_a^2} R_b(v) \tag{1.7}$$

allowing for the comparison of ranges based on their masses and atomic numbers. For example, for a proton and a Carbon nucleus, it can be found that $R_p = 3R_C$.
The relation between the range of a particle and its initial kinetic energy E is well approximated by the formula

$$R(E) = \alpha E^p \tag{1.8}$$

where α is a constant that depends on the material, and p is a constant that depends on the incoming particle. The value of p is generally around 1.75 for many particles. From this formula, it is clear that the range value, and thus the position of the Bragg peak, depends only on the kinetic energy of the particle.
The range fluctuations σ_R are directly related to the energy loss straggling, and it can be shown that the following holds:

$$\frac{\sigma_R}{R} = \frac{1}{\sqrt{m}} f\left(\frac{E}{mc^2}\right) \tag{1.9}$$

The range straggling, along with multiple Coulomb scattering, explained in the following section, are important factors to be taken into account for hadrontherapy treatment, as will be better explained in Section 2.1.1.

1.1.3 Multiple Coulomb Scattering

A charged particle passing through matter can also suffer repeated elastic Coulomb scatterings from nuclei. This process is much less probable with respect to the energy loss process described so far. The cross section of these individual collisions is given by the Rutherford formula

$$\frac{d\sigma}{d\Omega} = \left(\frac{Z_1 Z_2 \alpha \hbar c}{4E_0}\right)^2 \frac{1}{\sin^4\left(\frac{\theta}{2}\right)} \tag{1.10}$$

where Z_1 and Z_2 are the charges of the incident particle and the nucleus involved in the collision, α is the fine structure constant ($\approx 1/137$), $\hbar$ is the reduced Planck constant, E_0 is the energy of the incident particle, and θ is the scattering angle.
These collisions result in numerous small angular deflections of the particle and their total effect is to deviate the incident particle from its initial direction, as shown in Figure 1.5.

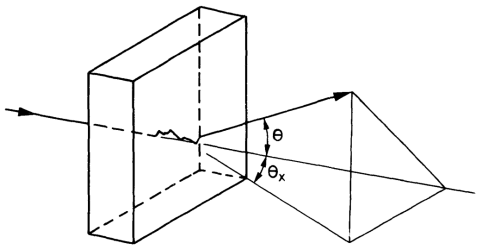

Figure 1.5: Multiple scattering of a charged particle [1] .

If the average number of independent scatterings is big enough (> 20), and energy loss is negligible, the problem can be treated statistically. The distribution of the scattering angles is described by the Molière's theory [6]. In the first order approximation, the distribution can be modeled as a Gaussian with mean 0 and standard deviation

$$\sigma_\theta = \frac{13.6MeV}{\beta cp} z \sqrt{\frac{x}{X_0}} \left[1 + 0.038 \ln \frac{x}{X_0}\right] \tag{1.11}$$

where p is the momentum of the incident particle, z is the charge of the incident particle, and x/X_0 is the length crossed in the material in units of radiation length X_0, defined as the thickness of material required to reduce the particle's energy to $1/e$ of its initial value. The value of the radiation length is equal to:

$$X_0 = \frac{A}{4\alpha N_\alpha Z^2 r_e^2 \ln(183 Z^{-1/3})} \tag{1.12}$$

where Z and A are referred to the medium and α is the fine structure constant.

1.2 Nuclear interactions

Even though less frequent than electromagnetic interactions, nuclear interactions are also present in the energy range relevant to hadrontherapy and space radioprotection, playing an important role as explained in Section 2.1.2. These interactions are mediated by the strong force and have a very short range, of the order of 1 fm, which is roughly the size of a nucleon. For a nuclear interaction to occur, the energy of the particles involved must overcome the Coulomb barrier.
Nuclear interactions can be either elastic or inelastic. Elastic interactions do not change the structure of the projectile or the target and they do not produce any additional particles; their primary effect is the deflection of the primary particle beam and a change of the kinetic energy.
Inelastic nuclear interactions, on the other hand, can lead to two different processes: nuclear excitation and nuclear fragmentation. In the first case, the nuclei involved become excited, followed by de-excitation with the emission of γ rays in the range of 0-10 MeV. The second type of reaction modifies the nucleon composition of the involved nuclei [7], without changing the overall number of nucleons, resulting in the emission of lighter particles (*fragments*) from the breakup of the target. If the projectile is a nucleus different from a proton, which does not fragment at these energies, projectile fragmentation can also take place.
Fragments from the projectile typically have a similar energy per nucleon as the original particle but lower charge, resulting in a longer range due to the dependence of stopping power on charge. In contrast, fragments from the target are generated with very low velocities and stop after traveling only few micrometers. Both types of fragments can release energy in the medium, leading to potential collateral effects in the case of hadrontherapy.

1.2.1 Nuclear fragmentation

The process of nuclear fragmentation is the most frequent among nuclear interactions in the energy range of interest and can be explained with a multiple stage process, as described more in detail in [8].
In the first stage, known as the *intra-nuclear cascade* (INC), the target and projectile interacts through a series of two-body interactions among nucleons [9]. These interactions occur on an extremely short timescale, approximately 10^{-22} seconds and protons, neutrons, and light fragments may be emitted. The system enters then in the *pre-equilibrium* phase, where the nuclei have not yet reached thermal equilibrium. This phase is characterized by further nucleon-nucleon collisions. During this process, additional protons, neutrons, and light fragments are emitted and the process is still relatively rapid. Finally, in the *de-excitation* step (10^{-18} to 10^{-16} s), the nucleus dissipates its remaining excitation energy through various mechanisms. Light fragments are emitted in a process known as *nuclear*

evaporation. For light nuclei, if the excitation energy is enough, the nucleus undergo a Fermi break-up, disassembling into smaller fragments. In cases where heavy nuclei are involved, fission can occur, though this is less relevant in contexts such as hadrontherapy. If the residual nucleus remains excited, it returns to its ground state through gamma emission.

1.2.2 Nuclear cross section

A fundamental parameter to understand nuclear processes is the *cross section*. This quantity measures the probability of a reaction occurring. Considering a beam of particles passing through a material composed of uniformly distributed scattering centers, the cross section σ quantifies the probability that an incident particle will interact with a scattering center. The number of scattering centers encountered by the beam is proportional to the material thickness δx, the target area perpendicular to the beam A, and the density n_t of these centers. The density of scattering centers in the target per unit volume is given by:

$$n_t = \frac{\rho_t N_A}{A_t} \tag{1.13}$$

where ρ_t is the target mass density, A_t is the target mass number, and N_A is Avogadro's number. Given the beam flux ϕ, the average number of scattered particles N_s is [1]:

$$N_s = \phi \sigma n_t A \delta x \tag{1.14}$$

where σ is the cross section. It is also possible to define the differential cross section by considering the number of particles scattered into a specific solid angle Ω or at a specific kinetic energy E_{kin}, and also the double differential cross section $\frac{d^2\sigma}{d\Omega dE_{kin}}$. From this, the cross section is obtained from:

$$\sigma = \int_0^{\Omega} \int_0^{\infty} \frac{d^2\sigma}{d\Omega dE_k} \, dE_k \, d\Omega. \tag{1.15}$$

A possible way to describe nuclear reactions is through microscopic models, where nuclear interactions are expressed in terms of a sum of individual nucleon-nucleon (N-N) scattering processes. One of the most successful microscopic model is given by the *Glauber model* [10].
Following the implementation of the model in [11], the local mean free path is given by:

$$\Lambda(r) = [\rho(r)\sigma_T^{\overline{NN}}]^{-1} \tag{1.16}$$

with $\rho(r)$ the nuclear matter density and $\sigma_T^{\overline{NN}}$ the N-N total scattering cross section averaged over isospin. Averaging over the mean free path of different incident nucleons in the target, the mean free path can be extended to:

$$\Lambda(r) = \left[\sigma_T^{\overline{NN}} \int d\Omega \int_V d\vec{s} \, \rho_p(\vec{s}) \rho_t(\vec{r} - \vec{s}) \right]^{-1} \tag{1.17}$$

where r is the distance between the centers of the colliding nuclei, ρ_p and ρ_t are the nuclear density distributions of respectively projectile and target, V is the nuclear volume overlap at the distance r, s is the position variable for the integration over V and $d\Omega$ is the angular part of $d\vec{r}$ [11]. Integrating over the whole trajectory of the projectile, it is possible to obtain the probability of no N-N interaction (trasparency function):

$$T(b) = \exp\left[\int_{-\infty}^{+\infty} -\frac{dz}{\Lambda(r)}\right] \tag{1.18}$$

with b impact parameter and z the distance with respect to the beam axis, hence $r^2 = b^2 + z^2$. Finally the reaction cross section σ_R is derived assuming that any N-N scattering process leads to a nuclear reaction event and it is given by integrating the complementary of $T(b)$:

$$\sigma_R = \int_0^{+\infty} 2\pi b[1 - T(b)]db. \tag{1.19}$$

This model is validated for high-energy collisions, where the projectile trajectory can be considered straight. Correcting the model taking into account electromagnetic and nuclear field effects on the trajectory, the model can be extended to lower energies [12] (around 10-1000 MeV/u). Further corrections also take into account the Pauli exclusion principle and Fermi motion of nucleons inside target nuclei.
Other more empirical descriptions start from taking the geometrical interpretation of the cross section: the reaction cross section can be considered as the overlapping area between the target and the projectile nucleus. The area of a nucleus, in a first approximation, is proportional to the mass number raised to the power of 1/3, and so a first empirical model (Bradt and Peters [13]) is given by:

$$\sigma_R = \pi r_0^2 \left(A_p^{1/3} + A_t^{1/3} - b\right)^2 \tag{1.20}$$

where $r_0 \simeq 1.25\,\mathrm{fm}$ is the nucleon radius, A_p and A_t are the projectile and target mass numbers, respectively, and b is an overlapping parameter. However, this formula is energy-independent and is valid only for nuclei with energy $> 1.5\,\mathrm{GeV/u}$. In a more refined model, an energy-dependent empirical constant can be multiplied to the formula, and another one can substitute the b parameter.
A cross section model for nuclear inelastic interactions, expressed in terms of the energy dependent total proton-proton cross section σ_{pp}^{tot} and proton-neutron cross section σ_{pn}^{tot}, valid in the energy range from $30\,\mathrm{MeV/u}$ to $1\,\mathrm{GeV/u}$, is:

$$\sigma_r = \pi C(E)\left(\sqrt{\sigma_{pp}^{tot}(E)Z_p^{2/3} + \sigma_{pn}^{tot}(E)N_p^{2/3}} + \sqrt{\sigma_{pp}^{tot}(E)Z_t^{2/3} + \sigma_{pn}^{tot}(E)N_t^{2/3}}\right)^2 \tag{1.21}$$

with Z_p and N_p (Z_t and N_t) the number of protons and neutrons of the projectile (target), and $C(E)$ an energy-dependent empirical parameter. In Figure 1.6, the prediction of this model along with experimental data is shown for proton-^{12}C and ^{12}C-^{12}C [14].

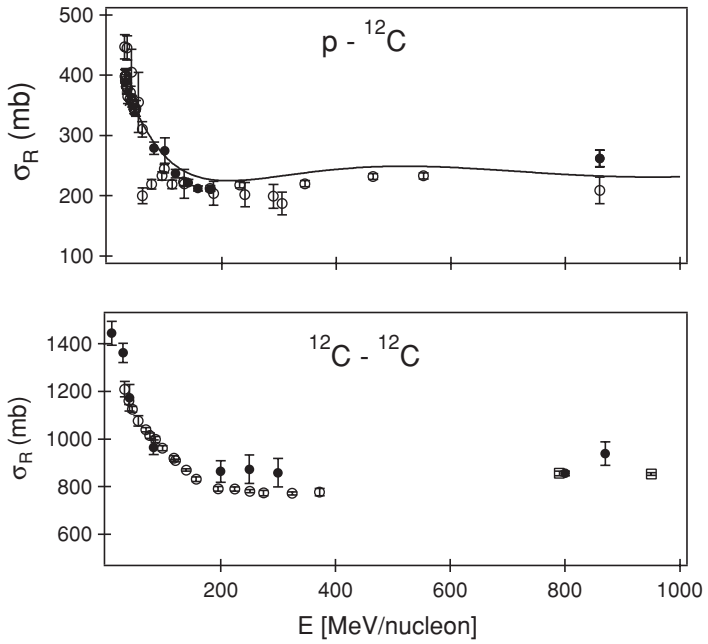

Figure 1.6: Total cross sections for proton-^{12}C and ^{12}C-^{12}C as a function of energy per nucleon [14]. The solid line represents the prediction of Eq. 1.21, and the experimental data are taken from [15][16].

A more detailed understanding of fragmentation requires to consider not only the total reaction cross section but also the cross section for each individual fragment produced. This is particularly important for applications in hadrontherapy and space radioprotection, where accurate knowledge of the behavior and effects of all fragments is essential for effective treatment and safety measures. Unfortunately, the current literature on these specific cross sections remains quite limited.

Chapter 2

Hadrontherapy and space radioprotection

In this chapter, I will focus on two key applications of charged particles relevant to my thesis work: hadrontherapy and space radioprotection. Hadrontherapy is a cancer treatment technique that uses charged particles to target cancer cells, while space radiation protection aims to shield astronauts and electronics from harmful space radiation. The following sections will introduce these topics, underling the effects of nuclear fragmentation.

2.1 Hadrontherapy

Cancer, also known as neoplasm, is a cellular mutation that proliferates within an organism, growing and multiplying in a disordered manner with respect to normal cells. Sometimes, cells from the tumor mass detach from the original site and migrate through the lymphatic system or bloodstream to other parts of the body, forming new tumors known as metastases. The unchecked growth of these cells can be fatal.
According to the World Cancer Research Fund, in 2022, over 18 million new cancer cases were reported worldwide, with nearly 10 million deaths linked to the disease [17]. For this reason, the medical field is constantly looking for improvements and more effective treatments.
Currently, depending on the type and stage of the cancer, different types of treatments are used: chemotherapy, immunotherapy, oncological surgery, radiotherapy, and hadrontherapy. The first three methods do not use radiation and are therefore referred to as non-radiative therapies. If the tumor has already formed metastases, therapies that can affect the entire body are used, such as chemotherapy and immunotherapy. In the former case, the treatment involves administering drugs that can destroy cells and prevent their growth; in the latter case, the approach is to act on the immune system by training it to recognize tumor antigens that are mutated compared to the healthy ones. A localized

and easily reachable tumor can be surgically removed, and then the treatment can be supported by chemotherapy or radiotherapy sessions. When the tumor is not reachable with surgery, radiotherapy and hadrontherapy are used.
Radiotherapy involves irradiating the tumor area with electromagnetic radiation beams to damage the DNA of the cancerous cells. The objective is to inflict enough damage to prevent cancer cell reproduction.
Hadrontherapy relies on the same basic idea of damaging cancer cells, but instead utilizes beams of charged particles, such as protons or heavy ions, accelerated through particle accelerators.
Hadrontherapy was first proposed by Robert Wilson [18], one of the founders of Fermilab, who studied the energy release characteristics of proton beams in matter. The first hadrontherapy treatment took place at the Lawrence Berkeley National Laboratory in 1952. Today, there are more than 100 facilities in operation worldwide and around 30 more under construction or expansion [19]. Italy hosts the CNAO (National Center for Oncological Therapy) in Pavia, one of the most prestigious and important facilities worldwide. Operational since 2011, the CNAO uses both proton beams up to 250 MeV and Carbon ion beams up to 400 MeV/u, accelerating them through a synchrotron (in Figure 2.1). CNAO is one of the few facilities that uses Carbon ions and has three different rooms reached by the beam, two for treatment and one experimental room. The facility is now building new treatment rooms and aims to start accelerating He-ions as well as constructing a facility for Boron Neutron Capture Therapy (BNCT) [20].

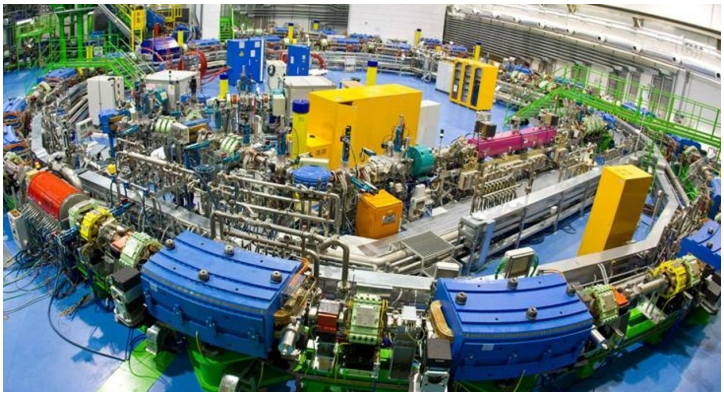

Figure 2.1: Picture of the synchrotron at CNAO [21].

In 2015, the Proton Therapy Center was also inaugurated in Trento, utilizing proton beams in the range of 60-230 MeV, with a 360° adjustable orientation. Starting in 2023, a proton center has also become operational at the European Institute of Oncology (IEO) in Milan. A new proton center has also been built at the CRO (Centro di Riferimento Oncologico) in Aviano.

2.1.1 Principles of hadrontherapy

As already mentioned, hadrontherapy treatment is based on damaging cancer cells using a beam of charged particles. Currently, the particles used in hadrontherapy centers are predominantly proton beams and ^{12}C ions. However, ongoing research is exploring the potential use of Helium and Oxygen ions in treatment. In hadrontherapy, particle kinetic energies typically range from approximately 60 MeV/u to 400 MeV/u for heavier particles like Carbon ions. The main advantage of hadrontherapy over conventional radiotherapy is its different dose profile. In radiobiology, the dose D quantifies the amount of radiation absorbed and is defined as the energy absorbed dE per unit mass dm:

$$D = \frac{dE}{dm}. \tag{2.1}$$

The absorbed dose is measured in Gray, 1 Gy = 1 J/kg. The dose does not account for the varying biological effects of different types of radiation, so the *equivalent dose* is introduced, calculated by applying a weighting factor w_R to the absorbed dose to reflect the impact of the radiation type. Considering different radiations R the equivalent dose is given by:

$$D_{eq} = \sum^{R} w_R D_R \tag{2.2}$$

where D_R is the dose of a specific radiation R and w_R is its weight. The equivalent dose is measured in Sievert (Sv).
As previously discussed in Section 1.1.1, charged particles release minimal energy at the beginning of their path. The maximum energy release occurs at the *Bragg peak*, located near the end of the path, just before the particle comes to a stop, defining the particle's range. This property is related to the behavior of the energy loss described by Eq. 1.2. Since the energy loss is proportional to $1/\beta^2$, when the particle's energy is high, its energy loss is low. As the particle slows down, the energy loss increases steeply, leading to the complete loss of the particle's energy in a relatively small region. Photons, on the other hand, have a maximum energy release within a few centimeters of entering the medium (see Figure 2.2).
The position of the *Bragg peak* is directly related to the initial energy of the incident beam (see Eq. 1.8): the higher the beam's energy, the greater the depth it can penetrate, as illustrated in Figure 2.2.

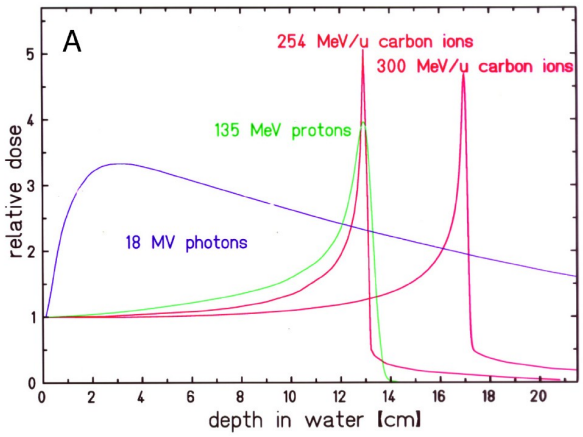

Figure 2.2: Depth-dose distribution comparison between photon, protons, and Carbon ion beams in water at therapeutic energies. From this plot, it is also possible to notice the variation in the position of the Bragg peak for Carbon ions at different energies [22].

Thanks to this characteristic of charged particles, the maximum dose can be delivered exactly at the tumor site, optimizing therapeutic effectiveness and minimizing damage to surrounding healthy tissues (see Figure 2.4). This is particularly important in the presence of *Organs At Risk* (OAR) near the tumor area and in pediatric tumors, where precision in the treatment is of extreme important due to the small size of the patient. The *Bragg peak* is relatively narrow, on the order of millimeters, while a tumor can easily reach several centimeters. Therefore, a single energy beam is generally insufficient. Instead, a combination of monoenergetic beams at different energies is used, creating what is known as the Spread-Out Bragg Peak (SOBP) [23], which consists of overlapping multiple peaks to cover the entire tumor volume (see Figure 2.3). This method allows for more precise and effective treatment of irregularly shaped or larger tumors by ensuring the dose distribution matches the tumor's extent.

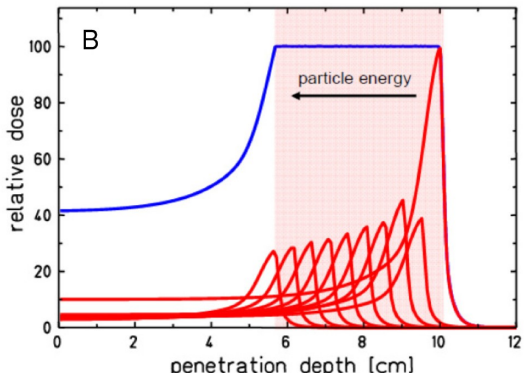

Figure 2.3: Spread Out Bragg Peak (SOBP) [22].

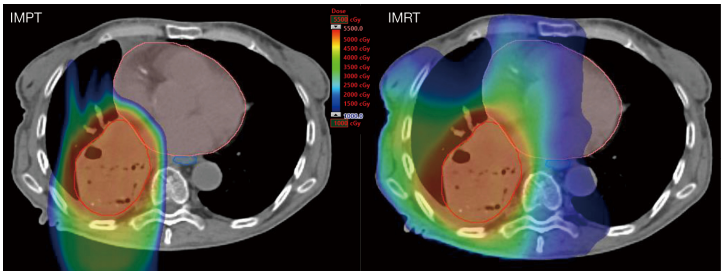

Figure 2.4: Dose distribution in the treatment of lung cancer using Proton Therapy (left) compared to Intensity Modulated Radiation Therapy (right). Two organs at risk are highlighted: the esophagus in blue and the heart in pink [24].

In hadrontherapy treatment, it is also essential to consider both *range straggling*, which can cause variations in the path length of the particles, and the effect of Multiple Coulomb Scattering with nuclei, which laterally deflects the beam. Treatment planning must account for these variations as they can slightly alter the dose distribution in the patient. For instance, when considering a proton beam of 200 MeV in water, which largely composes the human body, the fluctuations in range, approximately 25.8 cm, are around 2.5 mm, and the lateral displacement is about 5 mm. In Figure 2.5, the lateral spread of different ions in water as a function of energy is shown. Heavier ions tend to suffer less from scattering, resulting in a smaller lateral spread.

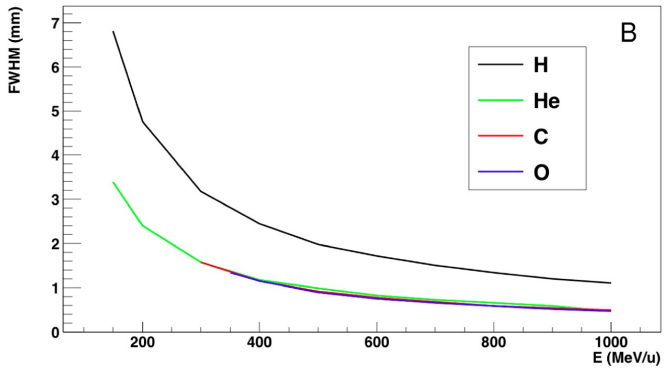

Figure 2.5: Lateral spread of different ions as a function of the energy of various beams after traversing 15 cm in water, calculated using the Monte Carlo Code Geant4 [22].

Another significant advantage of hadrontherapy over conventional radiotherapy is its higher biological effectiveness. The delivered, and consequently absorbed, dose is not a sufficient parameter to understand the DNA damage caused by radiation. The same dose of different types of radiation can result in significantly different levels of damage to cancer cells.
The *Linear Energy Transfer* (LET) is a physical factor that represents the energy released

per unit length along the track of the primary beam and is directly related to the stopping power defined in Eq. 1.2:

$$\mathrm{LET} = \left(\frac{dE}{dx}\right)_{\Delta} \tag{2.3}$$

where Δ represents a cut-off value to exclude higher energy losses.
Ionizing radiations are classified as low-LET radiation, as in the case of X-rays ($\sim$ 1 keV/μm), or high-LET, as in the case of hadrons ($\sim$ 10–100 keV/μm). Photons generally interact only once within the human body, resulting in few ionizations inside the cell, which are responsible for damage. In contrast, hadron beams interact more frequently, producing more ionizations and leading to more substantial and often irreparable DNA damage.
The effectiveness of radiation in killing cells can be quantified by defining the *Relative Biological Effectiveness* (RBE). This quantity is the ratio between the dose of reference radiation D_X (typically γ-rays from ^{60}Co decay) and the dose D of another type of radiation required to achieve the same biological effect:

$$\mathrm{RBE} = \left(\frac{D_X}{D}\right)_{\text{same effect}} \tag{2.4}$$

By definition, photons have an RBE equal to 1, while it is higher for hadrons, being ~ 1.1 for protons and $\sim 3-4$ for Carbon ions. In general, RBE depends on the LET of the radiation, but also on the type of radiation and the type of cell being damaged. It generally increases with LET, reaching a peak around $100-200\,\mathrm{MeV}/\mu\mathrm{m}$, and then decreases due to overkilling effects (when cells receive more dose than necessary to cause their death). The position of this peak shifts to higher LETs for heavier ions.

2.1.2 Effects of nuclear fragmentation

At the energy range of hadrontherapy, the most frequent nuclear interaction process is nuclear fragmentation. In this type of treatment, nuclear fragmentation can have a non-negligible impact.
Fragments have different charge and mass compared to the primary beam and, for this reason, following Eq. 1.2, their energy deposition will be different. Fragments can alter the dose profile of the primary beam, releasing dose in healthy tissues and potentially causing damage, as well as lead to loss of the primary beam. In particular, it is possible to distinguish between two types of fragmentation, with different consequences: projectile fragmentation and target fragmentation.

Projectile fragmentation

In hadrontherapy, protons and heavier nuclei are used. Considering the energies employed, protons do not have enough energy to fragment, and structures below the nucleons are

not explored. However, when the primary beam is a heavier nucleus, such as Carbon, it can interact with atoms in the human body and undergo fragmentation.

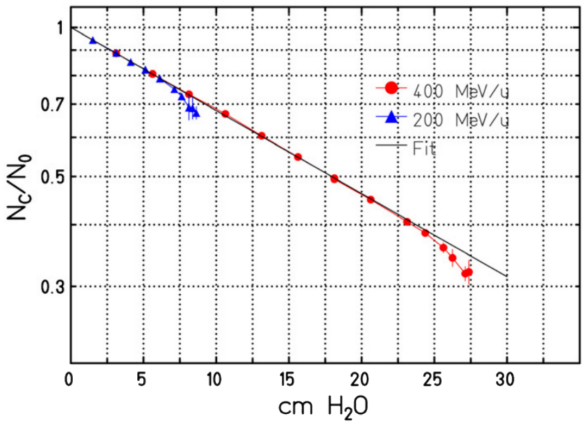

Figure 2.6: Measured attenuation of a Carbon beam of 200 MeV/u and 400 MeV/u in a thick water absorber [25].

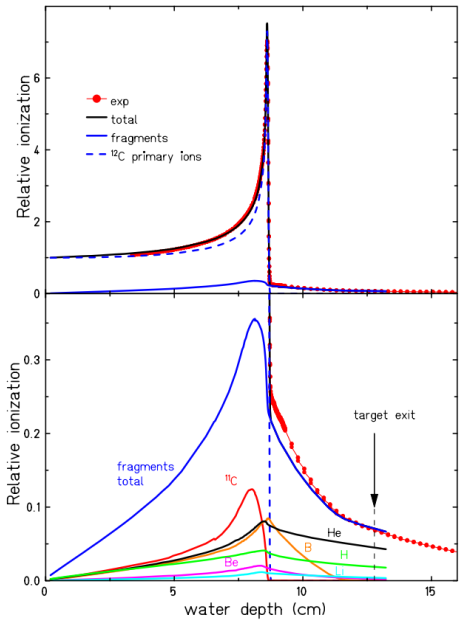

Figure 2.7: Ionization function of a 200 MeV/u ^{12}C ion beam in water. The calculations are made with a Monte Carlo code (Particle and Heavy Ion Transport Code System (PHITS)). The magnified ordinate scale below shows the contribution of fragments with different atomic numbers Z [26].

Projectile fragmentation is not negligible and results in a loss of the primary beam: for a 200 MeV/u ^{12}C beam in water, around 60% of primary ions reach the Bragg peak. For 400 MeV/u ^{12}C, the situation is even worse, with only 30% of primary ions reaching the peak, as shown in Figure 2.6. Most of these nuclear interactions are peripheral, with only a few nucleons participating in the interaction, meaning that fragments will travel at nearly the same velocity as the primary ion. Low-Z fragments with the same velocity as the projectile will have a longer range (see Eq. 1.7). This results in a *fragmentation tail*, which is a dose release beyond the *Bragg peak* caused by the fragments (see Figure 2.7). At higher beam energies, as well as for heavier nuclei, the probability of nuclear fragmentation increases, leading to the production of more fragments.

Target Fragmentation

Target fragmentation can also play an important role in hadrontherapy, especially in the case of proton therapy, where protons do not fragment. As protons travel through the human body, they can undergo nuclear interactions with atoms in the tissues. These nuclear interactions are not negligible; before the Bragg peak, 30% of protons at around 250 MeV undergo inelastic nuclear interactions with human body nuclei, as shown in Figure 2.8a. Figure 2.8b illustrates the contribution of nuclear interactions to cell killing: before the Bragg peak, the ratio of cells killed by fragmentation reactions to those killed by ionization is around 1/10, a pretty significant contribution.

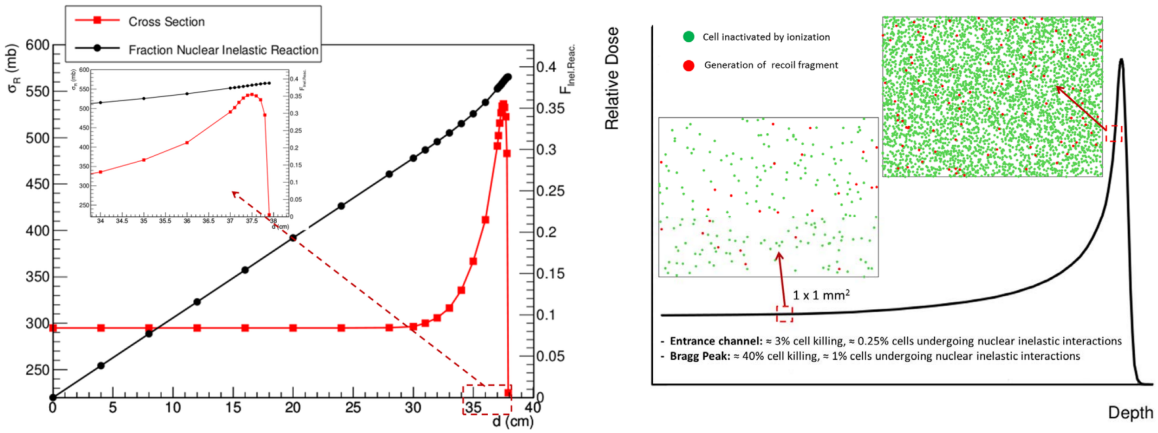

(a) (b)

Figure 2.8: In Figure 2.8a, the fraction of primary protons undergoing inelastic nuclear reactions in water for an initial beam energy of 250 MeV, along with the total cross section; in Figure 2.8b, the fraction of cell killing caused by ionization and fragmentation reactions along the trajectory of a proton beam [27].

Target fragmentation particularly affects the entrance channel of the human body, before

the peak. Fragments produced from the target typically have very low energy since the target (human body nuclei) is almost at rest. For this reason, these fragments can travel only a few μm before stopping, releasing their energy where they are produced, along the path of the particle. Since they travel a short distance and almost do not leave the target, studying target fragment production is extremely difficult.

Fragment	**E (MeV)**	**LET (keV/μm)**	**Range (μm)**
^{15}O	1.0	983	2.3
^{15}N	1.0	925	2.5
^{14}N	2.0	1137	3.6
^{13}C	3.0	951	5.4
^{12}C	3.8	912	6.2
^{11}C	4.6	878	7.0
^{10}B	5.4	643	9.9
^{9}Be	6.4	400	15.7
^{6}Li	6.8	215	26.7
^{4}He	6.0	77	48.5
^{3}He	4.7	89	38.8
^{2}H	2.5	14	68.9

Table 2.1: Range for fragments at different energies with their corresponding LET [27].

In Table 2.1 ranges of different fragments at different energies coming from the target are represented: even the lighter ones travel less than 100 μm. Unfortunately, the data available on nuclear fragmentation of the target, as described in Section 2.3, are limited.

2.1.3 Dose verification system: the He-check idea

Various uncertainties can arise in hadrontherapy, affecting the treatment plan and necessitating an increase in safety margins, which can potentially reduce the benefits of the treatment. These uncertainties can arise from factors such as anatomical changes, setup errors, and inaccuracies in determining proton stopping power across different materials. To address these issues, several dose verification systems have been developed. However, implementing a real-time verification system that provides information on the ion beam range within the patient during treatment sessions would be the best solution for mitigating these uncertainties. At the Centro Nazionale di Adroterapia Oncologica (CNAO), a facility for hadrontherapy, where both protons and Carbon ions are used for cancer treatment, a project named He-check is being developed to perform dose verification during patient treatment sessions.
The He-Check system concept involves the simultaneous use of ^{12}C and ^{4}He ions for therapeutic treatment and verification purposes, respectively.

Carbon ions (C^{6+}) and Helium ions (He^{2+}) can be accelerated together, due to the fact that they are characterized by almost the same magnetic rigidity R at the same velocity:

$$R = B\rho = \frac{pc}{q} \tag{2.5}$$

with B magnetic field used to accelerate the beam, ρ curvature radius and p and q momentum and charge of the particle. This results in a mixed beam in which the two species have the same energy per nucleon. It is important to specify that while the rest mass-to-charge ratio of the Carbon is 12/6 a.m.u., the ratio of He is 4.0026033/2 a.m.u. Given the same momentum, this slight difference in ratios results in a small difference in magnetic rigidity between the two ions, causing their orbits within the same magnetic field to have different radii. The accelerator's extraction mechanism at CNAO utilizes a betatron core to push the beam stacks towards resonance. Due to their slightly different magnetic rigidities, Helium particles reach resonance first and are consequently extracted first. Therefore, to utilize the mixed beam, it is necessary to discard the initial part of the extracted beam, which consists only of Helium, and the final part, which consists only of Carbon.
Carbon and Helium ions have also different ranges in matter due to their mass and charge differences. Using Eq. 1.7,it is found that the range of Helium is approximately three times that of Carbon.
Thanks to their nearly equal magnetic rigidity and differing ranges, it is feasible to use a system in which both beams are accelerated simultaneously. The carbon beam deposits its dose to the tumor, while the Helium beam passes through the patient and releases its energy in a detector. By measuring the position and residual range of the Helium ions exiting the patient, it is possible to reconstruct the traversed density and thickness, thus achieving real-time verification.
Figure 2.9 illustrates a schematic representation of the He-Check system.

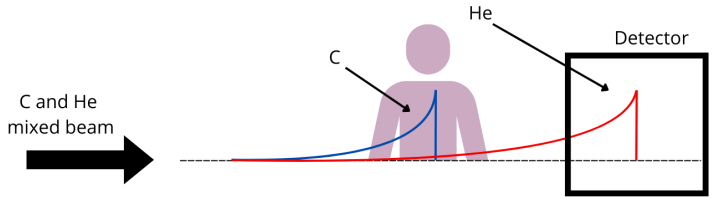

Figure 2.9: Schematic representation of the He-check idea.

During my master's studies, I spent a period at the CNAO, working on the He-check project and studying its experimental setup. The comprehensive details of this work are presented in Appendix A.

2.2 Space Radioprotection

Today, space agencies around the world, including NASA and ESA, are showing an increasing interest in human missions to the Moon and Mars to explore new frontiers. However, one of the biggest challenges in these space missions is dealing with space radiation, which is a significant risk for space instrumentation and, more importantly, the health of astronauts. Thanks to the Earth's magnetic field and atmosphere, people are naturally shielded from most cosmic radiation on Earth. In space, there are no such protections, and as a result, radiation exposure strongly increases, potentially by more than a factor of 100 compared to the Earth's surface.
To understand and try to reduce risks during space missions, it is required a clear knowledge of the types and energy spectra of particles encountered in space, as well as their interactions with spacecraft materials and human tissues. The impact of cosmic radiation on human health is difficult to evaluate, particularly concerning nuclear interactions, producing secondary fragments. To have accurate risk assessments, precise modeling of interactions is needed, based on experimental data, currently very limited.

2.2.1 Space environment

Space radiation is different from that on Earth; it includes both protons and heavy ions and is also isotropic. The main sources of radiation in space are *Galactic Cosmic Rays* (GCRs) and *Solar Particle Events* (SPEs). GCRs originate from outside the Solar System, likely from supernovae or other high-energy sources. GCR energies span a broad range, up to 1×10^{20} eV. They consist mainly of protons and other nuclei (98%) and a small fraction of electrons (2%). Among nuclei, protons are predominant (85%), with Helium nuclei (14%), while heavier elements are about 1% [28]. Although heavier ions like Iron are less abundant, their higher charge leads to a significant contribution to the GCR equivalent dose. This is due to the substantial energy loss they cause, which is proportional to the square of their charge. Figure 2.10a shows the fluence of different ions in GCRs along with their contribution to dose and dose equivalent.
The Sun continuously emits particle radiation, primarily composed of protons and electrons, known as the solar wind. The intensity of these low-energy particles ranges from 10^{10} to 10^{12} particles per $\mathrm{cm^2\,s^{-1}\,sr^{-1}}$ [28]. With energies between 100 eV and 3.5 keV for protons, these particles are stopped within the first few hundred nm of skin, making them negligible in terms of radiation protection [28].
However, the Sun occasionally releases large bursts of energy, such as radio waves and X-rays, which can accelerate particles within the solar matter. These events are known as Solar Particle Events and result in the emission of ions, primarily protons and a small fraction of heavier nuclei, with energies reaching several GeV from the solar corona. SPEs are relatively rare phenomena, occurring approximately 5-10 times per year when the Sun is not at its minimum activity.

Solar activity also affects GCRs below GeV, as cosmic ray flux is lower during solar maximum compared to solar minimum, as shown in Figure 2.10b, while SPEs are more likely during solar maximum.

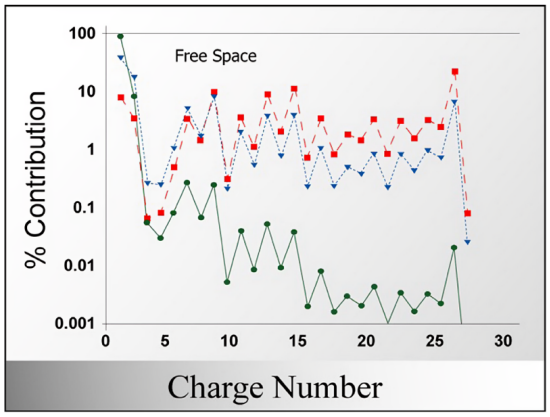

(a)

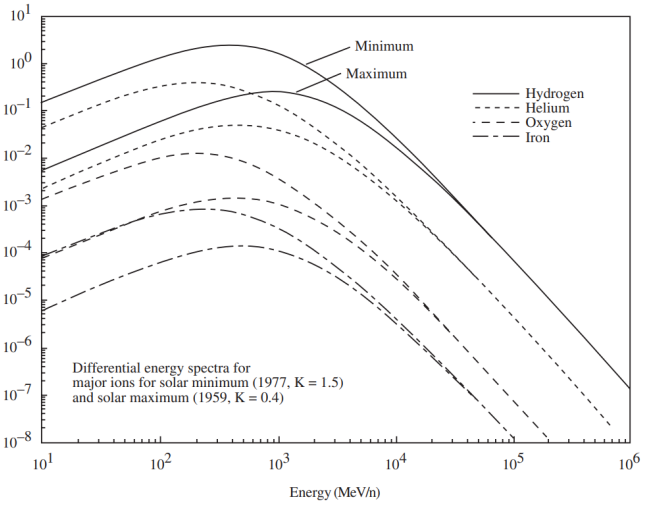

(b)

Figure 2.10: In Figure 2.10a the contribution of the different ions in the GCR in fluence (green), dose (blue), and dose equivalent (red) [28][29]; in Figure 2.10b GCR particle spectra for some ions at solar minimum and maximum [28].

2.2.2 Shielding

As already mentioned, space radiation is isotropic. This means that the only possible countermeasure that can be taken to provide protection against it is shielding, since there is no way to avoid radiation, and the exposure time depends on the duration of the mission. To achieve effective shielding, particle interaction properties must be exploited. As seen in Section 1.1, electromagnetic interactions make the particle lose energy until it stops, meaning that low-energy ions are easily stopped with small amounts of material. However the thickness of the shielding must be chosen carefully, also taking into account that the total mass of it should not be too much to avoid overloading the spacecraft. Even though protons are the primary component of space radiation, heavier ions contribute significantly to the overall effective dose. Therefore, in choosing the shielding and its thickness, it is important to account for the nuclear interactions of these heavy ions, as they can fragment inside it. The resulting fragments are generally lighter and consequently less harmful.
On the other hand, the linear energy transfer (LET) of ions decreases with the inverse square of their velocity, meaning that ions emerging from thicker shielding have higher LET, making them more harmful than they would be with thinner shielding.
To compare different shielding materials, the mass stopping power ($dE/d\chi$), already introduced in Eq. 1.3, and *mass thickness* or *areal density* expressed in gcm^{-2} are used. Using Eq. 1.2, the mass stopping power is proportional to the charge of the target material per unit mass (Z_t/A_t). This means that lighter materials have higher mass stopping power than heavier ones for the same mass thickness.

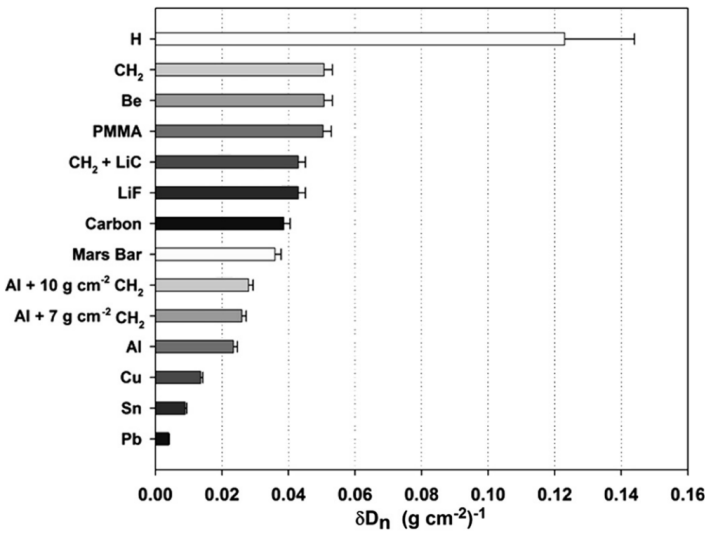

Figure 2.11: Dose attenuation properties of some shielding materials exposed to 1 GeV/n ^{56}Fe-ions [30].

Regarding nuclear interactions, from Eq. 1.20, the reaction cross section is proportional to $A^{2/3}$, so since the number of target nuclei per unit mass is equal to N_A/A_t, the reaction cross section becomes $\propto A^{-1/3}$. Again, lighter materials maximize the number of nuclear interactions per unit mass that can cause fragmentation, leading to dose reduction.
A particular case is liquid H_2. Because of its Z_t/A_t ratio, it has a very high *stopping power* compared to other materials. However, liquid hydrogen needs low-temperature storage, which is impractical for a spacecraft, and it also has high reactivity. For this reason, hydrogen-rich materials are taken into consideration.
The effectiveness of shielding design is evaluated through particle transport codes, and the accuracy of these models depends heavily on experimental data, which, as previously stated, are still very limited regarding nuclear fragmentation. Figure 2.11 shows the dose attenuation for different shielding materials.

2.3 Nuclear fragmentation data

In this section, I will present some data regarding nuclear fragmentation, coming from experiments as well as simulation codes. Both projectile and target fragmentation data are lacking, but the situation is worse for target fragmentation since measuring fragments produced by the target is difficult because they do not escape it.
The FOOT experiment, explained in Chapter 3, aims to provide precise measurements of nuclear fragmentation cross sections for all fragments produced in both projectile and target fragmentation.
A first measure of the proton total cross sections have been measured at CERN for different nuclei in the range from 180 to 560 MeV/u, range of interest for hadrontherapy, in [31] (see Figure 2.12).

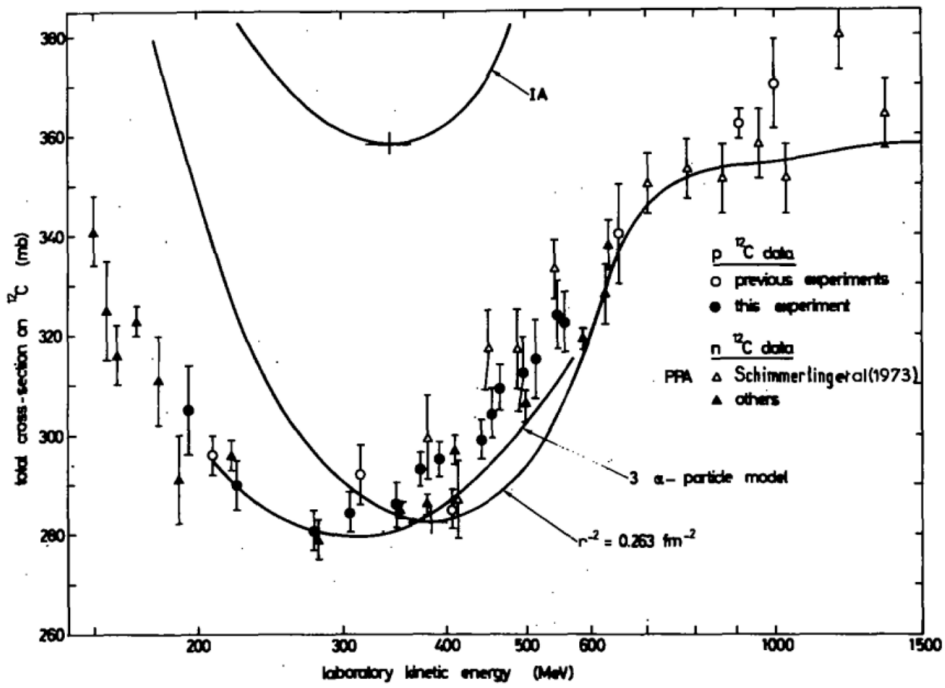

Figure 2.12: Total cross section of protons and neutrons against a target of ^{12}C together with theoretical predictions [31].

A review of the available interaction cross sections for protons below 250 MeV on carbon, oxygen, and calcium target is presented in [32], where the authors compared experimental data from the EXFOR [33] and Landolt-Börnstein databases [34] with different theoretical models, like TALYS [35], ICRU [36] and INCL [37]. In Figure 2.13 and Figure 2.14 some of these cross sections are shown. It is clear that for what regards target fragmentation, the data available are very limited, in particular for isotopic cross section.
Another interesting work has been performed at GANIL measuring the cross section products of a 95 MeV/u ^{12}C beam against thin targets [38], in Figure 2.15 the results for a Carbon target.
Concerning measurements relevant for space radioprotection, in [39] an extensive data collection that reports elemental and isotopic cross-sections, total and differential, for various target and projectiles at different energies was done. In Figure 2.16, as an example, ^{4}He cross section: each symbol on the plots represents all cross section measurements available for ^{4}He relevant to space radiation as a function of target and projectile charge.

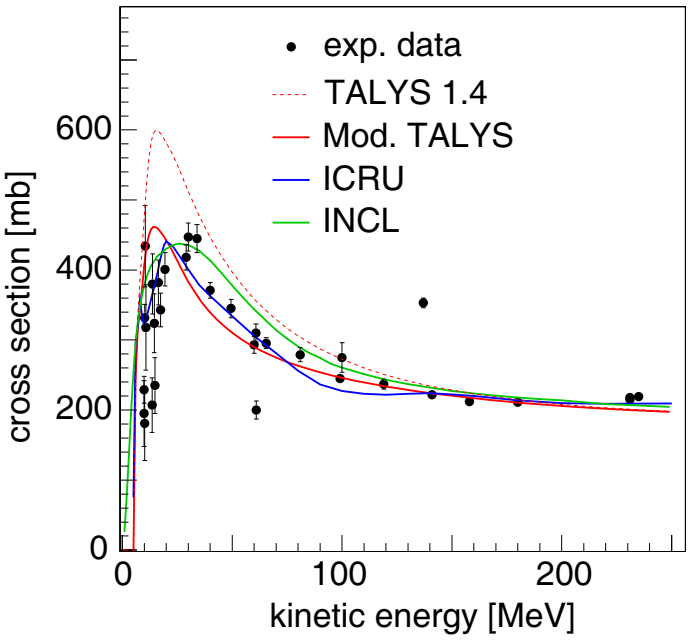

(a)

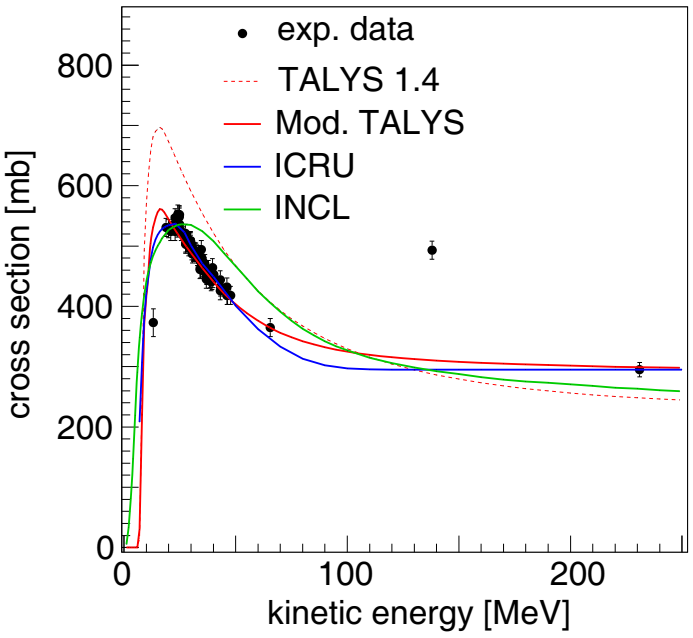

(b)

Figure 2.13: In Figure 2.13a the p + ^{12}C reaction cross section. Experimental data are drawn from the EXFOR database and are represented by black dots; results of TALYS 1.4 (dashed red), Modified TALYS (solid red), ICRU (solid blue) and INCL (solid green) are also shown. In Figure 2.13b the same, but for the p + ^{16}O reaction [32].

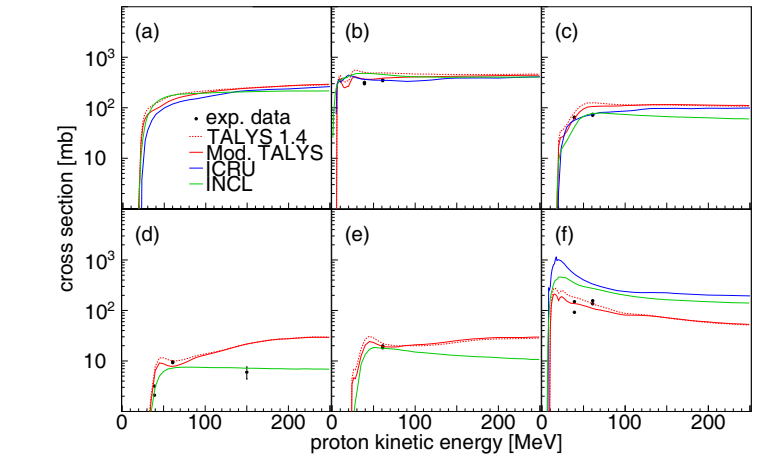

(a)

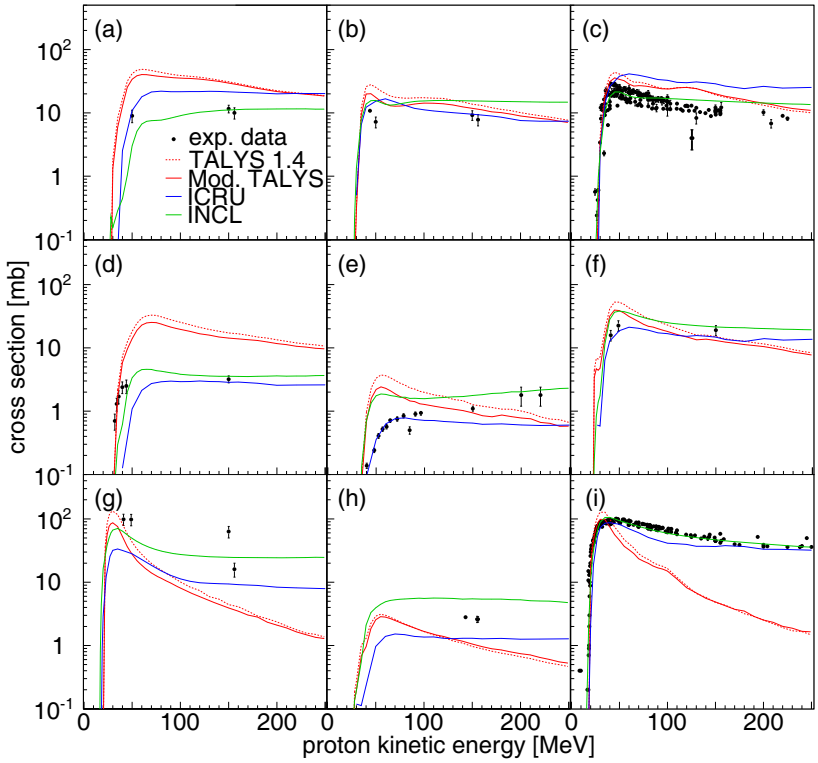

(b)

Figure 2.14: In Figure 2.14a cross section production of (a) neutrons, (b) protons, (c) deuterons, (d) tritons, (e) ^{3}He and (f) ^{4}He from the p + ^{12}C reaction. Experimental data are taken from [34] and are represented by black dots; results of TALYS 1.4 (dashed red), Modified TALYS (solid red), ICRU (solid blue) and INCL (solid green) are also shown. In Figure 2.14b the same, but for (a) ^{6}Li, (b) ^{7}Li, (c) ^{7}Be, (d) ^{9}Be, (e) ^{10}Be, (f) ^{10}B, (g) ^{11}B, (h) ^{10}C and (i) ^{11}C.

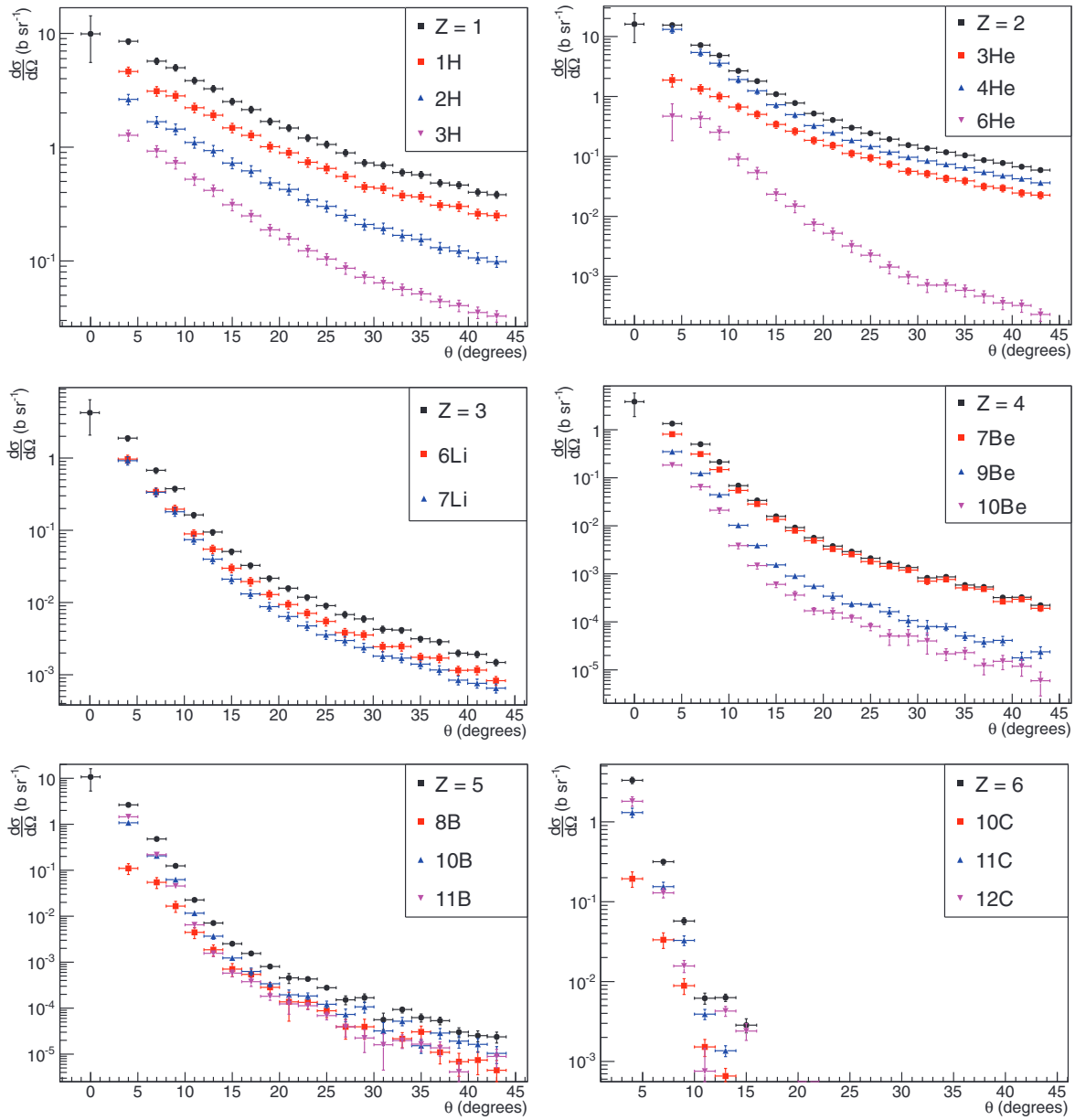

Figure 2.15: Angular distributions for fragments resulting from the fragmentation of a 95 MeV/u ^{12}C on a carbon target [38].

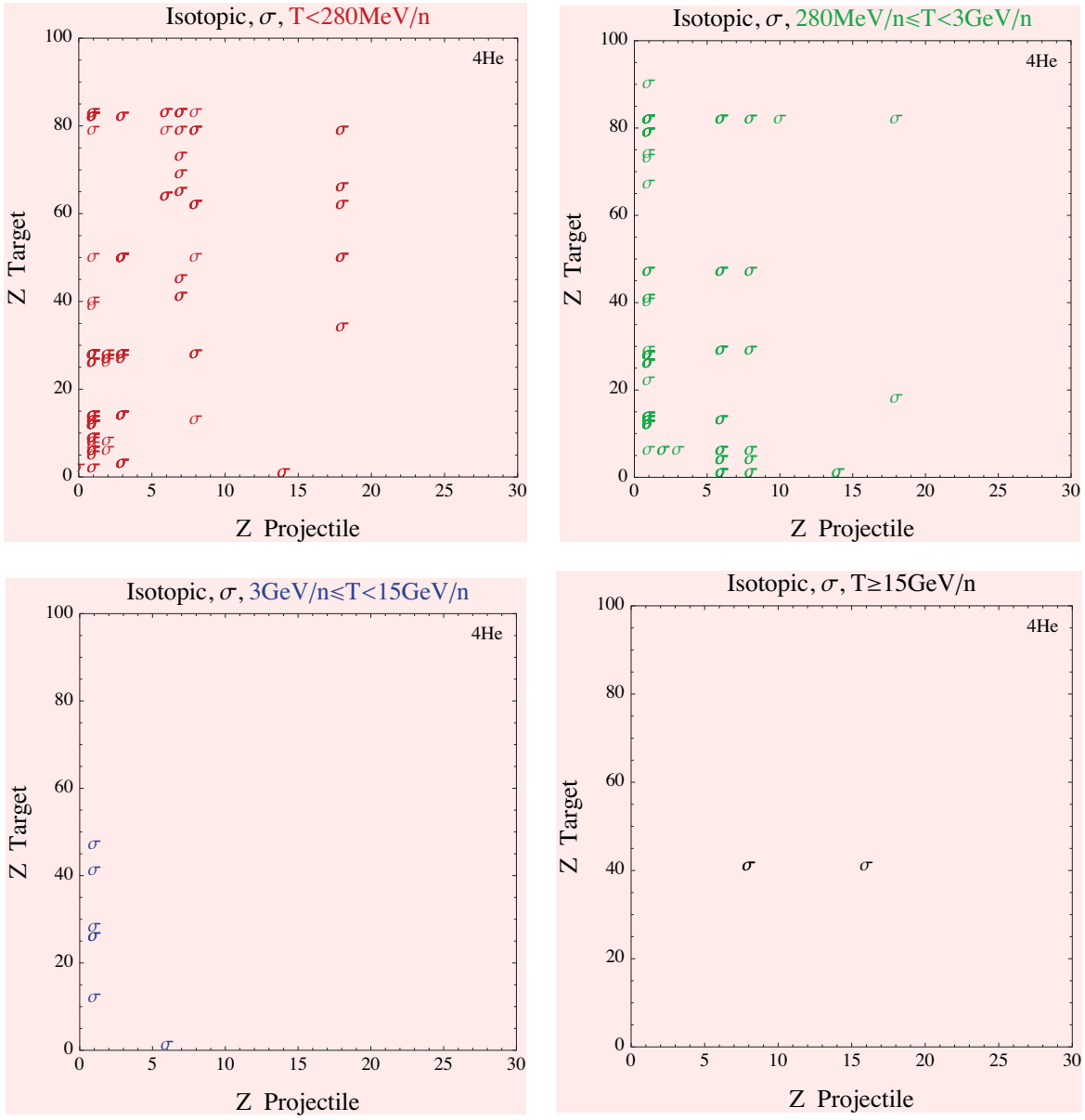

Figure 2.16: Isotopic cross section for ^{4}He fragments [39]: each symbol on the plots represents all cross section measurements available for ^{4}He relevant to space radiation as a function of target and projectile charge

Chapter 3

The FOOT experiment

The FOOT (FragmentatiOn Of Target) experiment was funded by the INFN (Istituto Nazionale di Fisica Nucleare) in 2017, and it is a collaboration involving researchers from ten INFN sections in Italy as well as several international universities and research institutions.
The objective of the FOOT experiment is to improve our understanding of nuclear fragmentation processes that can occur within the human body, both for applications in hadrontherapy and space radioprotection. Specifically, the experiment aims to increase the available experimental data by measuring the total and differential nuclear fragmentation cross sections for light nuclei (Z $\leq$8) in the energy range of interest, between 200 MeV/u and 400 MeV/u for hadrontherapy, and up to 800 MeV/u for space radioprotection. These measurements will help improve treatment planning systems and develop reliable models to be used in the field of space radioprotection: in both cases accurate nuclear data are required.
The FOOT experiment has already collected data at various research centers, including CNAO (Centro Nazionale di Adroterapia Oncologica) in Pavia, HIT in Heidelberg, and GSI in Darmstadt, Germany. This thesis will analyze data acquired at GSI in 2021, when the FOOT setup was not in its final setting.
Currently, the setup is complete, and a measurement was already taken at CNAO in 2023. Further measurements are planned for the future.

3.1 The goal and experimental approach

The final goal of the experiment is to measure the nuclear fragmentation differential cross section with respect to the production angle of the fragments ($d\sigma/d\Omega$) and the kinetic energy of the fragments produced ($d\sigma/dE_{kin}$) with an accuracy better than 10%, and the double differential cross section in kinetic energy and angle ($d^2\sigma/(d\Omega dE_{kin})$) with an accuracy better than 5%. To achieve these performances, the experiment must achieve a

precision of around 2-3% in charge identification capability and around 5% in isotopic identification capability of the fragments [40].
Monte Carlo simulations based on the FLUKA code [41][42] have predicted the energies and emission angles of fragments according to their mass, necessary for designing the experiment effectively. In Figure 3.1, the kinetic energy and emission angle of nuclear fragments produced from the interaction of a ^{16}O beam at 200 MeV/u with a C_2H_4 target are shown. Lighter fragments ($Z < 3$) have a wider emission angle, whereas heavier fragments are primarily emitted in the forward direction. For this reason, the FOOT experiment consists of two different experimental setups:

- an electronic setup optimized for fragments with $2 \leq Z \leq 8$, with an angular acceptance of 10°
- a setup based on an emulsion spectrometer optimized for low-Z fragments, with an angular acceptance of up to 60°.

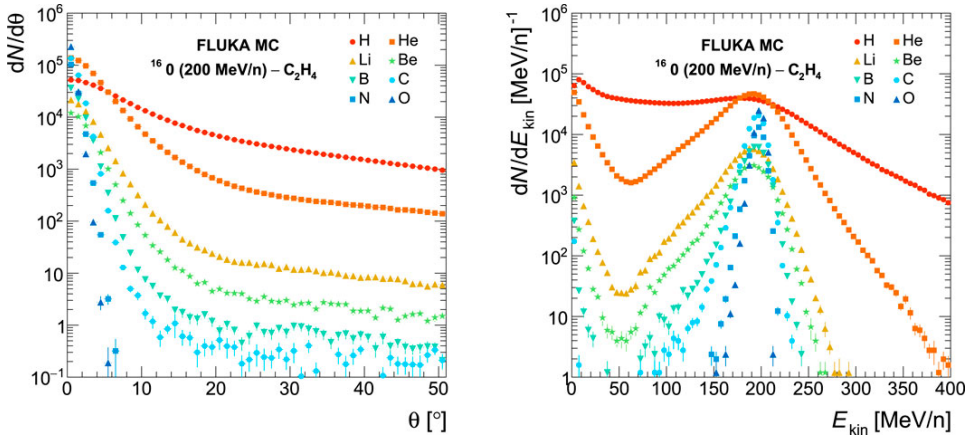

Figure 3.1: In (a) the kinetic energy of nuclear fragments produced from a ^{16}O beam at 200 MeV/u interacting with a C_2H_4 target; in (b) their angular distribution. Both plots are obtained using FLUKA simulations [40].

The experiment uses beams of protons and other ions such as ^{4}He, ^{12}C, and ^{16}O against targets containing H, C, or O (graphite, polyethylene, and PMMA), simulating interactions that occur inside the human body.
Projectile fragmentation can be obtained from direct reactions. For target fragmentation, the FOOT experiment employs the *inverse kinematic approach*, since target fragments are nearly impossible to detect due to their very short travel distances.

3.1.1 Inverse kinematics and cross section

The *inverse kinematic approach* involves reversing the roles of the projectile and the target. Instead of firing a proton beam against a target resembling a human tissue, nuclei abundant in the human body, such as C or O, are fired as projectiles on a Hydrogen target (protons). In this second configuration, fragments produced can escape the target much more easily since they originate from nuclei not at rest. The cross section of the inverse process (proton-nucleus) can be determined using a proper Lorentz boost.
In particular, let's consider a beam moving along the z axis at velocity β in the laboratory frame S, against a target t (the human body in hadrontherapy). It is possible to describe the situation in the frame S' of the projectile p, where it is the target that moves toward p with velocity $-\beta$. The inverse kinematic approach considers the process $t \to p$ (in the S' frame) instead of $p \to t$ (in the S frame) and then use a Lorentz boost to go back to S. To apply this method the target in the S' frame must have the same β of the projectile in the S frame, which corresponds to the same energy per nucleon.
In the laboratory frame S, the projectile has a 4-momentum $\mathbf{P} = (E/c, p_x, p_y, p_z)$, while in the projectile frame S' the 4-momentum is $\mathbf{P'} = \left(E'/c, p'_x, p'_y, p'_z\right)$. The two vectors are related by:

$$\mathbf{P'} = \Lambda(\beta)\mathbf{P} \tag{3.1}$$

where $\Lambda(\beta)$ is a 4×4 matrix given by:

$$\Lambda(\beta) = \begin{pmatrix} \gamma & 0 & 0 & -\beta\gamma \\ 0 & 1 & 0 & 0 \\ 0 & 0 & 1 & 0 \\ -\beta\gamma & 0 & 0 & \gamma \end{pmatrix} \tag{3.2}$$

with $\gamma = \frac{1}{\sqrt{1-\beta^2}}$ being the Lorentz factor. The inverse transformation can be easily obtained by noting that $\mathbf{\Lambda}^{-1}(\beta) = \mathbf{\Lambda}(-\beta)$.
It is important to note that this method increases the uncertainty in the cross-section measurement, and for this reason, direct measurements require very high accuracy. In particular, to ensure the Lorentz transformation is precise, the emission angle of the fragments must be measured with an uncertainty no greater than 1 millirad [43].
Another issue is how to produce a Hydrogen target, as Hydrogen is gaseous at room temperature, making it impractical for the experiment due to its low interaction rates. Additionally, Hydrogen is highly flammable and poses safety risks, requiring modifications to the beam-target system of the experiment. To address this limitation, the FOOT experiment uses targets of graphite (C), polyethylene (C_2H_4) and PMMA ($C_5O_2H_8$) and then obtain the single elements cross sections via subtractions. For example, the cross section for Hydrogen is obtained through the subtraction of the C cross section from the polyethylene one:

$$\frac{d\sigma}{d\Omega}[\mathrm{H}] = \frac{1}{4}\left(\frac{d\sigma}{d\Omega}[\mathrm{C_2H_4}] - 2 \cdot \frac{d\sigma}{d\Omega}[\mathrm{C}]\right). \tag{3.3}$$

3.2 Electronic setup

The FOOT electronic setup is the one dedicated to fragments with Z $\leq$ 2 and it has an angular acceptance up to 10°. The setup is constructed to measure momentum (**p**), kinetic energy (E_{kin}), time-of-flight (TOF) and energy loss (ΔE) of the different fragments. In order to meet the requirements set on the cross section measurement, using Monte Carlo simulation, it has been determined the experimental resolution needed on these quantities, in particular:

- $\sigma(p)/p$ at level of 4-5%
- $\sigma(E_{kin})/E_{kin}$ at the level of 1-2%
- $\sigma(TOF)/TOF$ at level of 100 ps
- $\sigma(\Delta E)/\Delta E$ at level of 5%

Since the detector needs to be moved to different locations based on the availability of various ion beams, the detector design is flexible and compact, with a table-top concept. Additionally, to ensure accurate measurements, the detector contribution to fragmentation must also be kept as low as possible.
A schematic representation of the FOOT electronic setup is shown in Figure 3.2.

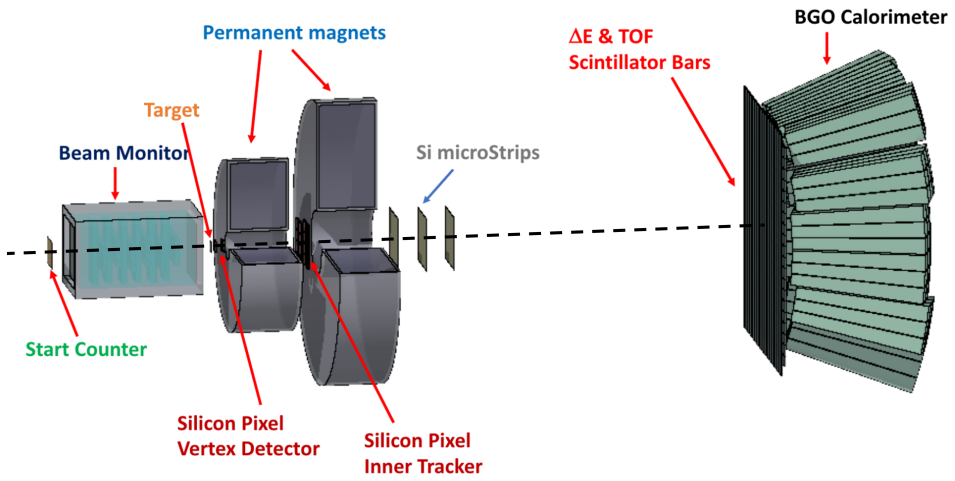

Figure 3.2: Schematic representation of the FOOT experiment [40].

The FOOT electronic setup can be divided into three different regions: an *upstream region*, before the target, a *tracking region* to track fragments' trajectories and a *downstream region* with a calorimeter for the energy measurement.

3.2.1 Upstream region

The *upstream region* is devoted to beam monitoring before it reaches the target, placed right after. It is composed of a plastic scintillator (*Start Counter*) and a drift chamber (*Beam Monitor*). To perform inverse kinematics, it is needed to have a complete knowledge of the beam, including β for the Lorentz boost, which depends on its energy and direction that needs to be precisely determined using the BM.

Start Counter

Positioned upstream of the Beam Monitor (BM) and the target, the *Start Counter* (SC) have several important functions: it provides the experiment's minimum bias trigger, monitors the incoming beam, gives the time reference for all detectors and the start time for the Time-Of-Flight (TOF) measurements.
The SC is composed of a thin EJ-228 plastic scintillator foil [44], which is 250 μm thick and has a $5 \times 5\,\mathrm{cm}^2$ active area, enough to cover the typical transverse size of the particle beam (see Figure 3.3a). The thickness has been chosen to minimize the interaction probability of primaries while maintaining good time resolution. The scintillator is supported by an aluminum frame and encased in a black 3D-printed box to ensure light-tight conditions. The scintillation light generated in the foil is detected by 48 silicon photomultipliers (SiPMs), each with an active area of $3 \times 3\,\mathrm{mm}^2$. The SiPMs are arranged around the scintillator, with 12 on each side, bundled in 8 electronics channels. Signal acquisition and SiPM power management are handled by the WaveDAQ system [45]. Waveforms collected by the SC are processed offline using a constant fraction discriminator technique to determine the event start time t_0. The SC achieves a time resolution of approximately 40-50 ps. [46].

Beam Monitor

The *Beam Monitor* (BM), initially developed for the FIRST experiment [47], is a drift chamber composed of 12 wire layers with 3 drift cells 16 mm$\times$ 11 mm per layer, allowing for beam profile reconstruction in both x and y directions (see Figure 3.3b). Consecutive layers are staggered by half a cell to resolve left-right ambiguities in track reconstruction. For the FOOT experiment, the BM operates at approximately 0.9 bar with an 80/20% Ar/CO_2 gas mixture and a working voltage between 1850 and 2200 V, depending on the ion beam. The BM achieves an efficiency of around 90% and can reach a spatial resolution better than 100 μm in the central region of the BM [48]. The BM is placed between the SC and the target and it measures the primary beam direction and impact point on the target. Its role is fundamental for resolving pile-up ambiguities in tracking detectors: for this reason it is needed high precision alignment between the BM and downstream detectors to ensure accurate direction measurement of fragments relative to

the beam. Additionally it is used to reject events where the beam has fragmented before the target, for example in the SC.

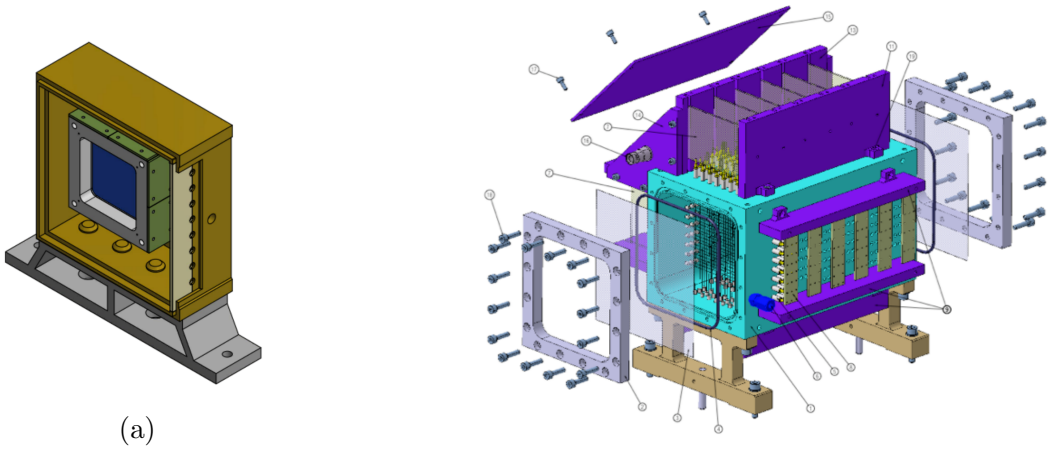

(a) (b)

Figure 3.3: In Figure 3.3a the start counter, in Figure 3.3b the beam monitor [40].

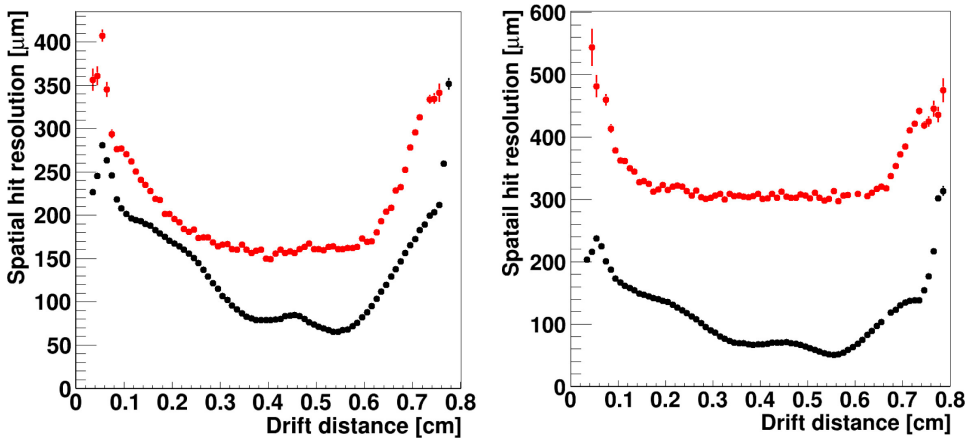

Figure 3.4: Resolution of the BM calculated with two different methods (see [49]) for proton beams at 228 MeV (left) and 80 MeV.

3.2.2 Tracking system

The FOOT *tracking system* is placed after the target and is composed by a magnetic spectrometer: two permanent magnets, a *vertex detector* (VTX), an *innner tracker* (IT) and a *microstrip detector*(MSD) (in Figure 3.6). The tracking system aims to reconstruct the track of the fragments.

Vertex detector

The VTX is composed of 4 different pixel sensor layers of dimensions 2 $\times$2 cm with a geometrical acceptance of about 40° for emitted fragments. The detector employs MIMOSA-28 (M28) Monolithic Active Pixel Sensors (MAPS) (see Figure 3.5). Each M28 sensor features a matrix of 928 $\times$ 960 pixels with a 20.7 µm pitch. The sensors are 50 µm thin. The VTX's high spatial resolution of 5 µm [50], combined with data from the Beam Monitor (BM), allows for precise angular tracking of particles with an accuracy at the mrad level while minimizing the impact of multiple scattering.

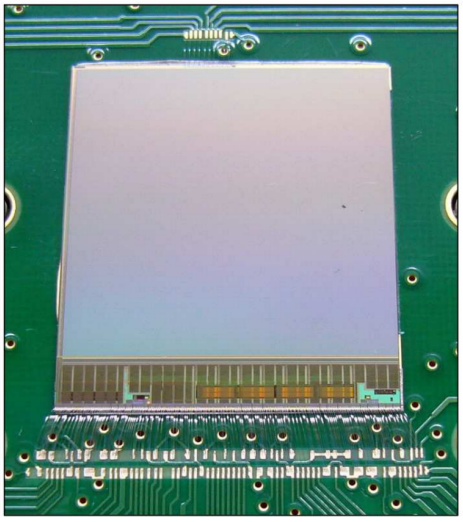

Figure 3.5: Picture of a M28 sensor [43].

Inner Tracker

The IT is placed between the two permanent magnets and includes two planes of pixel sensors to track fragments within the magnetic field region. Each plane has a sensitive area of approximately $8 \times 8\,\mathrm{cm}^2$ and is equipped with 16 M28 sensors per layer. It uses the same technology of the VTX, making the DAQ system architecture simpler. The IT sensors are arranged in ladders made of two modules of four M28 sensors glued on either side of a support structure of silicon carbide (SiC) 2 mm thick.

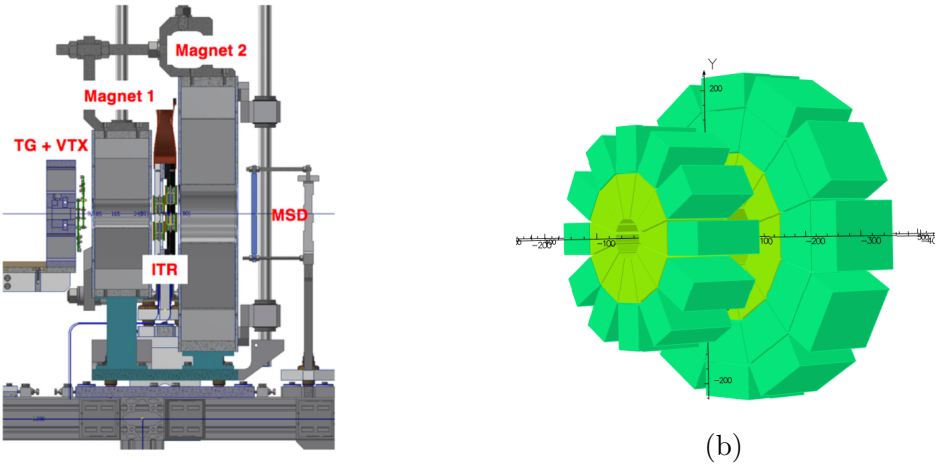

(a) (b)

Figure 3.6: In Figure 3.6a the technical design of the tracking region: the beam is coming from the left [40]; in Figure 3.6b a representation of the two magnets in Halbach configuration.

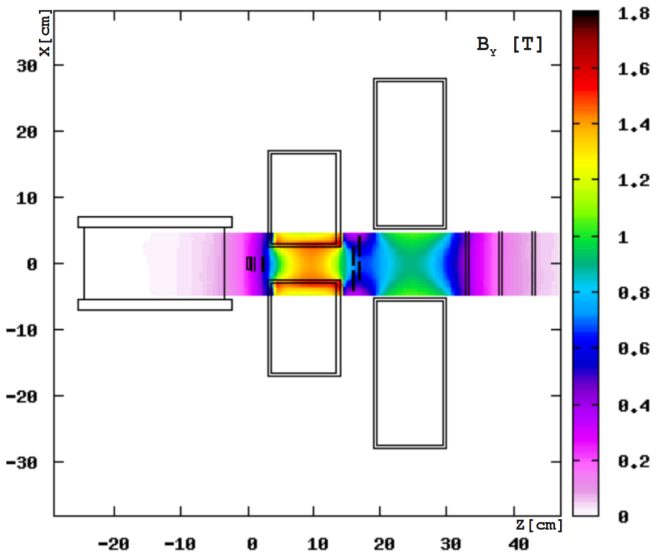

Figure 3.7: Magnetic field map produced by the FOOT magnets. The target is at z = 0.

Magnetic System

The FOOT spectrometer's magnetic system is used to bend the produced fragments, in order to reconstruct their momentum. The momentum resolution must be as precise as possible. Considering that the experiment must be transportable, the magnetic

system uses two compact permanent magnets arranged in a Halbach configuration. This configuration creates a nearly dipolar magnetic field inside a cylindrical permanent magnet.
The system includes two magnets (Figure 3.6b) with different dimensions: one with a 5 cm gap diameter providing up to 1.4 T, and another with a 10.6 cm gap diameter providing up to 0.9 T. The inner tracker between the magnets experiences an approximate field of 0.6 T (see in Figure 3.7 the magnetic field map).

Micro Strip Detector

The tracking of fragments downstream the magnetic region is essential for momentum measurement and aligning reconstructed tracks with hits in the Time-Of-Flight (TW) detector and the calorimeter. This task is handled by the MSD, which offers also a redundant measurement of energy loss per unit length (dE/dx) for fragments charge Z identification, complementing the TW measurements.
The MSD comprises three x-y tracking planes with an active area of 9.6 × 9.3 cm^2, separated by 2 cm along the beam direction, positioned immediately after the second magnet. Each plane is made of two perpendicular Single-Sided Silicon Detectors (SSSDs), each thinned to 150 µm (for a total of 900 μm), attached to a hybrid Printed Circuit Board (PCB) for support and readout interfacing.
The strip pitch is of 50 μm, minimizing fragment pile-up, and the digital readout with a 150 μm. In beam tests with proton, ^{12}C and ^{16}O beams have shown that the spatial resolution of the MSD ranges from 10 to 35 μm [51]. In Figure 3.8 the spatial resolution of the MSD for different particles at different energies.

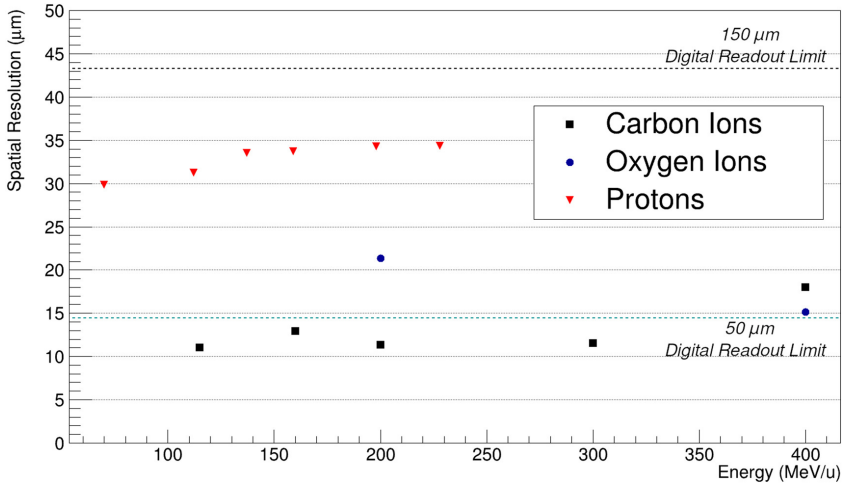

Figure 3.8: Spatial resolution computed from data taken with different particles at several energies [51].

3.2.3 Downstream region

The *downstream region* is the last part of the setup. It is placed at 1-2 m from the target and it is composed of two layers of scintillator bars, the TOF Wall (TW) and a BGO calorimeter (CALO).

TOF Wall

The TOF-Wall (TW) detector consists of two orthogonal layers of 20 plastic scintillator bars (EJ-200 by Eljen Technology), each 0.3 cm thick, 2 cm wide, and 44 cm long, forming a 40 $\times$ 40 cm active area. The TW measures energy deposition (ΔE), time-of-flight (TOF) using the t_0 from the Start Counter (SC), and hit position. These information are used then to identify the charge (Z) of incoming ions, which is fundamental for determining fragment mass, and also help to reconstruct fragments tracks. The chosen bar dimensions ensure minimal pile-up (below 1%) and optimize timing and energy resolution while reducing secondary fragmentation.The overall TW dimension matches the angular aperture of heavier fragments at the distance of 1-2 m from their production in the target.
Each bar is read out by 4 SiPMs per end, with a $3 \times 3\,\mathrm{mm}^2$ active area and 25 μm microcell pitch and the signals are digitized by the WaveDAQ system. This detector meets the FOOT experiment's requirements of TOF resolution below 100 ps and energy loss resolution $\approx 5\%$ for heavier fragments [52]. Additionally, it provides a dynamic range that spans over two orders of magnitude and allow the identification of fragments with varying energy releases, from protons to Oxygen. Using the TW time measurements, the position resolution can improve significantly until $\sigma_{\mathrm{pos}} < 8\,\mathrm{mm}$, optimizing the accuracy of offline fragment reconstruction. In Figure 3.9 two pictures of the TW during its assembly and on the beam line.

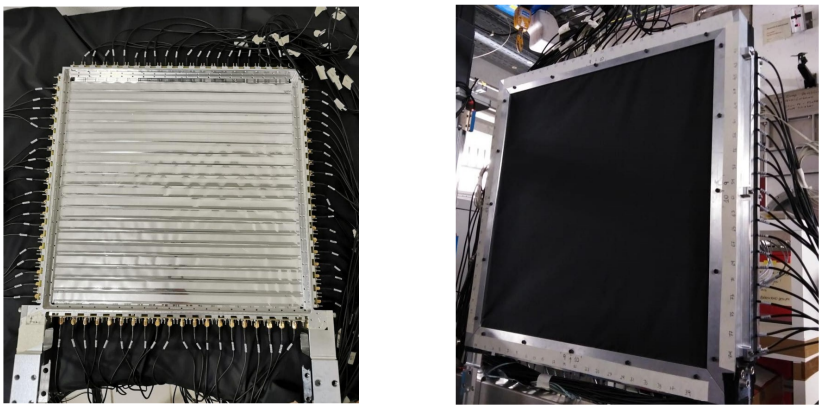

Figure 3.9: On the left a picture of ToF Wall detector during the assembly and on the right the TW on the beam line [53].

Calorimeter

The FOOT calorimeter is designed to measure the kinetic energy of fragments to determine their mass A. Depending on the energy of the primary beam, fragments can have different energies and lead to different processes inside the calorimeter. At the energies of 700-800 MeV/u, relevant for space radiation protection studies, hadronic showers can take place, and the full containment can not be achieved leading to reduced resolution. At lower energies, electromagnetic interactions dominate, allowing for better energy resolution that is needed for a precise description of the fragment energy. However, neutron production is unavoidable and these neutrons escape detection, causing energy leakage and systematic errors. For this reason the FOOT setup provides redundant measurements of different quantities.
The calorimeter uses 320 BGO ($Bi_4Ge_3O_{12}$) crystals arranged in a disk-like configuration ($\simeq$ 20 cm radius). The crystals, having high density ($\rho \approx 7.13\,\mathrm{g\,cm^{-3}}$) and good light yield (10 photons/keV), provide high stopping power and good energy resolution. Each crystal is shaped as a truncated pyramid with a front (back) area of $2 \times 2\,\mathrm{cm^2}$ ($3 \times 3\,\mathrm{cm^2}$) with a length of 24 cm and is coupled to a 25 SiPM matrix ($2 \times 2\,\mathrm{cm^2}$ active surface). Beam tests across a wide energy range have shown a good linear response and energy resolution $\sigma(E_{\mathrm{kin}})/E_{\mathrm{kin}}$ below 2%, meeting the experiment's requirements for heavier fragments [54][55].

3.2.4 Fragments identification process

In order to identify the fragments the FOOT electronic setup, uses all the different information coming from the detectors and combining them together. The charge of the fragments is obtained from the energy loss information coming from the TW, as well as a redundant measurement from the MSD, and the TOF measurement (time between the SC and the TW), using Eq. 1.2. The tracking system together with the magnetic field allows for the determination of the fragment rigidity (pc/Z) and its path length L. When combined with the measurements of TOF and charge Z, this provides both the momentum p and the velocity $\beta c = L/\mathrm{TOF}$ of the particle. The kinetic energy E_{kin} is measured in the calorimeter.
Using all these quantities, the mass of the fragments can be calculated with three different methods:

$$p = m\beta c\gamma \tag{3.4}$$

$$E_{kin} = mc^2(\gamma - 1) \tag{3.5}$$

$$E_{kin} = \sqrt{p^2c^2 + m^2c^4} - mc^2 \tag{3.6}$$

where γ is the Lorentz factor. In order to summarize the FOOT electronic experimental setup, Table 3.1 lists the detectors used, the measured quantities or functions they perform, and their respective resolutions.

Detector	Quantity Measured/Function	Resolution
Start counter	Trigger and TOF measurement	40-50 ps
Beam Monitor	Primary beam tracking	$100 - 300\,\mu$m
Vertex Detector and Inner Tracker	Fragments tracking	$5\,\mu$m
Micro Strip Detector	Fragments tracking	$35\,\mu$m
TOF Wall	TOF measurement and dE/dx	< 100 ps for time and 5% for dE/dx
Calorimeter	E_{kin}	2%

Table 3.1: Table summarizing the detectors used in the FOOT experiment, along with their respective functions, measured quantities, and resolutions.

3.3 Emulsion spectrometer

Light fragments (Z<3) tend to have a relatively high emission angle, making the experimental apparatus designed for heavier particles not suitable in this case. Therefore, the FOOT experiment is equipped with a dedicated setup specifically for detecting lighter fragments. The setup for light fragments consists of a Start Counter and a Beam Monitor, as described in Section 3.2.1, along with an Emulsion Cloud Chamber (ECC) that replaces all other elements present in the setup for heavy fragments.
The choice to use an emulsion chamber for fragment identification is due to the high emission angle of light fragments. Covering similar angles with a calorimeter would require it to be several meters in size, making its construction challenging both in terms of cost and portability.
The ECC is composed of layers of graphite and polyethylene, which replace the target, alternated with plates coated with silver bromide (AgBr) emulsion films. When fragments pass through these films, they ionize the emulsion, creating silver atoms. After accumulating a certain number of tracks, the films are automatically scanned using an optical microscope and areas where silver has concentrated are observed, enabling reconstruction of the fragment tracks.
The subsequent region is dedicated to the identification of the charge of the produced fragments, while the final region, which also includes layers of lead, is used to measure the momentum.
The description provided here is non-exhaustive, as the ECCs are not employed in the present thesis work. A more comprehensive description is available in [40] and [56].

Chapter 4

GSI 2021 data analysis

In this thesis work, I analyzed data taken in July 2021 at the GSI (Gesellschaft für Schwerionenforschung, Society for Heavy Ion Research) in Darmstadt, Germany.
At the time, the FOOT setup was not in its final configuration; the setup used in that data acquisition is presented in Section 4.1 . The data were acquired using a beam of ^{16}O at 200 MeV/u and 400 MeV/u with a 5 mm graphite (C) target and a 5 mm and 10 mm polyethylene (C_2H_4) target. The analysis is focused on the data at 400 MeV/u with the 10 mm polyethylene target, obtaining the total and angular differential elemental cross section. Starting from a previous analysis performed on the C target, I also extracted the proton cross section via subtraction (as explained in Section 3.1.1).

4.1 GSI 2021 setup

The FOOT setup in July 2021 at GSI was composed of the Start Counter (SC), the Beam Monitor (BM), the target and the ToF Wall (TW). Part of the tracking system was also present, with the Vertex Detector (VTX) and the Micro Strip Detector (MSD), as well as a part of the calorimeter (CALO), namely one module composed of 9 crystals. The magnets and the Inner Tracker (IT) were completely absent. Even if present, the VTX and the MSD were still not calibrated and aligned yet, thus no information from the tracking system was used for this analysis.
The detectors I use in the analysis are then the SC, the BM and, at ~ 1.93 m from the target, the TW (see Section 3.2). Without tracking information, it is still possible to obtain the charge of the fragments, but not their mass, therefore the evaluation of the isotopic cross section is not achievable.
Possible out-of-target fragmentation cannot be removed actively, so its contribution is evaluated using runs without the target. In Figure 4.1 the schematic of the setup used in the GSI data acquisition is shown.

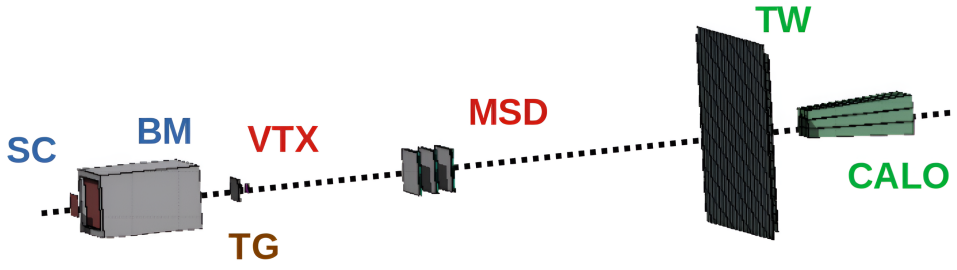

Figure 4.1: Schematic of the setup used in the GSI 2021 data acquisition. The VTX, MSD and module of the CALO were also present, even if they are not used in the analysis.

4.2 Software

In this analysis I worked on data acquired in July 2021 at GSI with the setup described in Section 4.1, as well as with some Monte Carlo (MC) simulation samples.
The initial step of the event reconstruction for both MC and real data is performed by the analysis software SHOE (Software for Hadrontherapy Optimization Experiment). This software is developed by the FOOT collaboration and stored in the INFN git repository [57]. It is a C++ object-oriented software built upon the ROOT framework [58].
SHOE is used to reconstruct information from the different subdetectors. For example, it performs signal processing for the SC and TW and the clusterization of the TW to obtain the charge identification. A more detailed description of the charge identification algorithm can be found in Section 4.2.2, since the charge information is used in this analysis.
The output of SHOE is a ROOT file containing all the information relative to the event reconstruction. Additionally, the software uses different configuration files tailored for each data acquisition campaign in order to ensure correct calibration and parameter settings.

4.2.1 MC sample

Monte Carlo simulations were developed to model a 400 MeV/u ^{16}O beam interacting with a polyethylene target, alongside a corresponding simulation without the target.
The simulation was developed using the Monte Carlo framework FLUKA [41][42]. It contains a complete description of the geometry and materials of every detector present in the setup to reproduce the real beam behavior. The MC simulates the interactions of the primary beam with the target and the setup itself, reproducing secondary particle production. It also records all the energy losses, the charge and mass of the produced fragments, as well as the kinematic quantities of all particles. The results are saved in

a ROOT file. The simulated MC data can then undergo event reconstruction through SHOE.
The agreement between data and MC simulation needs to be as accurate as possible, particularly for the TW detector, since it is fundamental for reconstructing the fragments' charge. To achieve results compatible with the real TW detector, the simulation mimics the energy response of the detector through calibration, and Gaussian smearing is applied to the energy loss and time-of-flight values computed with FLUKA (the two quantities measured by the TW). The possibility of more than one particle hitting a single bar is also accounted for, so multiple hits in a single bar are reconstructed as a single hit.
The Monte Carlo (MC) simulation is employed to validate the analysis technique by comparing the cross section derived from the MC truth, based on the actual yields of fragments, with the cross section calculated from the reconstructed fragments, as if they were real data. From the MC simulation all the relevant information can be evaluated, such as the geometrical efficiency, the efficiency of the TW algorithm used for reconstruction and clusterization, and the charge identification capability.

4.2.2 Charge identification

The charge identification algorithm employs data information from the SC and the TW detectors. The algorithm has been developed in order to provide the Z of each fragment on an event by event basis, also to be used as a seed for the tracking in the complete FOOT setup. The charge of each fragment is determined making use of the relation between the time-of-flight (TOF) and the energy loss (ΔE), as described by the Bethe Bloch formula (see Eq. 1.2). Generally, the energy release is expressed in function of β but, knowing the distance traveled by the fragments, the formula can be easily parametrized in function of the TOF. The charge identification is performed by selecting the charge based on a plot relating the energy loss of the fragments to their TOF. For each charge Z, the corresponding Bethe-Bloch curve as a function of TOF is calculated. The charge of each hit in a TW layer is assigned by selecting the closest Bethe-Bloch curve. This algorithm operates separately for each TW layer. A clustering algorithm groups hits from the two different TW layers and, if the charge identified in one layer matches the charge in the other, the hit is considered valid and is associated with the fragment.
In Figure 4.2 the energy loss in a single TW layer as a function of the TOF is shown for data taken with a 400 MeV/u ^{16}O beam on the polyethylene target. Each spot represents a different fragment charge. Since all fragments originate from the same projectile, the distribution of their kinetic energy peaks around the the projectile's energy, leading to a narrow TOF distribution. However, the energy loss, which depends on their different mass and charge, is pretty different, making each charge clearly distinguishable.

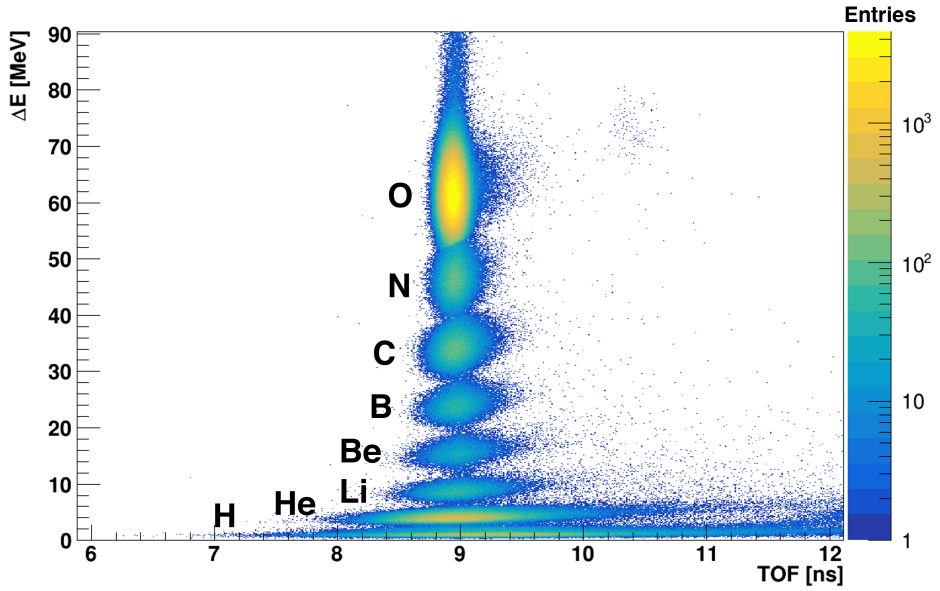

Figure 4.2: Energy loss in a single TW layer in function of the time-of-flight of real data of ^{16}O beam at 400 MeV/u against the polyethylene targe. The separation of each fragment, due to their different energy release, is clearly visible.

4.3 GSI 2021 data

The beam consisted of 400 MeV/u ^{16}O ions impinging on a 1 cm thick polyethylene (C_2H_4) target. A run without the target was also considered in order to perform background subtraction (see Section 4.4.2).
The FOOT experiment employs two different trigger settings: the minimum bias trigger and the fragmentation trigger. The minimum bias trigger (MB) records an event every time a primary ion passes through the start counter, regardless of whether a nuclear interaction occurred or not. The fragmentation trigger (FRAG), instead, is designed to acquire data only when the primary beam undergoes fragmentation, using information provided by the TW. The energy loss of primary ions is significantly larger than that of any fragments due to the difference in charge. Therefore, if the two central bars of the two different TW layers are hit simultaneously and the energy release exceeds a certain threshold, properly tuned to the expected energy loss of primaries, the event is tagged as Oxygen and discarded. The energy threshold is a trade-off between efficiently rejecting Oxygen events and retaining most Nitrogen fragments, which could be affected by a too low threshold. In MB runs, the trigger status information is recorded, allowing verification of whether the fragmentation trigger would have fired for each event.
The fragmentation trigger efficiently selects fragmentation events, as shown in Figure 4.3.

The plot represents the energy loss of different fragments in the TW for a MB run: the events in which the fragmentation trigger would have fired are shown in red, while all events are shown in black. The last peak represents the energy loss of the primary ions, and it is clearly reduced with the fragmentation trigger, while the number of produced fragments remains unchanged.

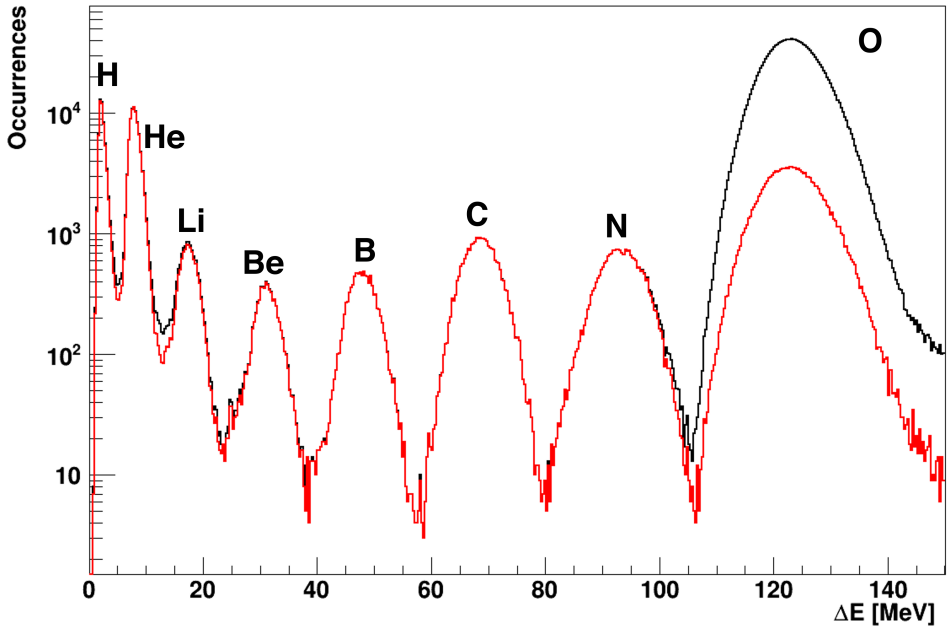

Figure 4.3: Energy loss in both TW layers for different fragments in a MB run: in red only the events in which the fragmentation trigger would have fired are selected. The fragmentation trigger efficiently reduces the number of primaries, while keeping all the fragments produced.

Run	Trigger	Target	Events
4288	MB	C_2H_4	455130
4289	MB	C_2H_4	581781
4290	MB	C_2H_4	526119
4291	MB	C_2H_4	174168
4292	MB	C_2H_4	173558
4298	MB	C_2H_4	572763
4299	MB	C_2H_4	186770

Run	Trigger	Target	Events
4302	MB	C_2H_4	594181
4303	MB + FRAG	C_2H_4	501962
4304	MB + FRAG	C_2H_4	502840
4311	MB + FRAG	C_2H_4	498541
4312	MB + FRAG	C_2H_4	503358
4313	MB	no	57133

Table 4.1: Physics run list.

In Table 4.1 all the physics runs analyzed in this work are listed, together with the type of trigger used and the number of events. In runs with the FRAG trigger, the MB trigger could also fire. However, only 1 out of 10 MB events was actually acquired. Considering the higher trigger rate of the MB trigger with respect to FRAG trigger, in these mixed runs the number MB and FRAG events are almost the same. For this reason, these are treated separately as independent measurements.

4.4 Analysis method

The aim of this analysis is to extract the total and angular differential cross sections of different fragments produced. With the available setup, it was not possible to extract the mass of each fragment, but only their charge, as described in Section 4.2.2. For this reason, the cross sections obtained refer to different fragment charges.
In this analysis, Hydrogen fragments are not considered, since the TW thresholds were optimized for higher charge fragments, resulting in low efficiency for Hydrogen.
The reaction of interest is the nuclear fragmentation of the primary beam inside the polyethylene target; however, fragmentation events can also occur outside the target, for example, in the material on the beam line or in air. The complete FOOT setup, with the tracking system, can recognize the background and eliminate it event by event. Using only SC, BM, and TW information, as in the case of the GSI 2021 setup, it is not possible to recover the origin of a fragment. For this reason, a run without the target was performed in order to subtract the out-of-target contributions (see Section 4.4.2). A simulation without the target has also been used in the MC analysis. The same analysis carried out on the data was also applied to the MC sample in order to validate the analysis method employed, as described in Section 4.4.6.
To reconstruct the angular distribution of the fragments, the track information from the BM of the primary ion for each event is used to extract the impact point on the target. Then, the impact point of the fragment on the TW is determined, and using this information along with the impact point of the primary beam on the target, the angle of the fragment's track is reconstructed. In Figure 4.4, the setup with the two reconstructed tracks is shown. The TW bars are 2 cm thick, and consequently, their granularity is $2 \times 2\,\mathrm{cm}^2$. The angle reconstruction is therefore affected by this limited precision, particularly altering the results for fragments with higher charge (Z = 6 and Z = 7), for which the angular distribution is narrow. To overcome this issue, an angular unfolding method was implemented (see Section 4.4.5).

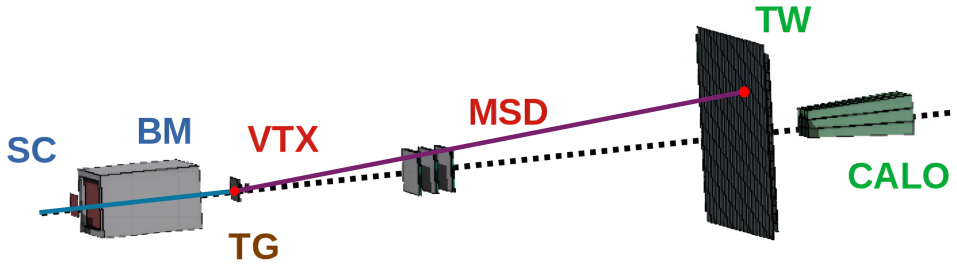

Figure 4.4: Schematic representation of the GSI 2021 setup, with the track of the primary Oxygen reconstructed by the beam monitor (blue) and the reconstructed track of a fragment (violet).

4.4.1 Cross section

The cross section extraction is performed through the measurement of the yields of different fragment charges. In particular, the elemental integral cross section for each charge can be defined using the following formula:

$$\sigma(Z) = \int_{\beta_{min}}^{\beta_{max}} \int_{0}^{\theta_{max}} \left(\frac{\partial^2 \sigma}{\partial\theta\partial\beta} \right) d\theta d\beta = \frac{Y(Z)}{N_{prim} \cdot N_{TG} \cdot \epsilon(Z)} \tag{4.1}$$

where θ_{max} is the angular acceptance of the setup, determined by the TW dimensions and the values β_{min} and β_{max} are the minimum and maximum values of β, corresponding to a specific time-of-flight range in which the charge reconstruction algorithm works properly. The maximum angle θ_{max} is of 5.7 ° and the values of β_{min} and β_{max} considered are 0.3 and 0.9, respectively. $Y(Z)$ is the number of fragments of a given charge measured by the TW, N_{prim} is the number of primaries (Oxygen) impinging on the target, N_{TG} is the number of interacting centers in the target per unit surface and $\epsilon(Z)$ is the efficiency for a specific charge Z. The number of interacting centers per unit area can be obtained from

$$N_{TG} = \frac{\rho \Delta x N_A}{A} \tag{4.2}$$

where ρ is the mass density of the polyethylene target ($0.94\,\mathrm{g/cm^3}$), Δx is the thickness of the target (1 cm), N_A is the Avogadro number, and A is the mass number of polyethylene, which is equal to 28.0534.
From the integration in β of the total cross section, it can be obtained the formula used for the angular elemental cross section measurement as follows:

$$\frac{d\sigma}{d\Omega}(Z) = \frac{Y(Z,\theta)}{N_{prim} \cdot N_{TG} \cdot \epsilon(Z,\theta) \cdot \Delta\Omega} \tag{4.3}$$

In this case the $Y(Z,\theta)$ is the number of fragments measured by the TW and $\epsilon(Z,\theta)$ is the efficiency for a given charge, at a given angle θ. The angle θ, as described previously, is the one between the BM track and the reconstructed track of the fragment from the interaction point in the target to the interaction point in the TW. The efficiency has been calculated using the MC sample, as explained in Section 4.4.3. Given the distance of the TW from the target of $\approx 2\,\text{m}$ and the width of the TW bars of $2\,\text{cm}$, the minimum bin width is of $\approx 0.57°$. Heavier fragments have a narrower angular distribution, for this reason the number of bins is set differently for different fragments, to account for available statistic in background data.

4.4.2 Background subtraction

As already mentioned, the out-of-target fragmentation cannot be directly evaluated from the analysis. The fragments taken into account for the cross section evaluation are all those that reach the TW; thus, fragments produced in air or in the setup material are also considered.
The plot in Figure 4.5 shows the energy loss in the first TW layer for different fragments in runs with and without the target, after rescaling for the number of primaries. In the run without the target (in red), it is evident that the amount of out-of-target fragmentation is not negligible.

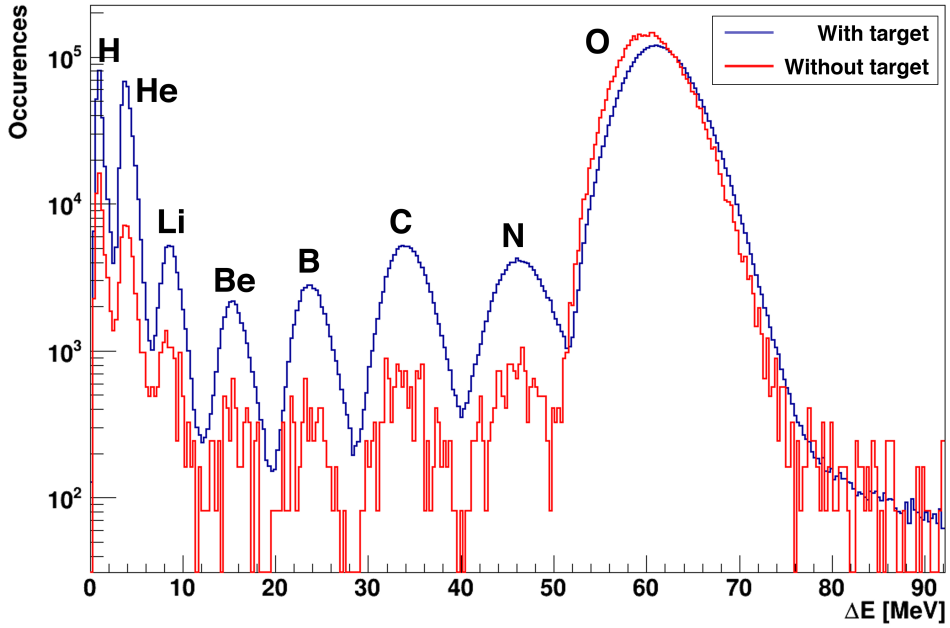

Figure 4.5: Energy loss in the front layer of the TW for all the runs with the target (in blue) and without it (in red).

To eliminate the contribution of out-of-target fragmentation, a run without the target is used to subtract the background. In particular, the number of fragments produced over the number of primaries (Y/N_{prim}), used to calculate the cross section in Eq. 4.1 and Eq. 4.3, becomes:

$$\frac{Y}{N_{prim}} = \frac{Y_{TG}}{N_{prim,TG}} - \frac{Y_{noTG}}{N_{prim,noTG}} \tag{4.4}$$

where Y_{TG} and Y_{noTG} are, respectively, the number of fragments in runs with and without the target, and $N_{prim,TG}$ and $N_{prim,noTG}$ are the corresponding number of primaries. The division by the number of primaries is important for correct subtraction, ensuring that the fragment yields are properly normalized, considering the different number of primaries.

4.4.3 Efficiency

The efficiencies in Eq. 4.1 and Eq. 4.3 are obtained using the MC sample information. The angular efficiency $\epsilon(Z, \theta)$ includes both the TW detector reconstruction efficiency and the geometrical efficiency. The reconstruction efficiency is computed dividing the number of fragments reconstructed by the TW with a certain charge Z and angle θ by the number of fragments with charge Z that reaches the TW within the angle θ. This represents the TW reconstruction capability accounting for the clustering algorithm performance.
The geometrical efficiency, instead, takes into account the fragments produced in the target, within the acceptance angle of the TW, that actually arrives in the TW and it is obtained taking the number of fragments generated in the target that reaches the TW with a certain Z and θ over the number of total fragments produced in the target with the same Z and θ. This efficiency takes into account for example light fragments, like He, that exit the angular acceptance due to Multiple Coulomb Scattering.
The final efficiency results from the multiplication of the two just described. The efficiencies are calculated using the true angle θ from the MC in order to avoid including angle mixing effects, described in more details in Section 4.4.5. The efficiency is applied both in reconstructed MC and data after background subtraction. In Figure 4.6 the angular efficiencies for each charge are represented in function of the emission angle. As previously stated, the binning is chosen to address the limited statistics in the background data for higher Z fragments at higher angles. For light fragments, the efficiency increases with the angle. This is related to the high multiplicity of events involving light fragments and the pile-up that can take place in the same bar. Heavier fragments have a more constant efficiency between 84% and 88%.
Similar calculations are used to obtain the efficiency for each different fragment charge $\epsilon(Z)$ and the result is shown in Figure 4.7. In this case the efficiencies range from a minimum of 68% for He up to 88%.

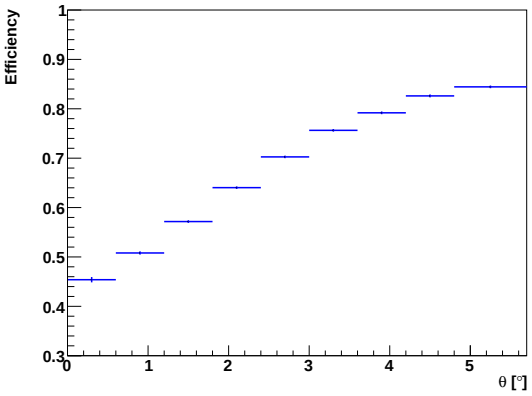

(a) Angular efficiency for Z = 2

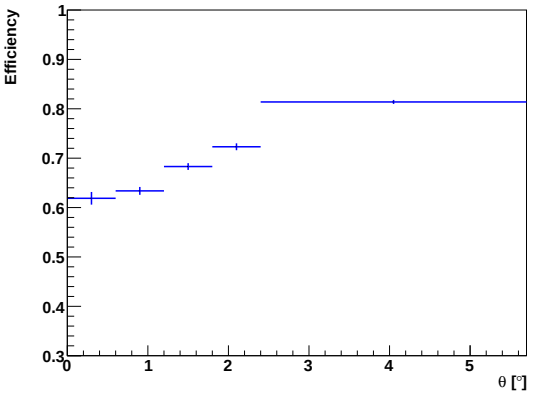

(b) Angular efficiency for Z = 3

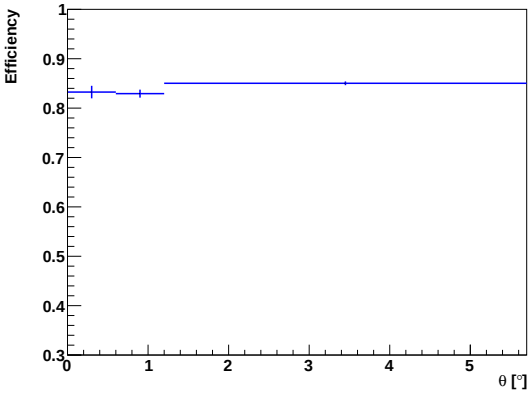

(c) Angular efficiency for Z = 4

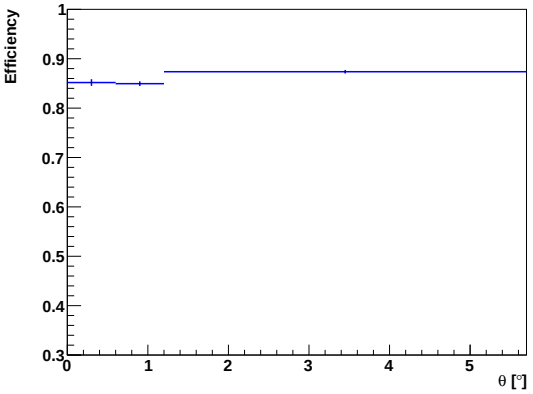

(d) Angular efficiency for Z = 5

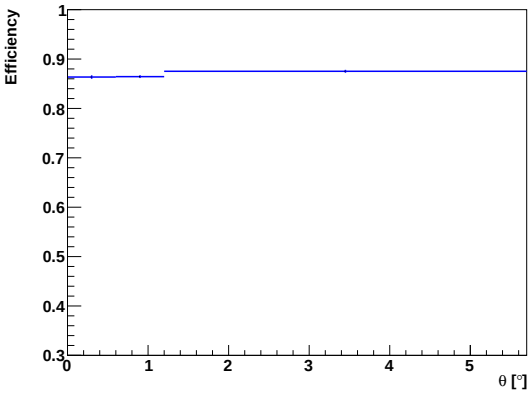

(e) Angular efficiency for Z = 6

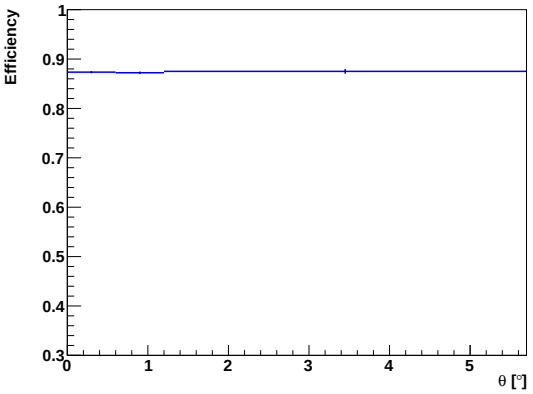

(f) Angular efficiency for Z = 7

Figure 4.6: Angular efficiencies in function of the emission angle for different charges.

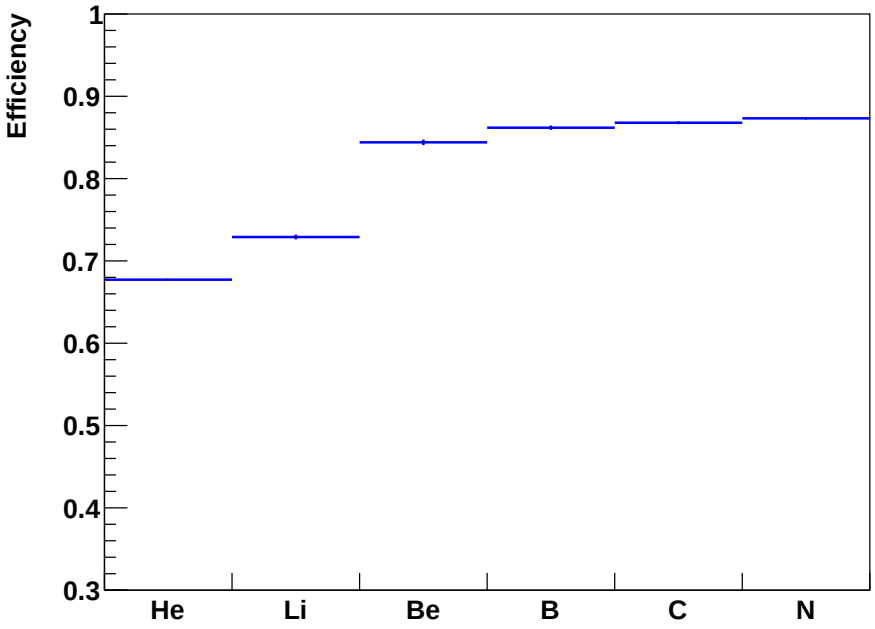

Figure 4.7: Efficiency for each fragment charge.

4.4.4 Purity

The MC sample has also been used to correct the possible wrong outputs of the charge reconstruction algorithm. In particular, after performing the charge reconstruction in the MC sample, as it is done on real data, a purity correction factor can be calculated for each charge and angle as:

$$P(Z_{reco}, \theta_{reco}) = \frac{N(Z_{reco} = Z_{true}, \theta_{reco})}{N(Z_{reco}, \theta_{reco})} \ . \tag{4.5}$$

The formula represents the number of correctly reconstructed charges over the number of fragments reconstructed with charge Z_{reco}.
The purity correction is then applied to the data, separately for with-target and without-target samples, before background subtraction. This procedure has shown, in various simulations, to yield better results in terms of cross-section.

4.4.5 Unfolding procedure

The lack of a tracking system in the GSI setup makes the reconstruction of the emission angle of the fragments more challenging. The angle is reconstructed using the information on the track of the primary beam from the BM and the reconstructed fragment track from the impact point in the TW (Figure 4.4). In Figure 4.8 the reconstructed angle in function of the true angle for the MC sample is shown for each different true charge. The angle mixing is indeed an issue and for Z = 6 and Z = 7, characterized by a particularly narrow angular distribution, this can lead to a wrong cross section evaluation.
The incorrect assignment of the reconstructed angle is due to the poor granularity of the TW, which hinders the correct reconstruction of the fragment trajectory after the target. The angle reconstructed using the true trajectory of the BM (in blue in Figure 4.4) and the reconstructed fragment track (the one that depends on the TW impact point, in violet in Figure 4.4) in function of the true angle is shown in Figure 4.9a. The angle reconstructed using the reconstructed BM trajectory and the true fragment track in function of the true angle is instead shown in Figure 4.9b. The reconstructed angle improves notably in the second case, highlighting the influence of the TW on the accuracy of the reconstruction. Another factor that influences angle reconstruction is the Multiple Coulomb Scattering of the fragments, that reaches the TW with a different angle with respect to the angle at their production.
This kind of angle mixing issue can be adjusted through an unfolding procedure, a method commonly employed in physics to correct for detector effects and resolution limitations [59]. In this analysis, the unfolding algorithm was applied to reconstruct the true fragments angular distribution. The unfolding was implemented using the Bayesian iterative algorithm [60][61] present in RooUnfold [62]. The information in the plots of Figure 4.8 are used to build a response matrix C_{ij} that expresses the effects of the experimental acceptance and resolution. Each element of this matrix represents the probability that an event generated in the i-th true bin (true angle) is reconstructed in the j-th measured bin (reconstructed angle). The Bayesian unfolding method starts with an initial prior, in this case the true angular distribution of different charges, and combines the measured data with the response matrix. Using Bayes' theorem, the posterior distribution calculated is compared with the prior. This process is repeated iteratively, with the posterior from one iteration used as the prior for the following. In this case, after an evaluation of different parameters, three iterations were performed.

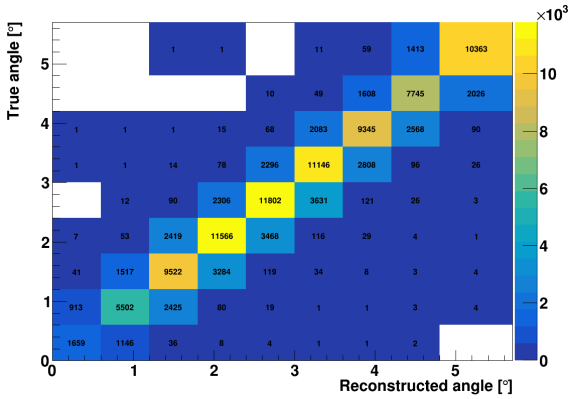

(a) Z = 2

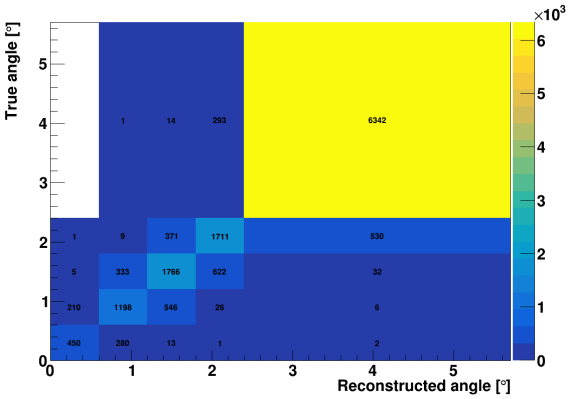

(b) Z = 3

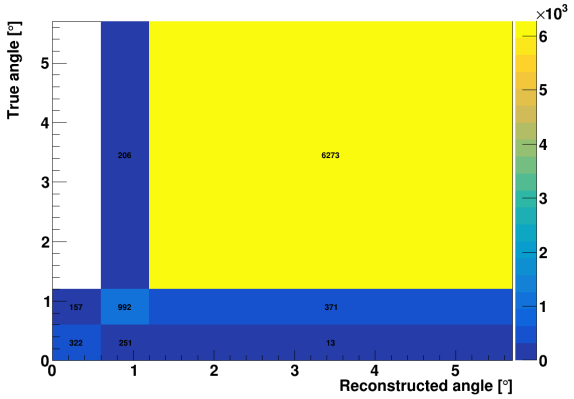

(c) Z = 4

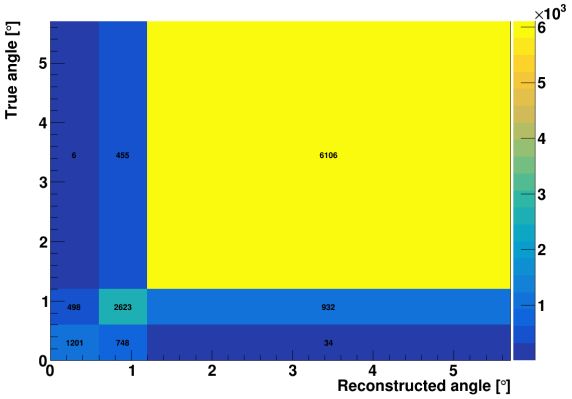

(d) Z = 5

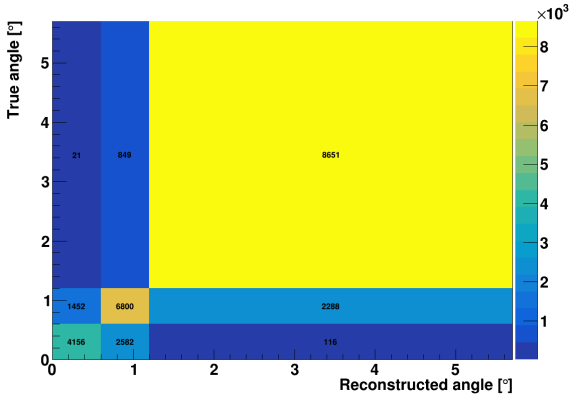

(e) Z = 6

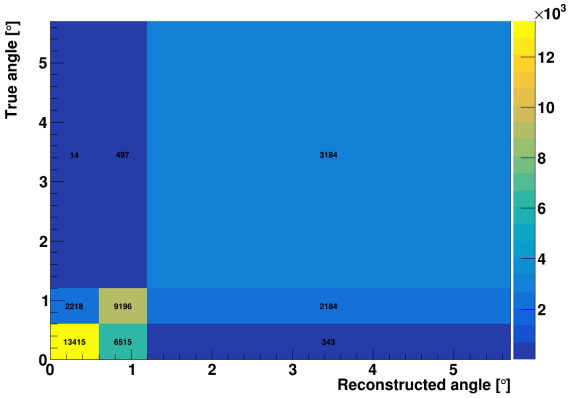

(f) Z = 7

Figure 4.8: True vs reconstructed angle for different charges for the MC sample.

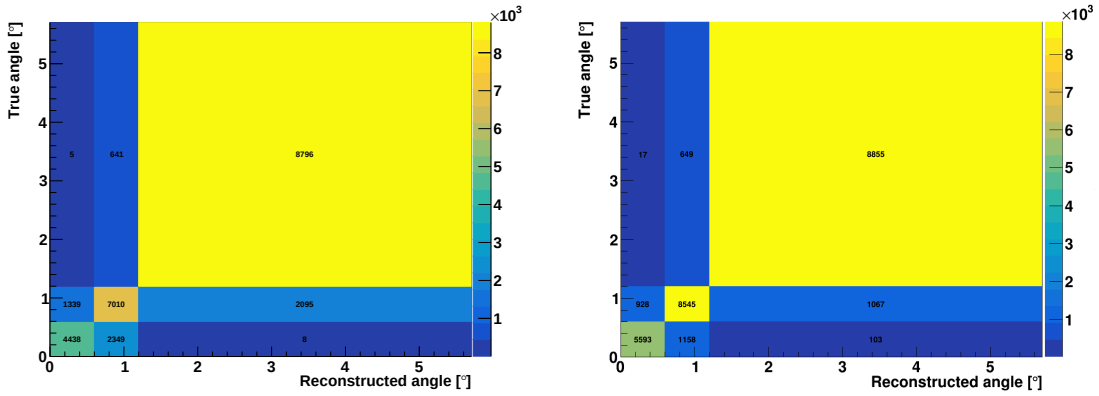

(a) (b)

Figure 4.9: For Z = 6: in Figure 4.9a the angle reconstructed using the true trajectory of the BM (in blue in Figure 4.4) and the reconstructed fragment track (in violet in Figure 4.4) vs the true angle; in Figure 4.9b the angle reconstructed using the reconstructed BM trajectory and the true fragment track vs the true angle.

4.4.6 Analysis method validation

The analysis method employed in this analysis, that includes background subtraction and unfolding procedure, has been validated using the MC sample. In particular this check is fundamental for angular cross section evaluation, for which the accuracy of the background subtraction technique is not straightforward.
For the method validation, the MC data are processed in the same way of data, using MC sample simulations with and without target and performing background subtraction along with efficiencies and purities. The reconstructed cross section obtained in this way is then compared with the cross section calculated using all true fragments yields retrieved directly from the MC itself.
The results obtained for angular cross section are presented in Figure 4.10: in black the true cross section extracted from the MC, in blue the reconstructed cross section before unfolding and in red the reconstructed cross section after unfolding procedure are reported. The cross section is expressed in barn/sr in function of the angle θ. The unfolding appears to be important for a more precise cross section result, particularly for higher Z fragments at higher angles, as already mentioned previously. The lower part of each plot shows the relative error in percentage of the true cross section (in gray) and the relative difference in percentage of the result with and without unfolding technique with respect the true value. The pre-unfolding results are already compatible with the true cross section within the error for some bins, showing that the analysis method employed is accurate. The post-unfolding result improves notably, making almost all values compatible within the error.

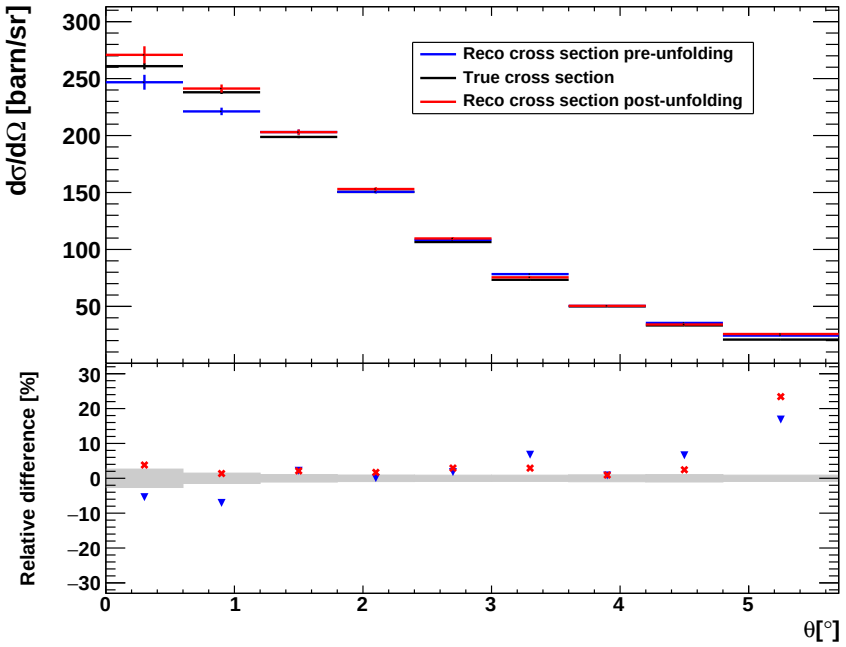
dσ/dΩ [barn/sr]
Reco cross section pre-unfolding
True cross section
Reco cross section post-unfolding
Relative difference [%]
θ[°]

(a) Z = 2

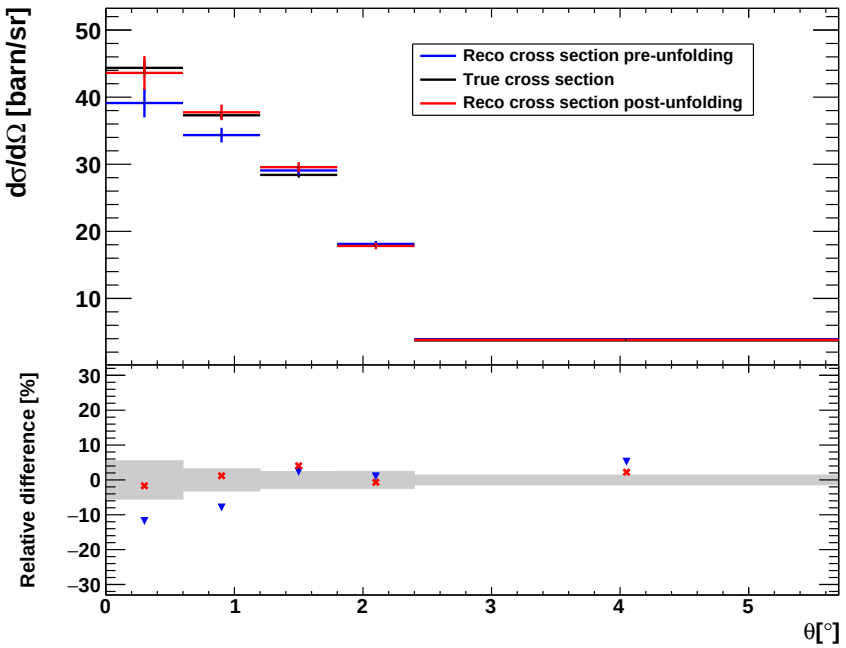
dσ/dΩ [barn/sr]
Reco cross section pre-unfolding
True cross section
Reco cross section post-unfolding
Relative difference [%]
θ[°]

(b) Z = 3

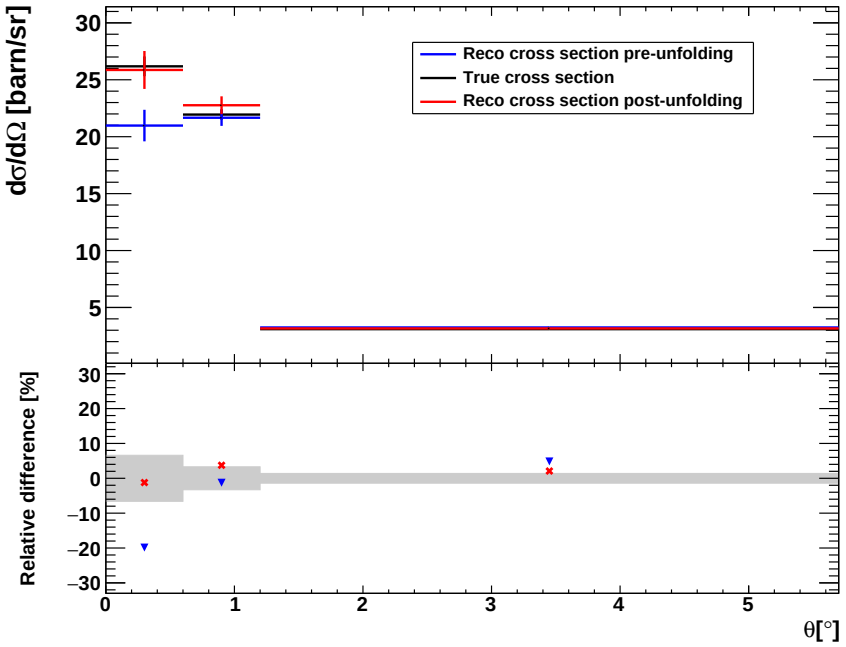
dσ/dΩ [barn/sr]
Reco cross section pre-unfolding
True cross section
Reco cross section post-unfolding
Relative difference [%]
θ[°]

(c) Z = 4

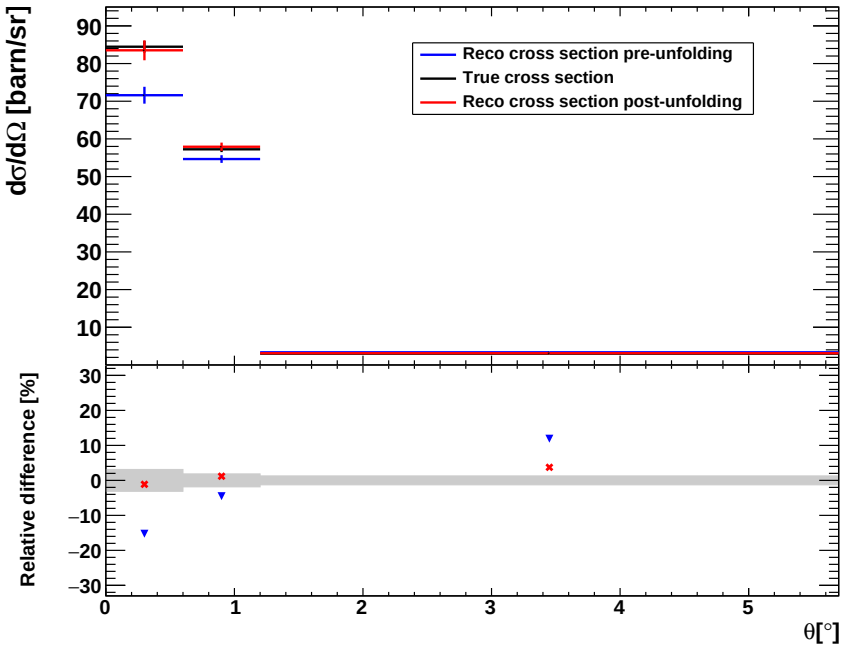
dσ/dΩ [barn/sr]
Reco cross section pre-unfolding
True cross section
Reco cross section post-unfolding
Relative difference [%]
θ[°]

(d) Z = 5

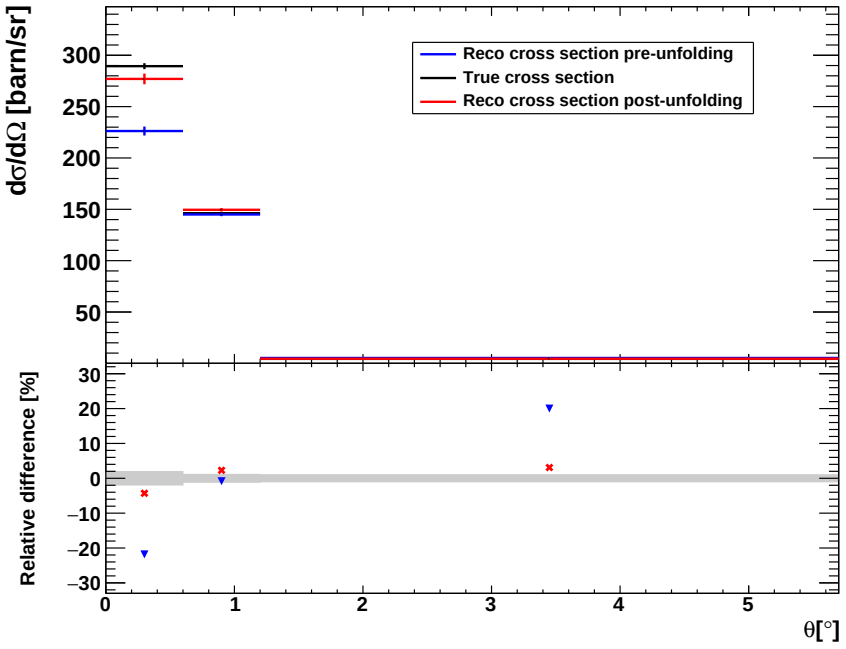

(e) Z = 6

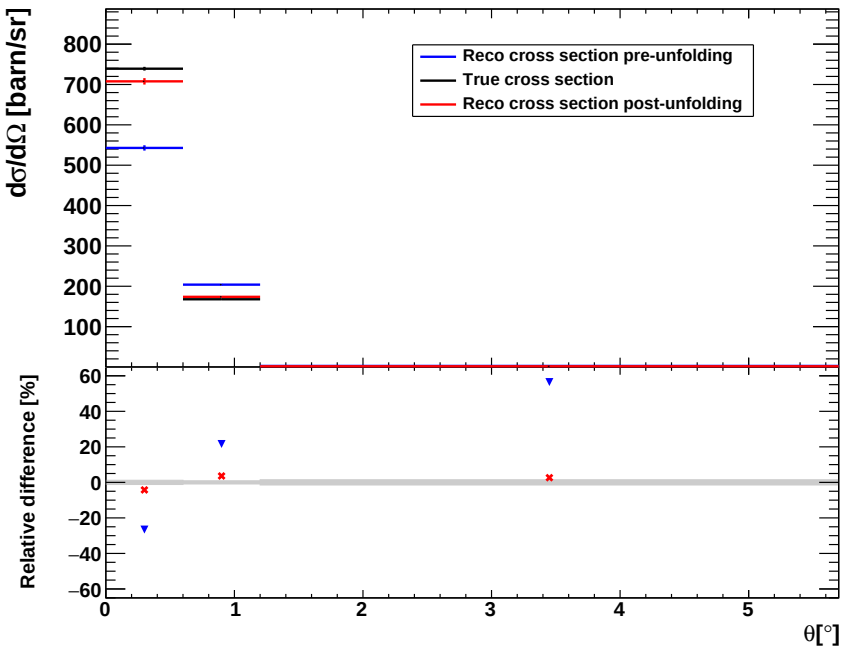

(f) Z = 7

Figure 4.10: Analysis method validation for different fragments.

The total cross section can be obtained in two different ways: using Eq. 4.1 with the total efficiency from Figure 4.7, or by integrating the angular cross section for each charge in the angular acceptance of the TW, from 0° to 5.7°. These two methods do not show significant differences, as illustrated in Figure 4.11, except for the He cross section. The plot shows in black the true cross section extracted from the MC, in red the one coming from the integration of the angular cross section of the MC sample and in blue the one calculated with Eq. 4.1, all expressed in mbarn. The discrepancy for He between these last two is due to the angular efficiency of He, which varies considerably across different angles. Therefore, the total cross section calculated by integrating the angular cross section provides a more accurate result, as it accounts for variations in reconstruction efficiency.

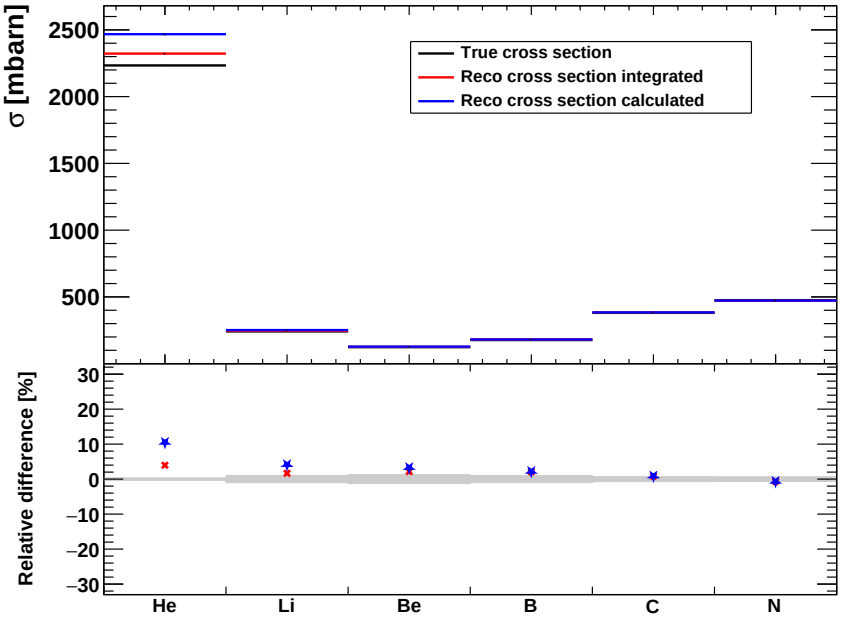

Figure 4.11: Total cross section for different charges for the MC sample. In black the true one from the MC, in red the one obtained from the integration and in blue the one calculated with Eq. 4.1. The relative error of the true cross section is shown in gray in the lower part of the plot; the red dots represents the relative difference between the true and the integrated cross sections, the blue ones the relative difference between the true and the calculated cross section.

4.5 Results

The data analyzed are all the physics runs listed in Table 4.1 acquired with a 400 MeV/u ^{16}O beam on a 1 cm polyethylene target.
In MB runs, the number of primary particles considered for the cross section evaluation corresponds to the number of events that have passed some quality cuts on the SC and BM. These cuts do not introduce biases in the measurement of the cross section since they are applied before the target, and thus the primary particles are selected before fragmentation occurs. In particular, pileup of multiple primaries are removed by looking at the raw SC signal and requiring only a single track in the BM. Additionally, events with a low energy deposition in the SC are eliminated, as these might correspond to fragmentations occurring before the target.
For FRAG events, the trigger selects only events in which fragmentation has occurred, so the number of primary particles needs to be evaluated. Since in MB runs it is possible to determine whether the FRAG trigger would have fired or not, by taking the ratio of the number of events labeled as fragmentation events to the total number of events, a trigger acceptance factor can be calculated, resulting to be approximately 18%. This factor is used to rescale the number of primary particles in fragmentation runs.
The total number of MB events is equal to 3511948 ± 1874 and for FRAG events is 735017 ± 857. The background events selected instead are only 52377 ± 229, since the run was acquired for alignment purposes. This small value of the background affects notably the error on the cross section measurement. All the MB statistics have been added together, as well as for FRAG statistics.
A data quality assessment has been done on both MB and FRAG data, without highlighting significant problems. The yields employed in the final result is a weighted average of the yields of MB and FRAG data.
In Figure 4.12 the results for the angular cross section for different fragments obtained using Eq. 4.3 are shown, where the fragments yields are the ones resulting after the unfolding procedure. The angular cross section is expressed in barn/sr and the binning is the one chosen to account for limited background statistics. Both statistical and systematic errors are shown and in the lower part of the plots the relative error in percentage is displayed. The main source of systematic uncertainty, represented in the plots, is related to the analysis procedure employed. It is derived calculating the relative difference between the reconstructed and true cross section of the MC sample, i.e. the difference in the cross sections in black and red of Figure 4.10. Except for few cases, this uncertainty results to be always smaller than the statistical one, below 10%, confirming the validity of the analysis method. The statistical error is mainly due to the limited statistics of the sample without target and ranges from 5% to 15 %, with a maximum of $\approx 28\%$ for the first bin of Li.

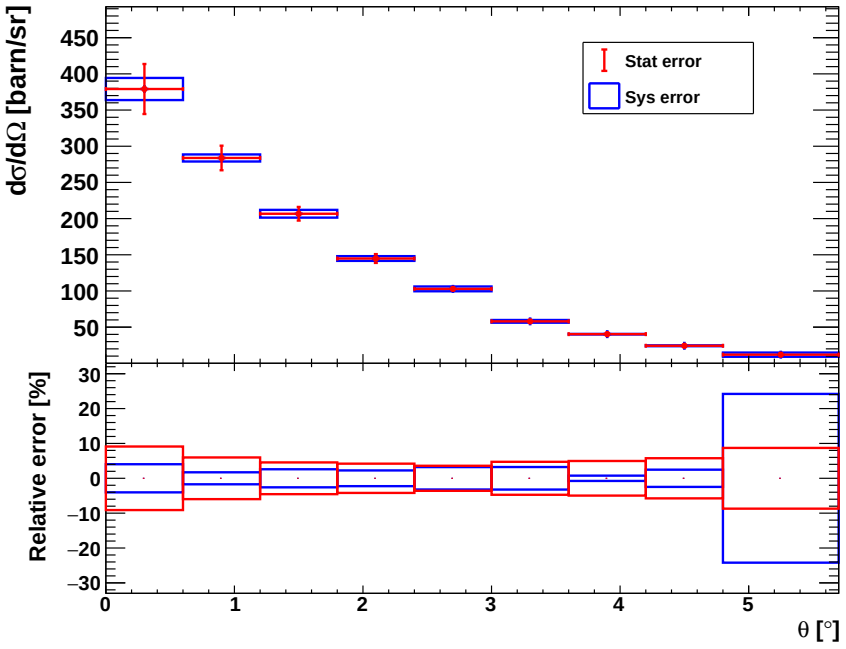
dσ/dΩ [barn/sr]
Stat error
Sys error
Relative error [%]
θ [°]

(a) Z = 2

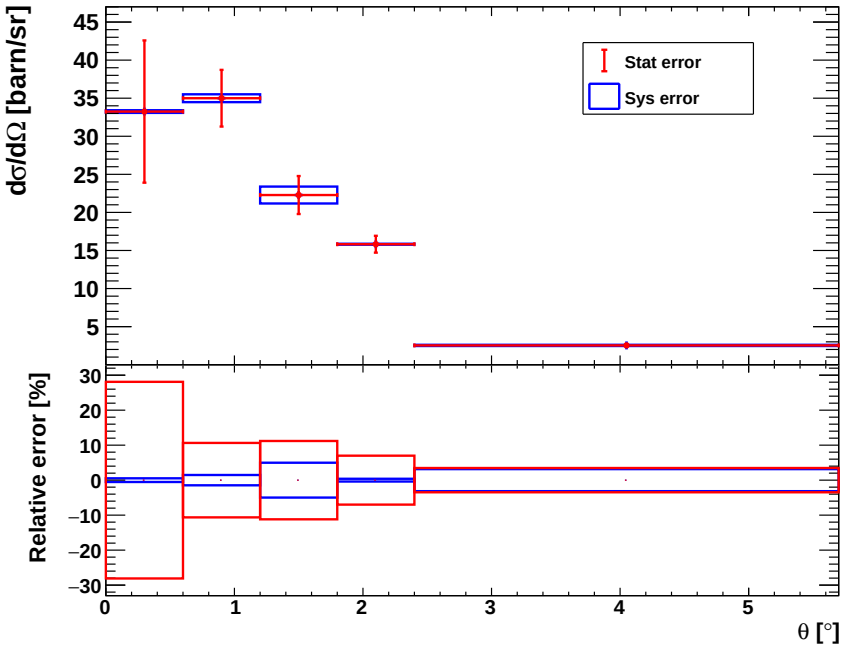
dσ/dΩ [barn/sr]
Stat error
Sys error
Relative error [%]
θ [°]

(b) Z = 3

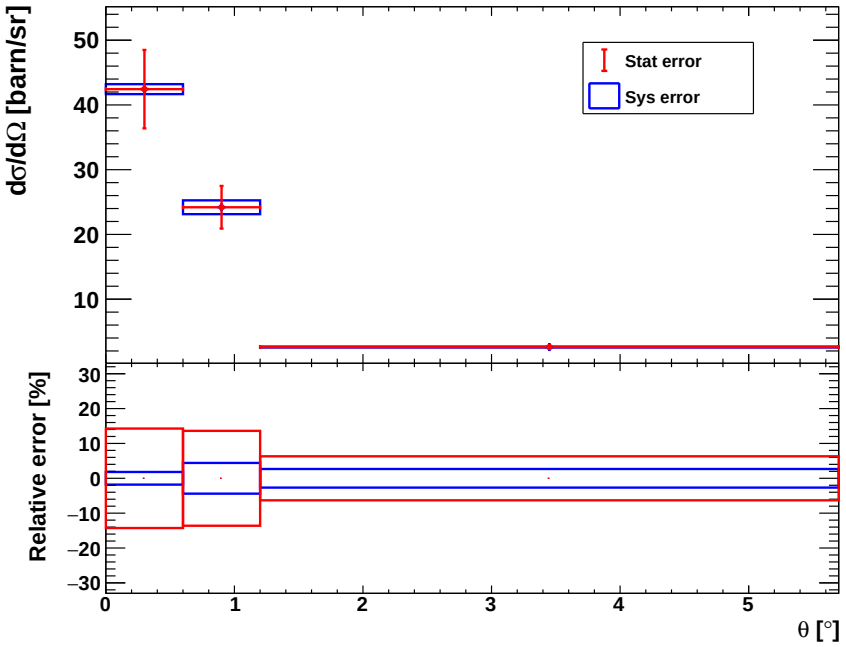
dσ/dΩ [barn/sr]
Stat error
Sys error
Relative error [%]
θ [°]

(c) Z = 4

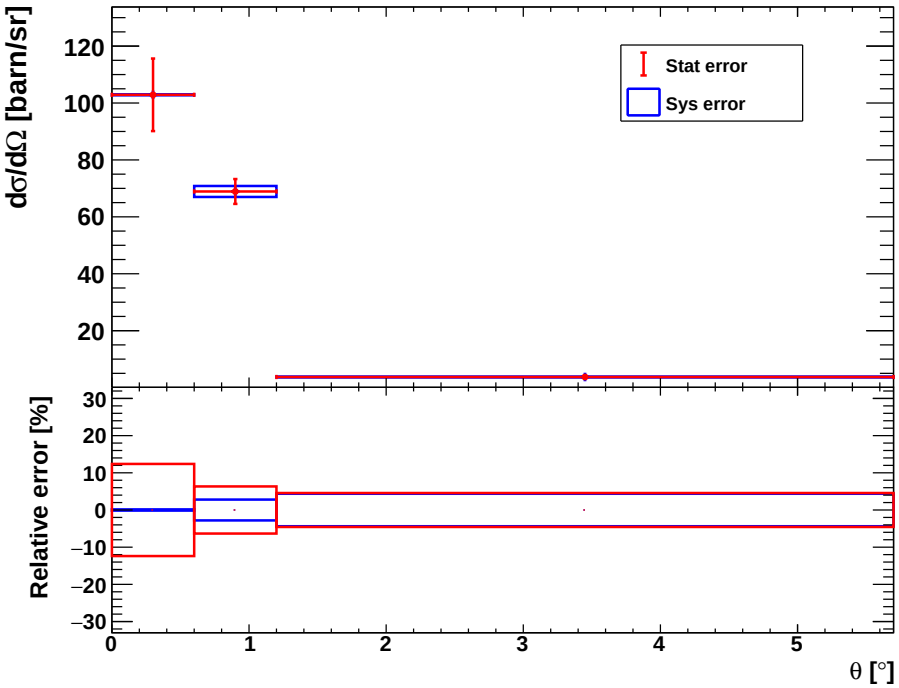
dσ/dΩ [barn/sr]
Stat error
Sys error
Relative error [%]
θ [°]

(d) Z = 5

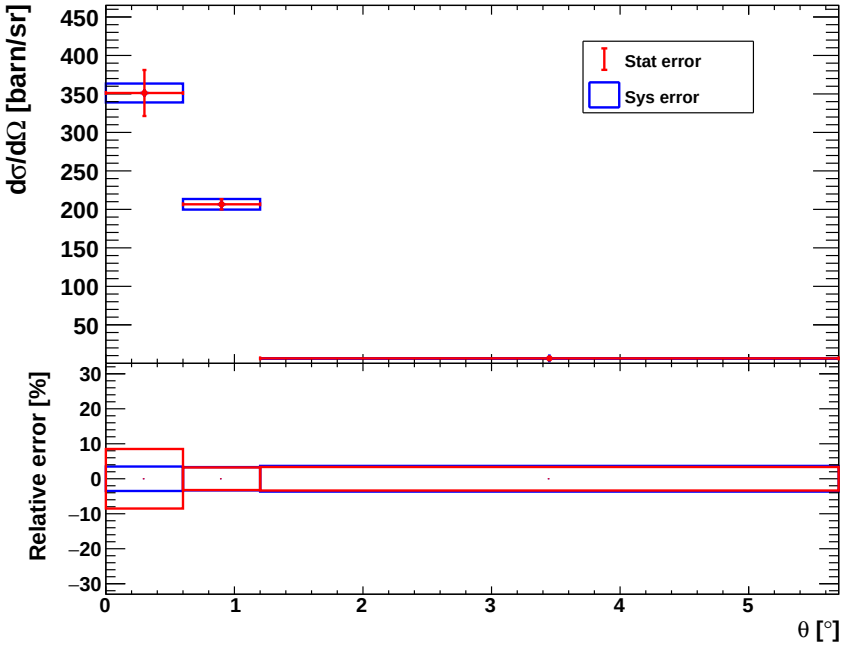

(e) Z = 6

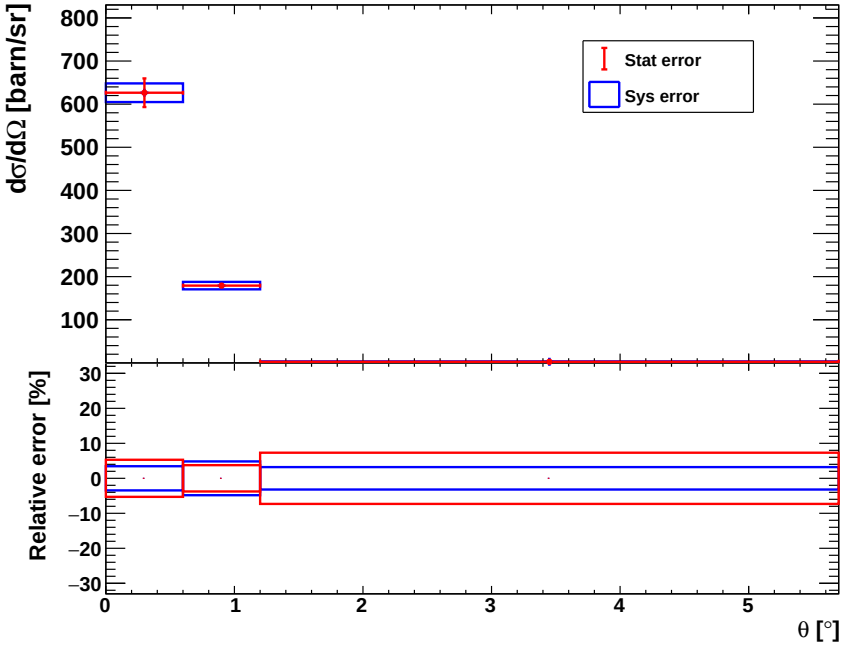

(f) Z = 7

Figure 4.12: Angular cross section for different fragments in fuction of the angle θ; below each plot the systematic and statistical error in percentage is shown.

The total cross section obtained from the integration of the angular one is reported in Figure 4.13, along with statistical and systematic errors. In this case the cross section is expressed in mbarn. The systematic uncertainty, which is always below 5%, is smaller than the statistical one for every fragment, except for He. The statistical uncertainty varies from 1.8% up to a maximum value of 5.4%.

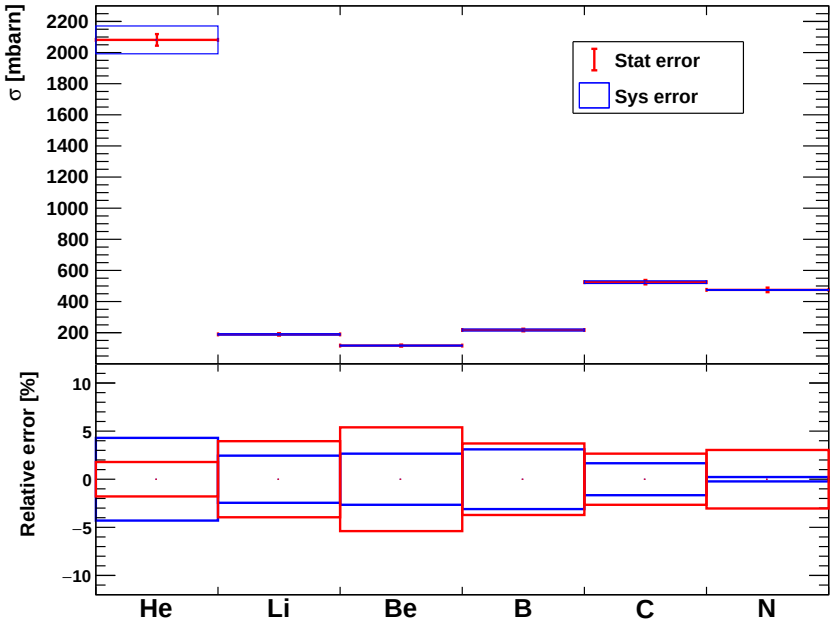

Figure 4.13: Total cross section for different fragment charges.

In Table 4.2 a summary of the total cross sections for different fragment charges is presented for the polyethylene target, along with its statistical and systematic uncertainties.

Fragment	$\sigma \pm \Delta\sigma_{\text{stat}} \pm \Delta\sigma_{\text{sys}}$ [mbarn]	$\Delta\sigma_{\text{stat}}/\sigma$	$\Delta\sigma_{\text{sys}}/\sigma$
He	$2081 \pm 37 \pm 89$	1.8 %	4.3 %
Li	$189 \pm 7 \pm 5$	4.0%	2.4%
Be	$117 \pm 6 \pm 3$	5.4%	2.7%
B	$217 \pm 8 \pm 7$	3.7%	3.1%
C	$524 \pm 14 \pm 9$	2.7%	1.7%
N	$475 \pm 14 \pm 1$	3.0%	0.2%

Table 4.2: Total cross sections with the polyethylene target for different fragments with relative statistical and systematic uncertainty.

4.5.1 Proton cross section

Another reaction of interest that can be studied from the data acquired at GSI in 2021 is the one of a beam of ^{16}O against a proton target. Dealing with a liquid hydrogen target, as already discussed, would be particularly difficult and a gas target would lead to a too low rate of interaction. For this reason the strategy employed by the FOOT experiment is to obtain the cross section of a proton target by subtracting the cross section obtained with a carbon target from the one with a polyethylene target. In particular, the cross section with proton target is given by:

$$\sigma[\mathrm{H}] = \frac{1}{4}\left(\sigma[\mathrm{C_2H_4}] - 2\sigma[\mathrm{C}]\right) \tag{4.6}$$

where $\sigma[\mathrm{C_2H_4}]$ is the cross section with the polyethylene target and $\sigma[\mathrm{C}]$ the one with the graphite (C) target. The same relation also holds for the angular cross section (see Eq. 3.3). The subtraction method has been already exploited in [38], where the fragmentation cross section of a Carbon beam of 95 MeV/u against different targets is studied. In particular the authors of the article validated the possibility to combine the cross sections from different targets, adding and subtracting them. They were able to compare the cross section results obtained with a PMMA target directly with those obtained from single targets of elements composing the PMMA.
To get the proton cross section, a previous result on Carbon target with the same setup and beam settings was used. The results of the subtraction for angular and total cross sections are shown respectively in Figure 4.14 and Figure 4.15. The angular cross section is given in barn/sr, while the total one in mbarn. The uncertainty associated with the cross-section values presented in the plot has been obtained through the propagation of the statistical error. For the total cross section, a summary of the results is provided in Table 4.3.

Fragment	$\sigma \pm \Delta\sigma_{\mathrm{stat}}$ [mbarn]	$\Delta\sigma_{\mathrm{stat}}/\sigma$
He	177 ± 11	6 %
Li	18 ± 2	13%
Be	11 ± 2	19%
B	23 ± 3	12%
C	63 ± 5	7%
N	60 ± 5	8%

Table 4.3: Total cross sections for different fragments for a 400 MeV/u ^{16}O beam against a proton target, together with relative statistical uncertainty.

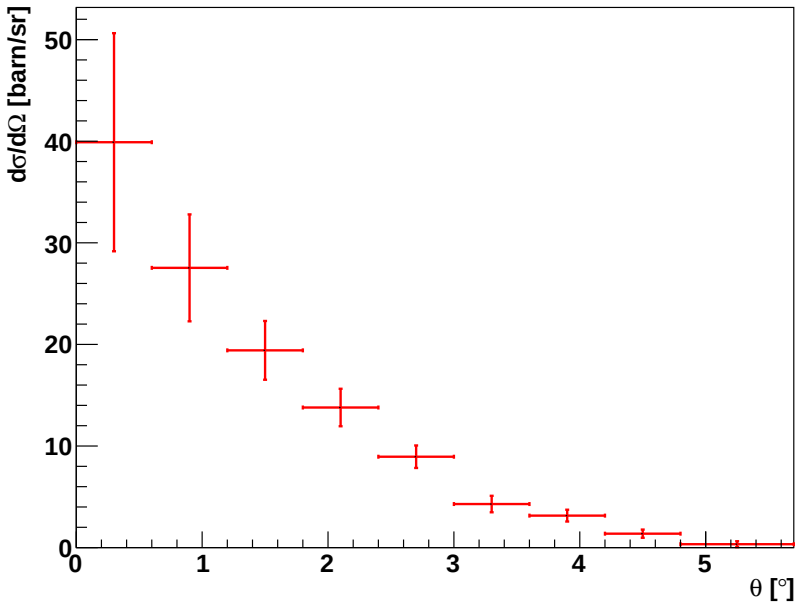
dσ/dΩ [barn/sr]
50
40
30
20
10
0
0
1
2
3
4
5
θ [°]

(a) Z = 2

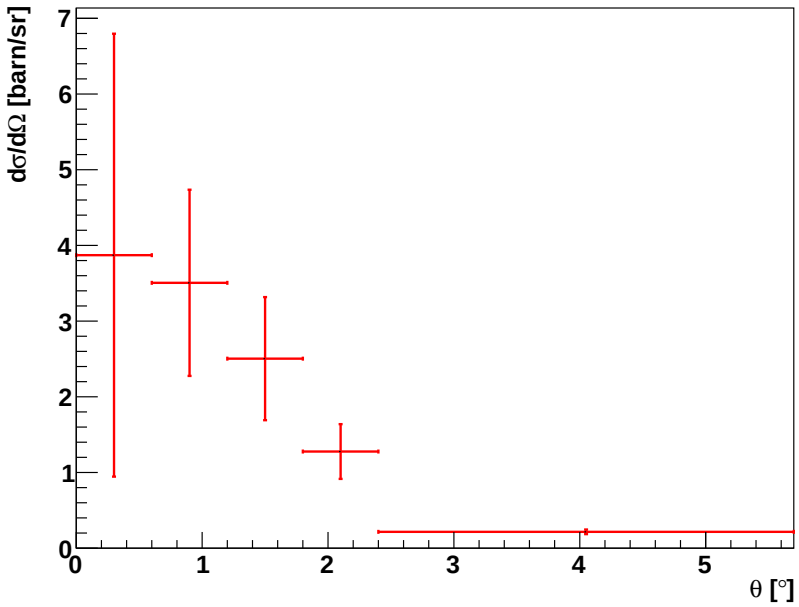
dσ/dΩ [barn/sr]
7
6
5
4
3
2
1
0
0
1
2
3
4
5
θ [°]

(b) Z = 3

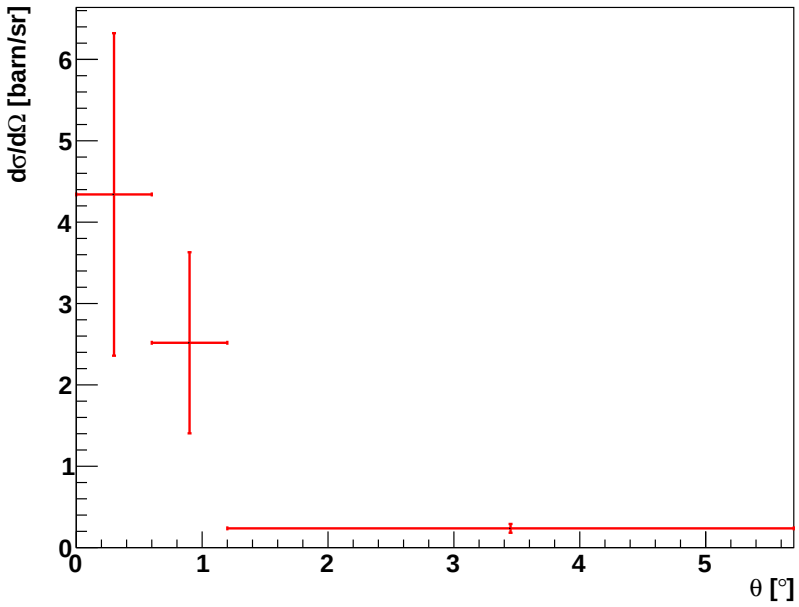

(c) Z = 4

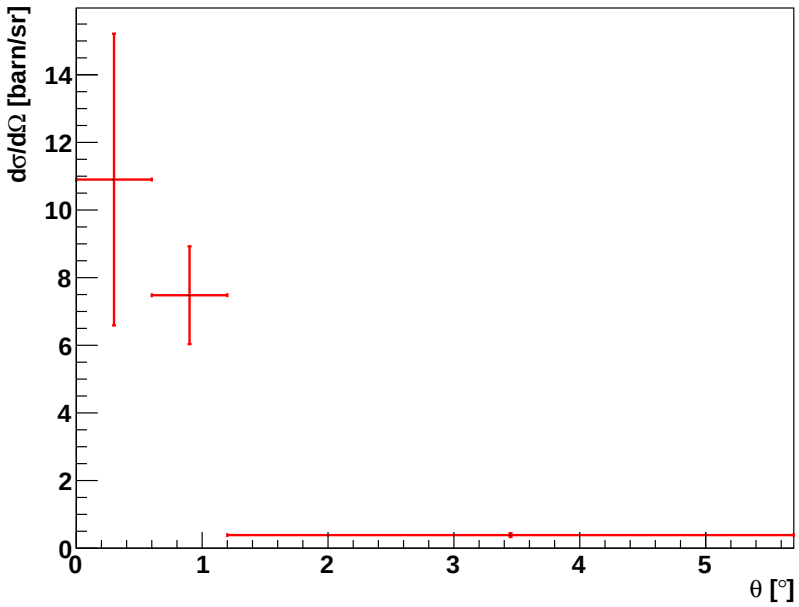

(d) Z = 5

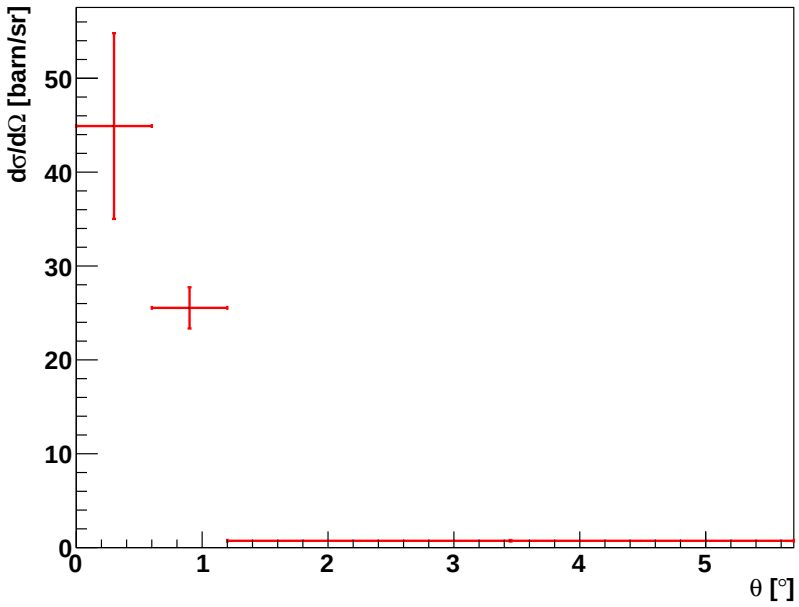

(e) Z = 6

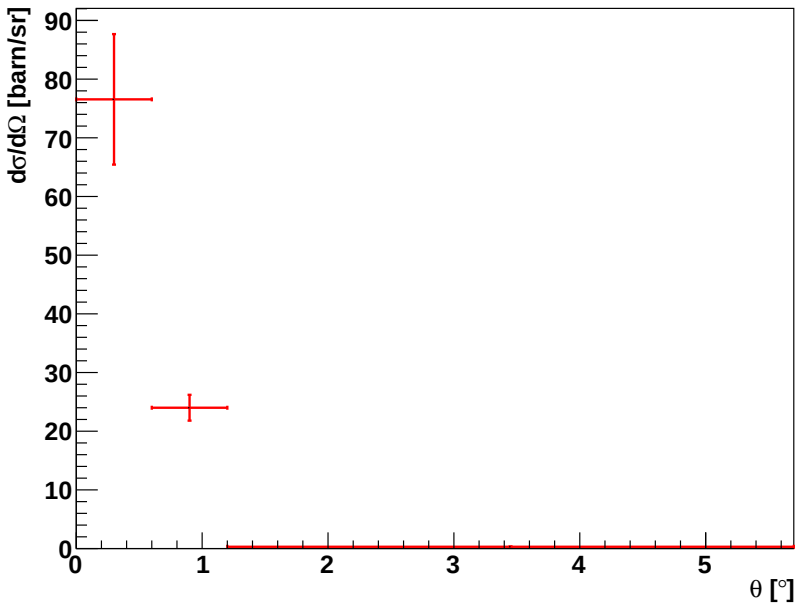

(f) Z = 7

Figure 4.14: Angular cross section for 400 MeV/u ^{16}O beam against a proton target for different charges in function of the angle θ: the cross section has been obtained using Eq. 4.6 with angular cross sections.

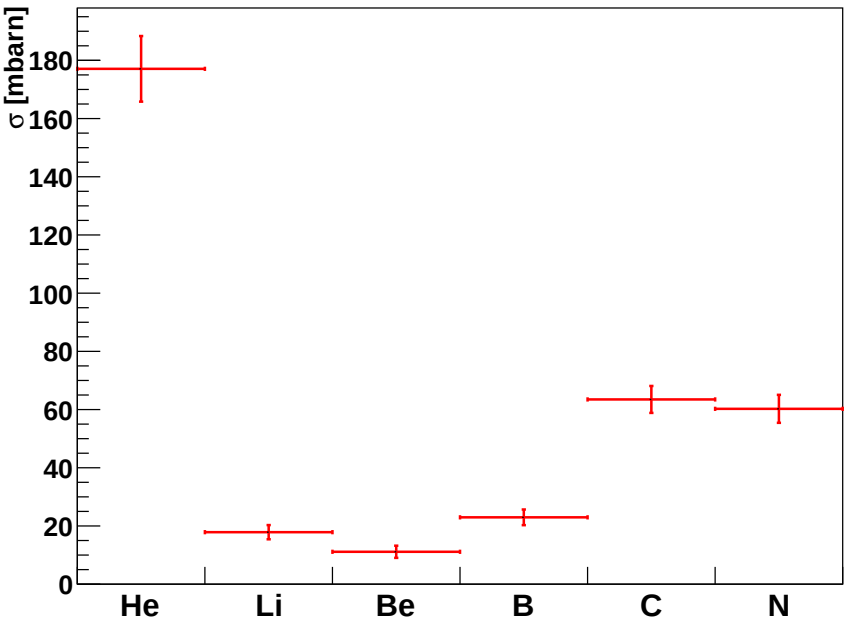

Figure 4.15: Total cross section for 400 MeV/u ^{16}O beam against a proton target for different charges: the cross section has been obtained using Eq. 4.6.

4.6 Literature comparison

As already stated in Section 2.3, the available cross section measurements on nuclear fragmentation are particularly limited. There are some measurements of elemental cross section, but none of differential cross section. In particular, to our knowledge, for a polyethylene target there are no measurements that can be compared with what it has been obtained in this work. A first comparison can however be done with the total cross section obtained for the proton. In [63], measurements of fragmentation nuclear cross sections for different beams at different energies against various targets are presented. The measurements were performed at the NASA Space Radiation Laboratory (NSRL) at the Brookhaven National Laboratory and at the Heavy Ion Medical Accelerator in Chiba (HIMAC) at the Japanese National Institute of Radiological Sciences. All the measurements were performed using different setups composed by silicon detectors. Detectors placed downstream of the target where positioned at various distances from the target in order to cover different acceptance angles. In particular, large acceptance detectors covered 5° up to 10° and could identify species with charge $Z \geq Z_{primary}/2$, while the small acceptance detectors covered 1°-2° and could resolve all fragment species.

Among different beams and targets tested, the total cross section of a 400 MeV/u ^{16}O beam against a proton target was measured. In this case the large acceptance detectors covered an angle up to 6.7° which is closer to the acceptance angle of this analysis. On the other hand, the small acceptance detectors are not considered in this comparison, due to their too small acceptance. The cross sections provided are for B, C and N fragments. The comparison with the results obtained in this work are in Table 4.4 and in Figure 4.16 (in red the results of this thesis, in black the results of [63]). The cross section values result to be compatible within the error.

Fragment	σ[mbarn] (This work)	σ[mbarn] (Ref. [63])
B	23 ± 3	25 ± 2
C	63 ± 5	60 ± 4
N	60 ± 5	58 ± 4

Table 4.4: Total cross sections for B, C and N for a 400 MeV/u ^{16}O beam against a proton target from this work and from [63].

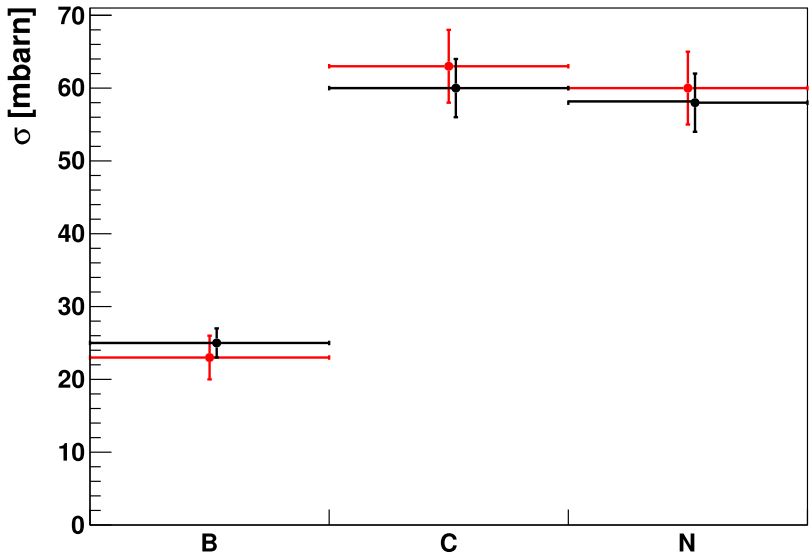

Figure 4.16: Total cross section for a 400 MeV/u ^{16}O beam on a proton target for B, C, and N: the cross sections obtained from this thesis analysis are shown in red, while the cross sections from [63] are shown in black. The black points have been slightly shifted to the right for better visualization of the error bars.

Conclusions

The aim of the FOOT (FragmentatiOn Of Target) experiment is to provide precise measurements of nuclear fragmentation total and double differential cross section in angle and kinetic energy of the resulting fragments. These measurements are relevant both in the hadrontherapy field, contributing to improving cancer treatment, and in the field of space radioprotection, where measurements are needed to protect astronauts from cosmic radiation. The FOOT experiment is composed of two different setups: an electronic setup and an emulsion setup optimized for light fragments with a large acceptance angle.
In this thesis work, I analyzed data taken in July 2021 at GSI (in Darmstadt, Germany) with the electronic setup. At the time, the setup was not complete yet, consisting only of a Start Counter, a scintillator used to provide the trigger signal, a Beam Monitor, a drift chamber before the target and a Tof Wall, two layers of scintillator bars used to identify the charge of the produced fragments.
The data were acquired using 200 MeV/u and 400 MeV/u ^{16}O beams against a 5 mm carbon target and a 5 mm and 10 mm polyethylene target. I worked on data taken at 400 MeV/u with the 10 mm thick polyethylene target, obtaining the total and differential cross sections in angle for different fragments. With this setup, it was possible to obtain elemental fragmentation cross sections for different fragment charges.
To account for the contribution of out-of-target fragmentation, a run without the target was used to subtract the background. To consider the detector resolution, an angular unfolding procedure was applied.
The same analysis carried out on the data was also applied to a MC sample, including background subtraction and angular unfolding. The MC was used to validate the analysis technique and to extract geometrical efficiency, TW reconstruction efficiency and charge identification capability. From the MC, the systematic uncertainties of the measurements, related to the analysis method employed, were also extracted.
From the data, the total cross section of all fragments as well as differential angular cross section were obtained within the angular acceptance range, from 0° to 5.7°.
Using a previous result on a Carbon target with the same setup and beam settings, it was also possible to extract the total and angular differential cross section on a Hydrogen target via subtraction from the polyethylene cross section.
For the proton total cross section, a comparison with other available measurements was

made for B, C and N fragments. The results were compatible with the few experimental data available within the errors.
In conclusion, the analysis conducted within this thesis has demonstrated the capability of the FOOT experiment to measure total and differential angular cross sections, using a background subtraction method.
This analysis provides useful feedback to further improve cross section measurements using the tracking system in the next future.
The detector is now complete and other data have been acquired: we expect from these new samples more precise results due to the larger acquired statistics and significant improvements of the detector.

Appendix A

He-check: setup analysis

In this appendix I will describe the work carried out during the period of my master's studies spent at CNAO, contributing to the He-check project. The project aims to perform dose verification during patient treatment sessions. The idea behind the project is to simultaneously accelerate a Carbon and a Helium beam, exploiting their almost equal rigidity. Due to their mass difference, Carbon releases its energy in the tumor, while Helium exits the patient, releasing its energy in a detector. From the position and residual range of Helium, it is possible to reconstruct the traversed density and thickness. More details on this can be found in Section 2.1.3.

A.1 Experimental setup

The studied setup for the He-check project consists of a $l_s = 20\,\text{cm}$ side plastic scintillator cube coupled with a scientific CMOS camera. The system is placed inside a box with completely black walls to minimize external light reaching the sensor. The box has a lateral aperture through which the particle beam can enter.
For a more accurate reconstruction of the light produced by the particle beam, I have performed an analytical study of the geometrical optics of the setup.
The centre of the coordinates used in this work is depicted in Figure A.1, where the setup is viewed from above in the two different configurations. The origin of the Y coordinate, representing the height, is positioned at the middle of the scintillator. The camera is located at a distance L from the proximal side of the scintillator, centered at Y = 0 and aligned with the origin of the coordinate system, but can be laterally moved along the Z direction. The particle beam is directed towards the Z direction, impacting the lateral side of the scintillator.
Two main configurations are shown in Figure A.1: one with the camera centered in the middle of the scintillator in the Z direction, and the other with the camera aligned with the side of the scintillator. In the second configuration, a mirror is added at an angle β

relative to the side of the scintillator. The mirror enables observation of the X position of the light, facilitating the reconstruction of the transverse position of the Bragg peak. In both figures, α represents half of the camera's Field Of View (FOV) angle along the Z direction.
The camera model is Ando Zyla 5.5 sCMOS and it has 2560 $\times$ 2160 pixel, with a sensor dimension of 16.6 mm $\times$ 14 mm. The scintillator is a BC-408 plastic scintillator cube with a refractive index $n = 1.58$.

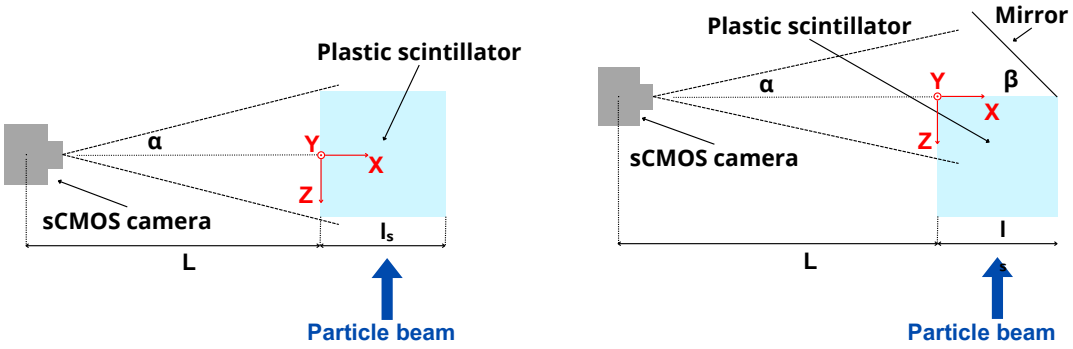

Figure A.1: Schematic setup of the scintillator and camera seen from above in two main configurations: on the left, the camera is centered in the Y-Z directions of the scintillator; on the right, a mirror is added, while the camera is aligned with the side of the scintillator and centered in the Y direction.

Lens parameters

The position of the camera relative to the scintillator is a crucial parameter. From the distance L, it is possible to derive the Field Of View (FOV) of the camera in the Y and Z directions. Considering the sensor dimension h and the focal length f, the field of view angle is given by: $\alpha = arctan\left(\frac{h}{2f}\right)$. From this equation the FOV can be calculated as

$$FOV = \frac{Lh}{f} \tag{A.1}$$

Figure A.2 illustrates a schematic representation of the field of view and its relation with the camera's sensor. Since the sensor is not a perfect square, the field of view differs slightly between the Y and Z directions. The camera is oriented such that the longer side of the sensor aligns with the Z direction.
When the camera is centered with respect to the scintillator (configuration on the left side of Figure A.1), the frontal side of the scintillator can be seen completely in both dimensions already from 360 mm, while if the camera is moved laterally (right side of Figure A.1), the scintillator is completely visible from 610 mm. Another important

parameter to define is the depth of field, which is the distance between the nearest and farthest objects that are acceptably sharp in focus in an image. It is required that the entire scintillator remains in focus. The depth of field depends strongly on the focal distance f, the f-number $F_/$, defined as the ratio of the focal length to the aperture diameter, and the circle of confusion. The circle of confusion is the diameter of the blurred image produced by a point-like object located outside the depth of field.

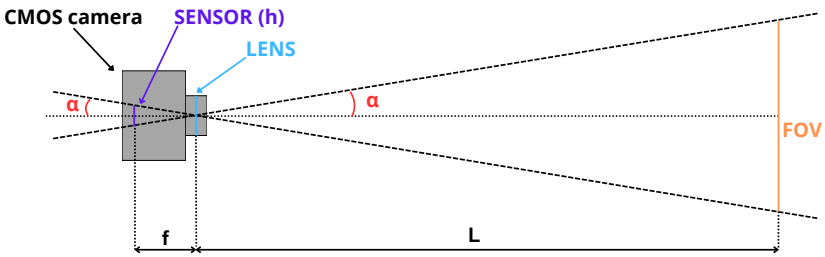

Figure A.2: Schematic representation of the field of view.

The distances from the camera of the nearest object in focus d_{prox} and farthest object in focus d_{dist} are given by:

$$d_{prox(dist)} = \frac{f^2 d}{f^2 + (-)c(d-f)F_/} \tag{A.2}$$

where d is the focus distance.
The pixel dimensions of the camera are $6\,\mu$m $\times$ $6\,\mu$m. Without any binning during the acquisition, the circle of confusion can be taken equal to the pixel dimension. Considering a focal length of 25 mm and an exposure time of 10 ms, $F/16$ is the optimal aperture to obtain a clear image in the experimental condition studied. At a focus distance $d = 70$ cm, the depth of field covers the entire dimension of the scintillator, ensuring it appears completely in focus.
The camera lens used in the setup consists of a system of multiple lenses. Hence, it is possible to estimate the virtual position of a lens that would correspond to this system. Given the focal distance of the lens $f = 25$ mm, we can assume the virtual position of the camera sensor at this distance. The length L, introduced earlier in Section A.1, represents the distance from the scintillator to the position of this virtual lens. To determine the position of the virtual lens, field of view measurements were conducted at various distances from the camera's support. These measurements were subjected to a linear fit, and the intersection point of the straight line with the X-axis indicates the position of the virtual lens. The position of the virtual lens obtained by the fit is (34 ± 2) mm from the camera's support. It is important to note that the FOV value depends on the camera's focusing settings and the positioning of the camera's objective. In reality, the camera lens comprises a complex system of lenses rather than a single lens. Therefore,

this measurement serves as an estimate rather than an exact value of the virtual lens' position.

Refraction and reflection

The scintillator has a refractive index of $n_2 = 1.58$, which differs from the refractive index of air, $n_1 = 1$. Correctly reconstructing the position of an object inside the scintillator requires consideration of the refraction of optical rays entering from outside (see Figure A.5a). In Figure A.3 a schematic with the parameters to study an optical ray coming from behind the scintillator is illustrated. From the picture, the real position of the object Z_{true} and the Z_{app} are given by:

$$Z_{true} = Z_1 + Z_2 = L \tan\theta_1 + l_s \tan\theta_2 \tag{A.3}$$

$$Z_{app} = (L + l_s) \tan\theta_1 \tag{A.4}$$

where θ_1 and θ_2 are the incident angles of the optical ray in air and inside the scintillator, respectively.

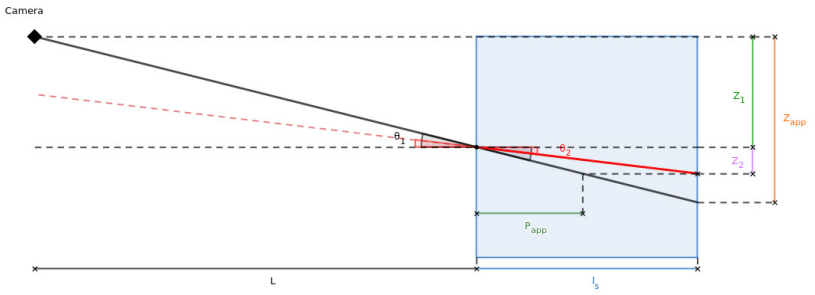

Figure A.3: Schematic representation of the refraction of an optical ray originating from behind the scintillator.

The two angles are related by Snell's law: $n_1 \sin\theta_1 = n_2 \sin\theta_2$. The Z positions are calculated with respect to the reference frame introduced in Section A.1. An object positioned behind the scintillator will appear on the camera at an apparent position at a distance $L + P_{app}$ from the camera, where $P_{app} = Z_2 / \tan\theta_1$. This calculation applies similarly in the Y direction.
If the optical ray originates not from directly behind the scintillator but from a distance X_{true} from the farthest side of the scintillator to the camera, the formulas change substituting $l_s - X_{true}$ to l_s. In the analysis performed in Section A.2, the variable Z_{app} is used for convenience instead of the corresponding apparent position along the X-axis. When the scintillator is positioned at $L = 650\,\text{mm}$ from the camera, the refraction of

light results in a maximum magnification effect of approximately $\sim 10\,\%$. This effect was verified by placing a sheet of graph paper behind the scintillator and measuring the position of a dot through the scintillator relative to its known position on the graph paper.
Another significant effect that occurs within the scintillator is reflection. Optical rays are internally reflected from the lateral sides of the scintillator and, given the refractive index of the scintillator, the critical incident angle for total internal reflection is $\approx 40°$. Through analytical analysis, it is possible to calculate the actual position of an object after single internal reflection. For instance, with the camera positioned as in the right side of Figure A.1, at a distance $L = 650\,\text{mm}$, only the last $37.9\,\text{mm}$ in the Z direction are reflected, perceived by the camera as $41.6\,\text{mm}$ due to refraction.

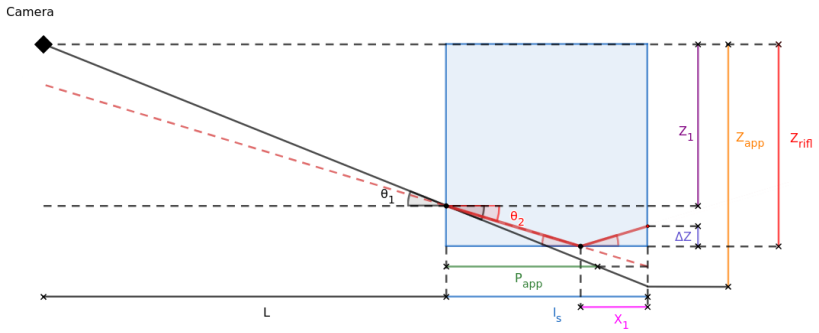

Figure A.4: Schematic view of the reflection of an optical ray originating from behind the scintillator.

For simplicity, the case of an optical ray originating from behind the scintillator will be considered first, followed by the case of an optical ray originating from within the scintillator.
From Figure A.4, which illustrates a schematic view of reflection process, Z_{app} of an object behind the scintillator is still given by Eq. A.4. As previously shown in Eq. A.3, $Z_1 = L \tan\theta_1$. The true position can be derived through the following calculations:

$$l_s - x_1 = (Z_{refl} - Z_1)\frac{1}{\tan\theta_2} \tag{A.5}$$

$$\Delta z = x_1 \tan\theta_2 \qquad Z_{true} \;= Z_{refl} - \Delta z \tag{A.6}$$

where Z_{refl} indicates the position of the scintillator side where reflection occurs relative to the camera. An object positioned behind the scintillator will appear in the camera as if it were located at a distance $L+P_{app}$ from the camera, where $P_{app} = (Z_{refl}+\Delta z - Z_1)/\tan\theta_1$. To observe reflection, the values of the x_1 and Δz variables must be positive: objects

in positions that do not meet this requirement are not reflected or their reflection does not reach the camera. For instance, with the camera positioned as in Figure A.4, at a distance $L = 650\,\text{mm}$, only the last 37.9 mm in the Z direction are reflected, perceived by the camera as 41.6 mm due to refraction. Light originating from behind the scintillator is the most affected by reflection.
In Eq. A.6, to determine the true position of an optical ray originating from a distance X from the proximal side of the camera, it is needed to replace l_s with X, noting that fewer positions are visible through reflection. The same calculations apply for the Y dimension, considering refraction.

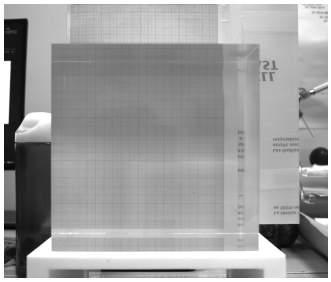

(a) Zoom of a photo taken by the camera of the scintillator cube in the configuration on the left side of Figure A.1. The effect of refraction is clearly visible from the distortion of the graph paper sheet placed behind the scintillator.

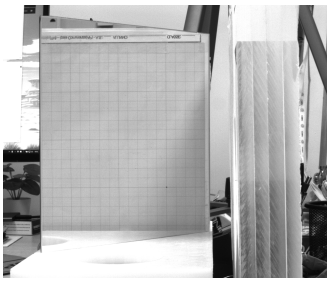

(b) Zoom of a photo taken with the camera: the mirror is positioned at a 45° angle relative to the camera's line of sight. A sheet of graph paper is positioned at a minimum distance of 2.2 cm.

Figure A.5: Some photos taken with the camera

Mirror setup

As mentioned in Section A.1, in the configuration where the camera is aligned with the side of the scintillator, a mirror can be added to capture an image of the lateral position of the light emitted by a particle beam. This setup is depicted on the right side of Figure A.1, with the mirror positioned at an angle β relative to the side of the scintillator. Due to experimental constraints, reconstructing the lateral position is not straightforward, and its complexity increases significantly with even small changes to the setup.
In reality, the setup differs slightly from the one depicted in Figure A.1 because the scintillator is positioned on a support that leaves a gap of 2.2 cm along Z. Consequently, the edge of the mirror does not touch the scintillator but instead maintains a distance of 2.2 cm from it. The mirror itself is a square of the same dimensions as the scintillator, $l_s = 200\,\text{mm}$. The simplest and effective configuration chosen is $\beta = 45°$, where the lateral side of the scintillator is reflected straight, as shown in Figure A.5b, due to the

perpendicular reflection of optical rays. Referring to Figure A.6, the reflection of the closer side AB of the scintillator, is seen from the camera at a distance equal to the one of side BD from the camera plus 2.2 cm, behind the mirror. Due to the dimension of the mirror and the angle chosen, AB is not reflected entirely. At a distance $L = 650$ mm, only approximately 179 mm are visible. Similarly, the other edge of the same face of the scintillator, B, is not fully contained within the mirror, as the mirror is positioned 2.2 cm away from the scintillator. In this case, the portion of the face not reflected in the mirror is sufficiently small to be considered negligible. To reflect the entire scintillator, a larger mirror could be chosen, or alternatively, the mirror could be positioned at an angle greater than 45°. However, in the latter case, the reflected image would not precisely match the original. In fact the reflected image would appear behind the mirror at an angle β relative to the scintillator and its reconstruction would be more complex because each point of the reflected image is at a different depth relative to the camera, thus having a different value in mm/pixels. Hence, the optimal solution would be a larger mirror to reflect the entire scintillator; a dimension of 230 cm would suffice.

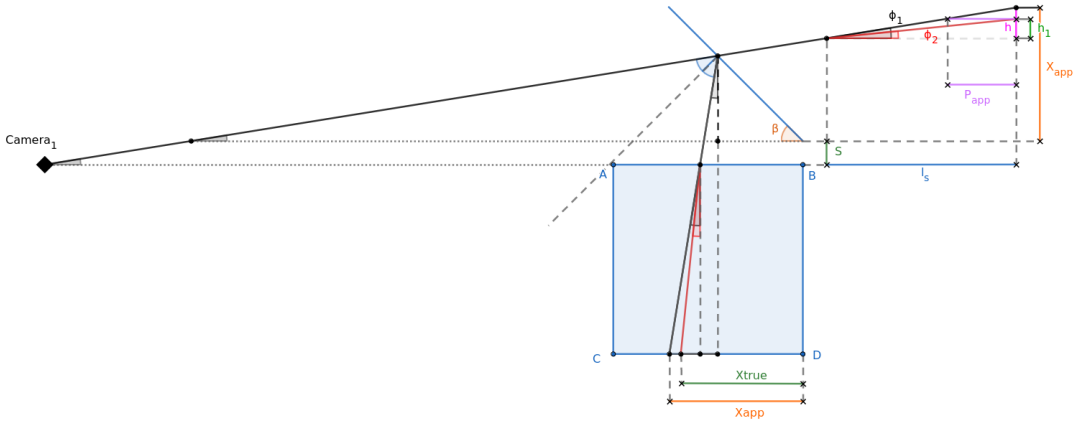

Figure A.6: Geometric construction used to calculate the X position of a point located at $Z = l_s$ considering refraction inside the scintillator.

Regarding the further side of the scintillator relative to the mirror, CD, edge C is reflected, while D is not visible in the mirror reflection. Specifically, from D, almost half a centimeter is missing from the reflection in the mirror. To resolve this issue, two solutions are possible: eliminate the 2.2 cm gap between the mirror and the scintillator by using a different support, or move the mirror the same distance behind the scintillator. With the second option, a larger mirror, such as one measuring 240 mm, would be necessary to see point A adequately.
The information from the mirror can provide the X position of a point inside the scintillator. To correctly reconstruct the X position, however, it is necessary to consider the refraction

of light. As previously done, the easiest approach is to start with a point positioned at the back of the scintillator, which corresponds to $Z = l_s$. The geometric construction of the system is represented in Figure A.6.
Considering the variables introduced in the figure, the following equations hold:

$$\tan\phi_1 = \frac{X_{app} + s}{L + 2l_s + s} \tag{A.7}$$

$$X_{true} = X_{app} - (h - h_1) = X_{app} - l_s(\tan\phi_1 - \tan\phi_2) \tag{A.8}$$

where the two angles are related by Snell's law. The object will appear at an apparent position P_{app} behind the mirror, as shown in Figure A.6.
The X position of the point relative to the side of the scintillator closest to the camera is $X'_{true} = l_s - X_{true}$.
If the object is not at $Z = l_s$, but at certain Z_{true}, the equations change as follows:

$$\tan\phi_1 = \frac{X_{app} + s}{L + l_s + Z_{true} + s} \tag{A.9}$$

$$X_{true} = X_{app} - (h - h_1) = X_{app} - Z_{true}(\tan\phi_1 - \tan\phi_2) \tag{A.10}$$

while the others remain the same.

A.2 Position reconstruction

The reconstruction of the position of a certain point inside the scintillator requires information about all three coordinates, with the X coordinate given by the mirror. The apparent positions due to refraction can be estimated given the number of pixels for that position, n_{pixels} and the mm/pixel corresponding to that specific depth with respect to the camera. Calling K_d the mm/pixel corresponding to a depth d from the proximal side of the scintillator to the camera (which is at $d = 0$) it is possible to obtain the following relation:

$$K_d = d\frac{K_{l_s} - K_0}{l_s} + K_0. \tag{A.11}$$

Using this equation, the apparent position in X and Z will be given by:

$$X_{app} = \left(d\frac{K_{l_s} - K_0}{l_s} + K_0\right) n_{xpixels} = \left((l_s + s + Z_{true})\frac{K_{l_s} - K_0}{l_s} + K_0\right) n_{xpixels} \tag{A.12}$$

$$Z_{app} = \left(d\frac{K_{l_s} - K_0}{l_s} + K_0\right) n_{zpixels} = \left((l_s - X_{true})\frac{K_{l_s} - K_0}{l_s} + K_0\right) n_{zpixels} \tag{A.13}$$

For Y_{app} the same equation used for Z_{app} holds, substituting n_{zpixel} with n_{ypixel}. The variables n_{xpixel}, n_{ypixel} and n_{zpixel} are the coordinates in pixels, corresponding to the apparent position of the point to be reconstructed. Combining Eq. A.3 and Eq. A.4, it is possible to obtain:

$$Z_{true} = \frac{LZ_{app}}{L + l_s - X_{true}} + (l_s - X_{true}) \tan\left(\arcsin\left(\frac{\sin(Z_{app}/(L + l_s))}{n_2}\right)\right) \tag{A.14}$$

The Y_{true} position is obtained using the same equation used for Z_{true}, substituting Z_{app} with Y_{app} The X'_{true} position from the side of the scintillator closer to the camera, as already mentioned in Section A.1, is:

$$X'_{true} = l_s - X_{true} = l_s - X_{app} - Z_{true}(\tan\phi_1 - \tan\left(\arcsin\left(\frac{\sin\phi_1}{n_2}\right)\right) \tag{A.15}$$

with X_{true} shown in Figure A.6 and $\tan\phi_1$ given by Eq. A.9.

A.3 Image acquisition and analysis

Acquisition setup and parameters

A preliminary image acquisition with the particle beam has been carried out to test the calculations and formulas derived so far. The setup used was the one shown in Figure A.1 on the right, with the camera aligned laterally with the scintillator and the beam coming from the Z direction.

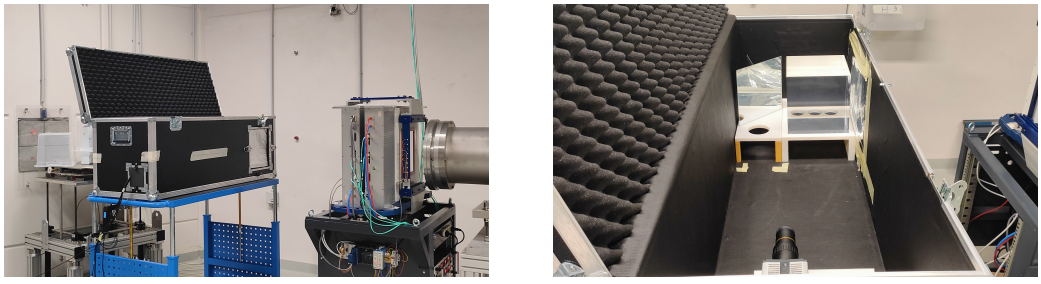

(a) (b)

Figure A.7: Setup inside the experimental room at CNAO: Figure A.7a shows the box containing the setup with the lateral window in front of the particle beam; the aperture for the particles is also visible. Figure A.7b shows the scintillator and the mirror correctly positioned inside the box.

The measurements were performed at a distance of $L = 650\,\text{mm}$ from the camera to capture a complete view of both the scintillator and the mirror as stated in the previous

sections. After aligning the setup and positioning the box correctly, a reference image with the box open was taken. From this image, the values of K_0 and K_{l_s} mentioned in Eq. A.11 were verified by measuring the number of pixels of objects at a specific distance with a known length. The value of K_0 was determined knowing that the scintillator side closer to the camera is positioned at $d = 0$ and its length is 200 mm, giving $K_0 = 0.16$ mm/pixel. K_{l_s} was obtained from the mirror side positioned at $d = 200$ mm, which is also 200 mm long, resulting in $K_{l_s} = 0.21$ mm/pixel.
Some background images were also taken to serve as a baseline reference and to be subtracted from the subsequent images acquired.
The background images were taken with the box closed under different lighting conditions: with the lights on, off, and with and without a dark blanket above. All these images exhibited almost the same mean pixel intensity, indicating that the box is already quite effective at blocking any external light sources.
The images were acquired with the camera configured to use an external trigger, using the initial start-of-spill signal, which indicates the beginning of particle beam emission, as the trigger signal. The camera acquired a kinematic series of images whose length was set manually. The images were taken by irradiating the scintillator with carbon and proton beams at different energies corresponding to depths in water of 30 mm, 60 mm, 100 mm, 140 mm, and 180 mm for carbon, and 30 mm, 60 mm, 101 mm, 141 mm, and 181 mm for protons. The carbon beam was delivered in a grid of 9 spots separated by 26 mm, containing 5×10^6 particles each, and in a grid of 25 spots separated by 26 mm, containing 10×10^6 particles each. For the proton beam, the grid was composed of 9 spots separated by 30 mm, each containing 10×10^6 particles. The chosen exposure time for the acquisition was 50 ms and the aperture of the camera was set at F/16.

Image analysis

This section presents the analysis of the images obtained with the proton beam, as it was possible to separate each spot from the others in different image frames.
Figure A.8 shows an image obtained from the camera and the corresponding image obtained after subtracting the background. On the right side of the image, the range of the particles in the scintillator is visible, while on the left, there is the spot corresponding to the reflection in the mirror. A median filter was also applied to the images to remove noise spots caused by hot pixels. To reconstruct the range correctly, a software was developed. The goal is to reconstruct, using the equations summarized in Section A.2, the position of the Bragg peak. Firstly, the image is integrated along the vertical direction to identify the pixels corresponding to the Bragg peak and the center of the spot in the mirror. The result for the image in Figure A.8 is shown in Figure A.9.
On the right side, the characteristic shape of the Bragg peak is clearly visible. The last 197 pixels of the peak before the intensity drop are due to the reflection of light inside the scintillator. The position of the peak in the mirror is obtained by fitting the peak locally

with a Gaussian and determining the position of the maximum of the fit. The position of the Bragg peak is instead obtained as the 90 % of the maximum on the descending edge. These pixel positions are then used to evaluate n_{xpixel} and n_{zpixel}, introduced in Eq. A.12 and Eq. A.13.
The system of equation presented in Section A.2 is then solved numerically, yielding the values of Z_{true} from the center of the image, where the camera is aligned, and X'_{true} from the side of the scintillator closer to the camera. The value of the range is then simply obtained by subtracting Z_{true} from l_s, the length of the scintillator.

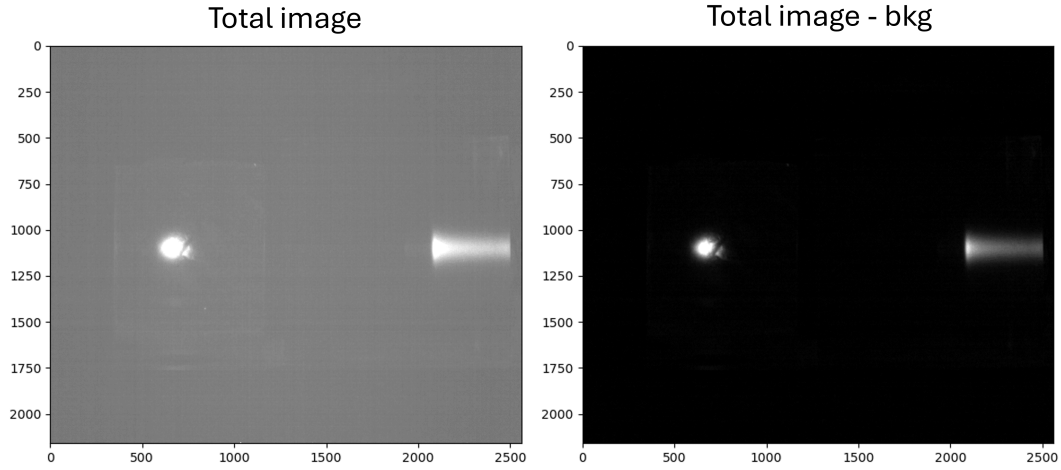

Figure A.8: Image obtained from the camera and the corresponding one with background subtraction. The light is produced from a beam of protons with a 60 mm range in water, corresponding to an energy of 90 MeV.

The n_{ypixel} is instead obtained by integrating horizontally the portion of the total image containing only the light coming from the scintillator and taking the center of the luminous region. To help visualize the X and Y positions, Figure A.10 provides a schematic representation of the setup seen laterally from the direction of the beam.
As an example, the results obtained for protons with ranges of 60 mm and 101 mm, corresponding to 90 MeV and 118 MeV respectively, are shown in Table A.1 and Table A.2. In the first two columns of the tables, the reference positions in X and Y of the spots assuming perfect alignment of the setup with the beam. The values of the Y coordinate exhibit slight variations from their reference values and are all compatible, indicating a setup misalignment along Y of approximately 3 mm which is plausible. However, the X values show clear discrepancies compared to their reference values and also differ among themselves. These discrepancies may be due to a misalignment of the setup in the X coordinate, amounting to nearly 1 cm, as well as potential issues with the reconstruction

code. Some defects due to aging in the scintillator cause some spots to be distorted and badly defined, making it challenging to accurately identify the central pixel.
The range values obtained from the analysis appear to be quite compatible among themselves within 1 mm. Summarizing the results by computing the mean of the values obtained for each of the 9 spots, the ranges obtained are: (32.3 ± 0.1) mm, (61.6 ± 0.1) mm, (101.2 ± 0.1) mm, (140.3 ± 0.1) mm and (179.5 ± 0.1) mm. Considering that inside the scintillator, the expected proton ranges are 32 mm, 61 mm, 101 mm, 140 mm and 180 mm, the values calculated are compatible with the expected ones.

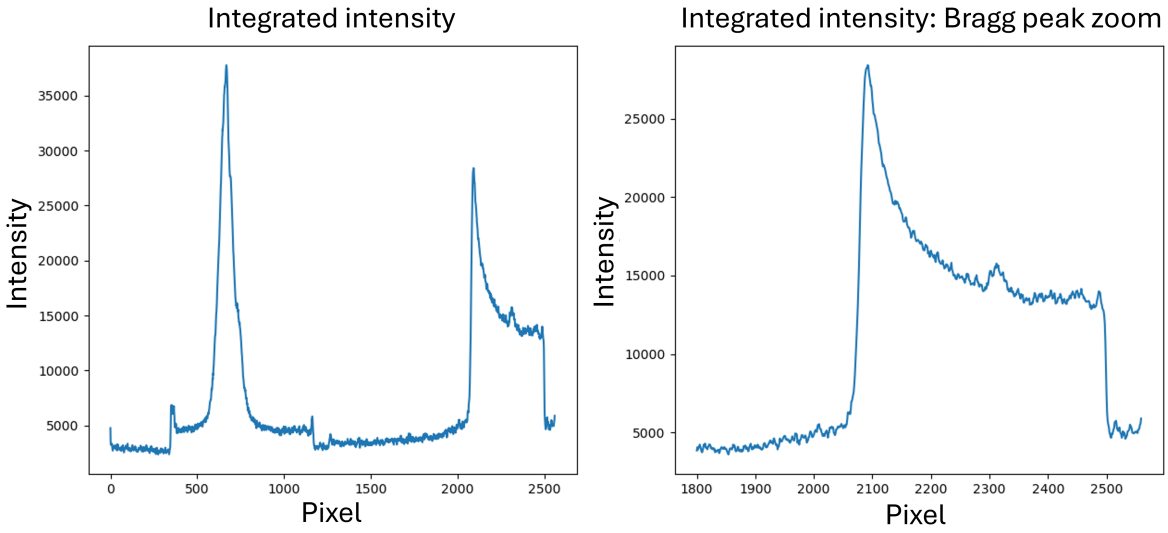

Figure A.9: Integrated intensities along the vertical direction of the image. On the left, the total image is shown, where the peaks related to the spot in the mirror and the Bragg peak are visible. On the right, a zoom of the Bragg peak is shown. The plot refers to the image in Figure A.8, protons at 90 MeV.

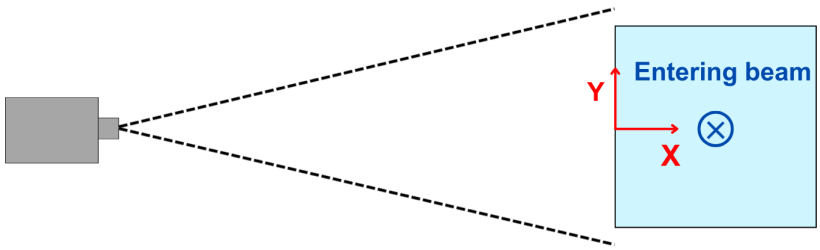

Figure A.10: Schematic view of the setup seen from the direction of the beam entering the foil. The coordinate system used in the following results is also shown from this perspective.

$\mathbf{X_{ref}}$**(mm)**	$\mathbf{Y_{ref}}$**(mm)**	**X (mm)**	**Y (mm)**	**Range (mm)**
130	-30	138.6	-33.0	61.6
100	-30	110.5	-33.4	61.4
70	-30	82.4	-33.3	60.9
70	0	80.6	-2.8	61.4
100	0	111.2	-3.5	61.7
130	0	138.8	-3.6	61.9
130	30	141.2	26.5	62.0
100	30	111.7	26.9	62.0
70	30	81.5	27.2	61.5

Table A.1: Results of image analysis for protons at 90 MeV, with a range in water of 60 mm. In the first two columns, the reference value of the beam position in X and Y is shown.

$\mathbf{X_{ref}}$**(mm)**	$\mathbf{Y_{ref}}$**(mm)**	**X (mm)**	**Y (mm)**	**Range (mm)**
130	-30	137.3	-33.6	101.3
100	-30	109.7	-33.5	101.0
70	-30	83.7	-33.5	100.4
70	0	80.8	-3.3	101.0
100	0	111.4	-3.3	101.4
130	0	137.8	-3.6	101.6
130	30	139.2	27.0	101.8
100	30	111.8	26.9	101.5
70	30	81.7	27.1	101.1

Table A.2: Results of image analysis for protons at 118 MeV, with a range in water of 101 mm. In the first two columns, the reference value of the beam position in X and Y is shown.

Bibliography

[1] W.R. Leo. *Techniques for Nuclear and Particle Physics Experimentes - A How-to Approach, 2nd edition*. Springer-Verlag Berlin Heidelberg, 1994. DOI: 10.1007/978-3-642-57920-2.

[2] Particle data group. *Passage of particles through matter*. 2021. URL: https://pdg.lbl.gov/2022/reviews/rpp2022-rev-passage-particles-matter.pdf.

[3] Wayne D Newhauser and Rui Zhang. "The physics of proton therapy". In: *Physics in Medicine and Biology* 60.8 (Mar. 2015), R155. DOI: 10.1088/0031-9155/60/8/R155. URL: https://dx.doi.org/10.1088/0031-9155/60/8/R155.

[4] Steven P. Ahlen. "Theoretical and experimental aspects of the energy loss of relativistic heavily ionizing particles". In: *Rev. Mod. Phys.* 52 (1 Jan. 1980), pp. 121–173. DOI: 10.1103/RevModPhys.52.121. URL: https://link.aps.org/doi/10.1103/RevModPhys.52.121.

[5] G. F. Knoll. *Radiation detection and measurement*. New York, NY: Wiley, 2010.

[6] H. A. Bethe. "Molière's Theory of Multiple Scattering". In: *Phys. Rev.* 89 (6 Mar. 1953), pp. 1256–1266. DOI: 10.1103/PhysRev.89.1256. URL: https://link.aps.org/doi/10.1103/PhysRev.89.1256.

[7] Danielewicz P. and Bertulani C. *Introduction to Nuclear Reactions (2nd ed.)* CRC press, 2021.

[8] A. C. Kraan. "Range Verification Methods in Particle Therapy: Underlying Physics and Monte Carlo Modeling". In: *Frontiers in Oncology* 5 (2015). ISSN: 2234-943X. DOI: 10.3389/fonc.2015.00150. URL: https://www.frontiersin.org/journals/oncology/articles/10.3389/fonc.2015.00150.

[9] R. Serber. "Nuclear Reactions at High Energies". In: *Phys. Rev.* 72 (11 Dec. 1947), pp. 1114–1115. DOI: 10.1103/PhysRev.72.1114. URL: https://link.aps.org/doi/10.1103/PhysRev.72.1114.

[10] R.J. Glauber. *Lecture on Theoretical Physics*. 1959.

[11] S. Kox et al. “Trends of total reaction cross sections for heavy ion collisions in the intermediate energy range”. In: *Phys. Rev. C* 35 (5 May 1987), pp. 1678–1691. DOI: 10.1103/PhysRevC.35.1678. URL: https://link.aps.org/doi/10.1103/PhysRevC.35.1678.

[12] M.Y.H. Farag. “Modified Glauber model for the total reaction cross-section of ^{12}C + ^{12}C collisions”. In: *The European Physical Journal A* 12.4 (2001), pp. 405–411. DOI: 10.1007/s10050-001-8664-2.

[13] H. L. Bradt and B. Peters. “The Heavy Nuclei of the Primary Cosmic Radiation”. In: *Physical Review* 77 (1950), pp. 54–70. DOI: 10.1103/PhysRev.77.54.

[14] Badawy Abu-Ibrahim. “Nucleus-nucleus total reaction cross sections, and the nuclear interaction radius”. In: *Physical Review C* 83.4 (Apr. 2011), p. 044615. DOI: 10.1103/PhysRevC.83.044615.

[15] M. Takechi et al. “Reaction cross sections at intermediate energies and Fermi-motion effect”. In: *Phys. Rev. C* 79 (6 June 2009), p. 061601. DOI: 10.1103/PhysRevC.79.061601. URL: https://link.aps.org/doi/10.1103/PhysRevC.79.061601.

[16] J. Jaros et al. “Nucleus-nucleus total cross sections for light nuclei at 1.55 and 2.89 GeV/c per nucleon”. In: *Phys. Rev. C* 18 (5 Nov. 1978), pp. 2273–2292. DOI: 10.1103/PhysRevC.18.2273.

[17] *World Cancer Research Fund (WCRF). Worldwide Cancer Data.* URL: https://www.wcrf.org/cancer-trends/worldwide-cancer-data/.

[18] Robert R. Wilson. “Radiological Use of Fast Protons”. In: *Radiology* 47.5 (1946), 487–491.

[19] Particle Therapy Co-Operative Group (PTCOG). 2022. URL: https://ptcog.site/.

[20] M. A. Dymova et al. “Boron neutron capture therapy: Current status and future perspectives”. In: *Cancer Communications (London)* 40.9 (Sept. 2020), pp. 406–421. DOI: 10.1002/cac2.12089.

[21] *Centro Nazionale di adroterapia.* URL: https://fondazionecnao.it/.

[22] Marco Durante and Harald Paganetti. “Nuclear physics in particle therapy: a review”. In: *Reports on Progress in Physics* 79.9 (Aug. 2016), p. 096702. DOI: 10.1088/0034-4885/79/9/096702. URL: https://dx.doi.org/10.1088/0034-4885/79/9/096702.

[23] David Jette and Weimin Chen. “Creating a spread-out Bragg peak in proton beams”. In: *Physics in Medicine and Biology* 56 (2011), N131–N138. DOI: 10.1088/0031-9155/56/11/N01.

[24] Jennifer S. Chiang et al. “Proton beam radiotherapy for patients with early-stage and advanced lung cancer: a narrative review with contemporary clinical recommendations”. In: *Journal of Thoracic Disease* 13.2 (2021). ISSN: 2077-6624. URL: https://jtd.amegroups.org/article/view/48525.

[25] E Haettner et al. “Experimental study of nuclear fragmentation of 200 and 400 MeV/u ^{12}C ions in water for applications in particle therapy”. In: *Physics in Medicine and Biology* 58.23 (Nov. 2013), p. 8265. DOI: 10.1088/0031-9155/58/23/8265. URL: https://dx.doi.org/10.1088/0031-9155/58/23/8265.

[26] K Gunzert-Marx et al. “Secondary beam fragments produced by 200 MeV/u ^{12}C ions in water and their dose contributions in carbon ion radiotherapy”. In: *New Journal of Physics* 10.7 (July 2008), p. 075003. ISSN: 1367-2630. DOI: 10.1088/1367-2630/10/7/075003.

[27] F. Tommasino and M. Durante. “Proton Radiobiology”. In: *Cancers* 7 (2015), pp. 353–381. DOI: 10.3390/cancers7010353.

[28] Marco Durante and Francis A. Cucinotta. “Physical basis of radiation protection in space travel”. In: *Rev. Mod. Phys.* 83 (4 Nov. 2011), pp. 1245–1281. DOI: 10.1103/RevModPhys.83.1245. URL: https://link.aps.org/doi/10.1103/RevModPhys.83.1245.

[29] Marco Durante and Francis A. Cucinotta. “Heavy ion carcinogenesis and human space exploration”. In: *Nature Reviews Cancer* 8.6 (2008), pp. 465–472. DOI: 10.1038/nrc2391.

[30] C. Zeitlin et al. “Measurements of materials shielding properties with 1GeV/nuc ^{56}Fe”. In: *Nuclear Instruments and Methods in Physics Research Section B: Beam Interactions with Materials and Atoms* 252.2 (2006), pp. 308–318. ISSN: 0168-583X. DOI: https://doi.org/10.1016/j.nimb.2006.08.011. URL: https://www.sciencedirect.com/science/article/pii/S0168583X06008809.

[31] P. Schwaller et al. “Proton total cross sections on 1H, 2H, 4He, 9Be, C and O in the energy range 180 to 560 MeV”. In: *Nuclear Physics A* 316.3 (1979), pp. 317–344. ISSN: 0375-9474. DOI: https://doi.org/10.1016/0375-9474(79)90040-X. URL: https://www.sciencedirect.com/science/article/pii/037594747990040X.

[32] B. Braunn et al. “Assessment of nuclear-reaction codes for proton-induced reactions on light nuclei below 250 MeV”. In: *European Physical Journal Plus* 130.7 (2015), p. 153. DOI: https://doi.org/10.1140/epjp/i2015-15153-x.

[33] *Experimental nuclear reaction data (EXFOR).* URL: https://www-nds.iaea.org/exfor/.

[34] A. S. Iljinov et al. “Production of radionuclides at intermediate energies, Landolt-Börnstein”. In: New Series, Subvol. I/13. Springer-Verlag, Berlin-Heidelberg, 1991.

[35] A. J. Koning, S. Hilaire, and M. C. Duijvestijn. "TALYS-1.0". In: *International Conference on Nuclear Data for Science and Technology* (2007), pp. 211–214. DOI: 10.1051/ndata:07767. URL: https://doi.org/10.1051/ndata:07767.

[36] ICRU. *Nuclear Data for Neutron and Proton Radiotherapy and for Radiation Protection*. Report 63. ICRU, 2000.

[37] A. Boudard et al. "New potentialities of the Liège intranuclear cascade model for reactions induced by nucleons and light charged particles". In: *Phys. Rev. C* 87 (1 Jan. 2013), p. 014606. DOI: 10.1103/PhysRevC.87.014606. URL: https://link.aps.org/doi/10.1103/PhysRevC.87.014606.

[38] J. Dudouet et al. "Double-differential fragmentation cross-section measurements of 95 MeV/nucleon ^{12}C beams on thin targets for hadron therapy". In: *Phys. Rev. C* 88 (2 Aug. 2013), p. 024606. DOI: 10.1103/PhysRevC.88.024606. URL: https://link.aps.org/doi/10.1103/PhysRevC.88.024606.

[39] J. Norbury et al. "Review of nuclear physics experiments for space radiation". In: *Health Phys.* 103 (2012), pp. 640–642.

[40] Battistoni G. et al. "Measuring the Impact of Nuclear Interaction in Particle Therapy and in Radio Protection in Space: the FOOT Experiment". In: *Frontiers in Physics* 8 (2021). ISSN: 2296-424X. DOI: 10.3389/fphy.2020.568242. URL: https://www.frontiersin.org/journals/physics/articles/10.3389/fphy.2020.568242.

[41] T.T. Böhlen et al. "The FLUKA Code: Developments and Challenges for High Energy and Medical Applications". In: *Nuclear Data Sheets* 120 (2014), pp. 211–214. DOI: 10.1016/j.nds.2014.07.049.

[42] G. Battistoni et al. "The FLUKA Code: an Accurate Simulation Tool for Particle Therapy". In: *Frontiers in Oncology* 6.116 (2016). URL: https://doi.org/10.3389/fonc.2016.00116.

[43] G. Alexandrov et al. *FOOT CDR Conceptual Design*. Tech. rep. Aug. 2017. DOI: 10.13140/RG.2.2.28904.78080.

[44] *EJ-228 scintillator*. URL: https://www.southernscientific.co.uk/data/file/8/6/SSL_EJ228-230.1438855383.pdf.

[45] L. Galli et al. "WaveDAQ: An highly integrated trigger and data acquisition system". In: *Nuclear Instruments and Methods in Physics Research Section A: Accelerators, Spectrometers, Detectors and Associated Equipment* 936 (2019). Frontier Detectors for Frontier Physics: 14th Pisa Meeting on Advanced Detectors, pp. 399–400. ISSN: 0168-9002. DOI: https://doi.org/10.1016/j.nima.2018.07.067.

[46] A.C. Kraan et al. "Charge identification of nuclear fragments with the FOOT Time-Of-Flight system". In: *Nuclear Instruments and Methods in Physics Research Section A* 1001 (2021), p. 165206. ISSN: 0168-9002. DOI: 10.1016/j.nima.2021.165206.

[47] R. Pleskac et al. "The FIRST experiment at GSI". In: *Nuclear Instruments and Methods in Physics Research Section A* 678 (2012), pp. 130–138. ISSN: 0168-9002. DOI: 10.1016/j.nima.2012.02.020.

[48] Y. Dong et al. "The Drift Chamber detector of the FOOT experiment: Performance analysis and external calibration". In: *Nuclear Instruments and Methods in Physics Research Section A: Accelerators, Spectrometers, Detectors and Associated Equipment* 986 (2021), p. 164756. DOI: 10.1016/j.nima.2020.164756.

[49] Yunsheng Dong et al. "The Drift Chamber detector of the FOOT experiment: Performance analysis and external calibration". In: *Nuclear Instruments and Methods in Physics Research Section A: Accelerators, Spectrometers, Detectors and Associated Equipment* 986 (2021), p. 164756. ISSN: 0168-9002. DOI: https://doi.org/10.1016/j.nima.2020.164756.

[50] E. Spiriti et al. "CMOS active pixel sensors response to low energy light ions". In: *Nuclear Instruments and Methods in Physics Research Section A: Accelerators, Spectrometers, Detectors and Associated Equipment* 875 (2017), pp. 35–40. DOI: 10.1016/j.nima.2017.08.058.

[51] Gianluigi Silvestre. "Characterization of the Microstrip Silicon Detector for the FragmentatiOn Of Target experiment". In: *Nuclear Instruments and Methods in Physics Research Section A: Accelerators, Spectrometers, Detectors and Associated Equipment* 1047 (2023), p. 167717. ISSN: 0168-9002. DOI: https://doi.org/10.1016/j.nima.2022.167717.

[52] A.C. Kraan et al. "Charge identification of nuclear fragments with the FOOT Time-Of-Flight system". In: *Nuclear Instruments and Methods in Physics Research Section A: Accelerators, Spectrometers, Detectors and Associated Equipment* 1001 (2021), p. 165206. ISSN: 0168-9002. DOI: https://doi.org/10.1016/j.nima.2021.165206.

[53] Riccardo Ridolfi. "The FOOT Experiment: Trigger and Data Acquisition (TDAQ) Development and Data Analysis". PhD thesis. University of Bologna, 2022.

[54] L. Scavarda. "Design and performance of the Calorimeter for the FOOT experiment". In: *Il Nuovo Cimento C* 43.123 (2020), pp. 1–7. DOI: 10.1393/ncc/i2020-20123-3.

[55] L. Scavarda. "The FOOT experiment: Measuring proton and light nuclei fragmentation cross sections up to 700 MeV/A". In: *Bulletin of the Russian Academy of Sciences: Physics* 84 (2020), pp. 480–484. DOI: 10.3103/S1062873820040267.

[56] Giuliana Galati et al. "Charge identification of fragments with the emulsion spectrometer of the FOOT experiment". In: *Open Physics* 19.1 (2021), pp. 383–394. DOI: doi:10.1515/phys-2021-0032.

[57] *SHOE, INFN git repository*. URL: https://baltig.infn.it/asarti/shoe.

[58] *ROOT Data Analysis Framework*. URL: https://root.cern/.

[59] Schmitt, Stefan. "Data Unfolding Methods in High Energy Physics". In: *EPJ Web Conf.* 137 (2017), p. 11008. DOI: 10.1051/epjconf/201713711008. URL: https://doi.org/10.1051/epjconf/201713711008.

[60] G. D'Agostini. *Improved iterative Bayesian unfolding*. 2010. arXiv: 1010.0632 [physics.data-an]. URL: https://arxiv.org/abs/1010.0632.

[61] G. D'Agostini. "A Multidimensional unfolding method based on Bayes' theorem". In: *Nucl. Instrum. Meth. A* 362 (1995), pp. 487–498. DOI: 10.1016/0168-9002(95)00274-X.

[62] *RooUnfold*. URL: https://gitlab.cern.ch/RooUnfold/RooUnfold.

[63] C. Zeitlin et al. "Fragmentation of ^{14}N, ^{16}O, ^{20}Ne, and ^{24}Mg nuclei at 290 to 1000 MeV/nucleon". In: *Phys. Rev. C* 83 (3 Mar. 2011), p. 034909. DOI: 10.1103/PhysRevC.83.034909. URL: https://link.aps.org/doi/10.1103/PhysRevC.83.034909.